A national laboratory of the U.S. Department of Energy
Office of Energy Efficiency & Renewable Energy

National Renewable Energy Laboratory

Innovation for Our Energy Future

High-Efficiency Amorphous Silicon Alloy Based Solar Cells and Modules

Final Technical Progress Report
30 May 2002 – 31 May 2005

S. Guha and J. Yang
United Solar Ovonic Corporation
Troy, Michigan

Subcontract Report
NREL/SR-520-38728
October 2005

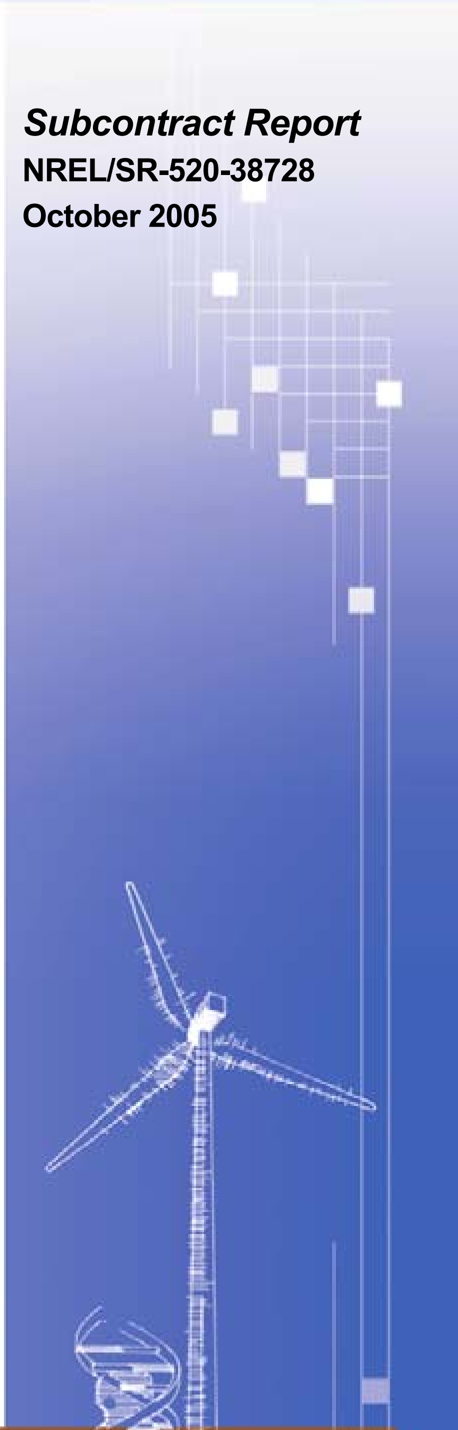

NREL is operated by Midwest Research Institute • Battelle Contract No. DE-AC36-99-GO10337

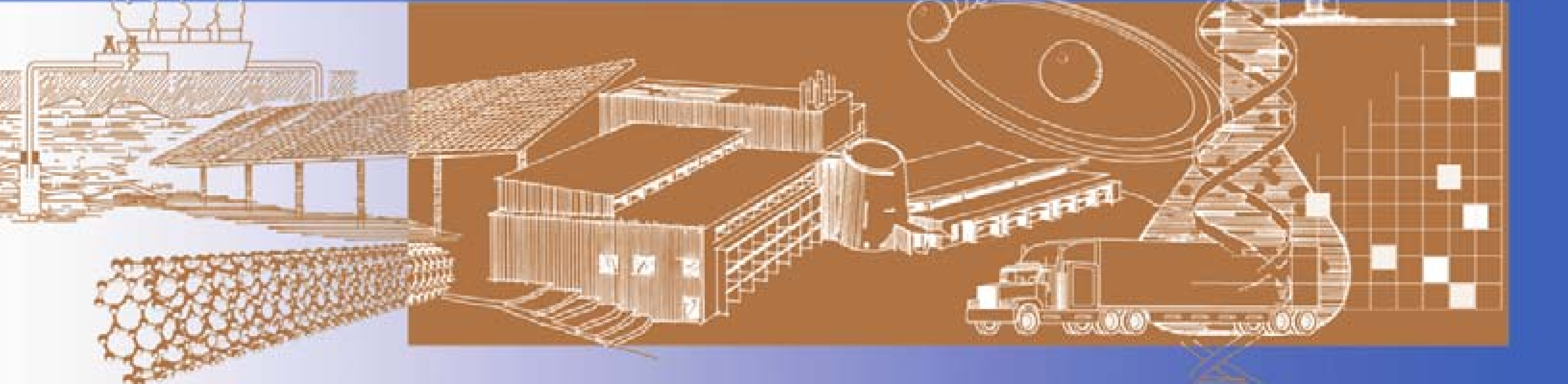

High-Efficiency Amorphous Silicon Alloy Based Solar Cells and Modules

Final Technical Progress Report
30 May 2002 – 31 May 2005

S. Guha and J. Yang
United Solar Ovonic Corporation
Troy, Michigan

NREL Technical Monitor: B. von Roedern
Prepared under Subcontract No. ZDJ-2-30630-19

Subcontract Report
NREL/SR-520-38728
October 2005

National Renewable Energy Laboratory
1617 Cole Boulevard, Golden, Colorado 80401-3393
303-275-3000 • www.nrel.gov

Operated for the U.S. Department of Energy
Office of Energy Efficiency and Renewable Energy
by Midwest Research Institute • Battelle

Contract No. DE-AC36-99-GO10337

NOTICE

Available electronically at http://www.osti.gov/bridge

Available for a processing fee to U.S. Department of Energy
and its contractors, in paper, from:
U.S. Department of Energy
Office of Scientific and Technical Information
P.O. Box 62
Oak Ridge, TN 37831-0062
phone: 865.576.8401
fax: 865.576.5728
email: mailto:reports@adonis.osti.gov

Available for sale to the public, in paper, from:
U.S. Department of Commerce
National Technical Information Service
5285 Port Royal Road
Springfield, VA 22161
phone: 800.553.6847
fax: 703.605.6900
email: orders@ntis.fedworld.gov
online ordering: http://www.ntis.gov/ordering.htm

Table of Contents

Preface

This final Subcontract Report covers the work performed by United Solar Ovonic Corporation for the period from May 30, 2002 to May 31, 2005 under National Renewable Energy Laboratory (NREL) Thin Film Partnership Subcontract No. ZDJ-2-30630-19. The following personnel participated in this research program.

> A. Banerjee, E. Chen, G. Fischer, G. Ganguly, S. Guha (Principal Investigator), B. Hang, M. Hopson, N. Jackett, T. Johnson, K. Lord, A. Mohsin, T. Nazmee, J. Noch, J. M. Owens, T. Palmer, G. Pietka, D. Wolf, B. Yan, J. Yang (Co-Principal Investigator), K. Younan, and G. Yue.

Collaboration with the Colorado School of Mines, University of North Carolina, University of Oregon, University of Utah, Syracuse University, and National Renewable Energy Laboratory is acknowledged. We would like to thank S. R. Ovshinsky and H. Fritzsche for their constant encouragement and useful discussion, and S. Sundquist for preparation of this report.

Executive Summary

Objectives

The principal objective of this R&D program is to expand, enhance, and accelerate knowledge and capabilities for development of high-efficiency hydrogenated amorphous silicon (a-Si:H) and amorphous silicon-germanium alloy (a-SiGe:H) related thin-film multi-junction solar cells and modules with low manufacturing cost and high reliability. Our strategy has been to use the spectrum-splitting triple-junction structure, a-Si:H/a-SiGe:H/a-SiGe:H, to improve solar cell and module efficiency, stability, and throughput of production. The methodology used to achieve the objectives included: i) explore the highest stable efficiency using the triple-junction structure deposited using RF glow discharge at a low rate, ii) fabricate the devices at a high deposition rate for high throughput and low cost, and iii) develop an optimized recipes using the R&D batch large-area reactor to help the design and optimization of the roll-to-roll production machines. For short-term goals, we have worked on the improvement of a-Si:H and a-SiGe:H alloy solar cells. a-Si:H and a-SiGe:H are the foundation of current a-Si:H based thin film photovoltaic technology. Any improvement in cell efficiency, throughput, and cost reduction will immediately improve operation efficiency of our manufacturing plant allowing us to further expand our production capacity.

For long-term goals, we have explored alternative materials and advanced technologies for next generation thin-film photovoltaic production. In the last few years, the research on hydrogenated nanocrystalline silicon (nc-Si:H) solar cells has attracted significant attention. Using nc-Si:H as the bottom cell in multi-junction structures, cell efficiency of over 14% and module efficiency of over 13% have been reported. At United Solar, we started to investigate the possibility of using nc-Si:H as the bottom cell in a-Si:H/nc-Si:H double-junction and a-Si:H/a-SiGe:H/nc-Si:H triple-junction structures to address the long term goals for the next generation large volume and low cost manufacturing plants. Three issues have been identified as the main focus in this study: i) searching for the highest stable cell and module efficiency; ii) increasing deposition rate and reducing deposition time to satisfy manufacturing requirements, and iii) investigating the issues related to large-area deposition, especially the uniformity of layer thickness and cell performance. During the three years of study, we have worked on these three areas and accumulated significant experience in material deposition and characterization, solar cell design and manufacture, and device characterization. We have achieved initial active-area efficiencies of 13.5% and 14.6% using a-Si:H/nc-Si:H double-junction and a-Si:H/a-SiGe:H/nc-Si:H triple-junction structures, respectively. For high rate and large area deposition, we have also made significant progress. Initial and stable active-area efficiencies of 13.1% and 11.5%, respectively, have been obtained with an a-Si:H/nc-Si:H double-junction structure, where the intrinsic a-Si:H layer in the top cell and nc-Si:H layer in the bottom cell were deposited in 10 and 30 minutes, respectively. In large-area deposition, we have used RF glow discharge technique for making a-Si/nc-Si:H double-junction cells. An initial aperture-area (420 cm^2) efficiency of 11.7% has been obtained with the intrinsic nc-Si:H layer deposited in 50 minutes. Although we still cannot answer the question of whether nc-Si:H should be used in the next generation manufacturing line at this time, we have already established ourselves as a leader in the field of nc-Si:H solar cells. During the course of the program, we have actively collaborated with team members and other institutions.

Approaches

In manufacturing, United Solar uses a triple-junction spectral-splitting solar cell structure and a roll-to-roll deposition process. The conventional a-Si:H/a-SiGe:H/a-SiGe:H triple-junction cells use an a-Si:H top cell (~1.8 eV bandgap) to absorb the blue light, an a-SiGe:H middle cell with ~20% germanium (~1.6 eV bandgap) to absorb the green light, and an a-SiGe:H bottom cell with ~40% germanium (~1.4 eV bandgap) to capture the red light. One objective of this program is to continue the optimization of a-Si:H top cell, a-SiGe:H middle cell, and a-SiGe:H bottom cell to achieve high efficiency. We have used a large-area deposition system to develop deposition parameters for the a-Si:H/a-SiGe:H/a-SiGe:H triple-junction structure. First, we modified the "2B" machine (this is a multi-chamber R&D deposition machine that can use substrates with an area of 15" x 14") by replacing the existing deposition cathodes with modified cathodes in order to improve the uniformity and cell efficiency. The new cathode design is similar to that used in our current 25 MW/year production machine. Any gain in cell efficiency obtained in the 2B machine can be transferred to the production equipment. Second, we used the improved hardware design to optimize a-Si:H and a-SiGe:H component cells including the uniformity and cell performance. For cost reduction, we investigated the feasibility of using a SiH_4/GeH_4 mixture instead of a Si_2H_6/GeH_4 mixture for the a-SiGe:H alloy middle and bottom cells. Finally, we optimized the process for making a-Si:H/a-SiGe:H/a-SiGe:H triple-junction cells using the 25 MW/year production constraints.

In order to address the long-term goals, we have developed nc-Si:H solar cells as a potential replacement for the a-SiGe:H bottom cell in the triple-junction structure. During the past three years, we continued to work on the optimization of nc-Si:H single-junction solar cells at various deposition rates and incorporated the improved nc-Si:H single-junction cell in a-Si:H/nc-Si:H double-junction and a-Si:H/a-SiGe:H/nc-Si:H triple-junction structures. To answer the question whether nc-Si:H is a better choice for the next generation manufacturing plant, we have carried out research in the following areas: i) deposition of nc-Si:H films and solar cells using RF glow discharge at a low rate of ~1 Å/s to achieve the highest efficiency, ii) deposition of nc-Si:H films and solar cells using modified very-high frequency (MVHF) glow discharge at a high rate of ~3-10 Å/s, iii) deposition of nc-Si:H films and solar cells using RF glow discharge under a high-pressure and high-power regime at a high rate of ~3-5 Å/s, iv) deposition of a-Si:H/nc-Si:H double-junction solar cells on large-area substrates at various deposition rates using the 2B machine, and v) metastability of nc-Si:H single-junction, a-Si:H/nc-Si:H double-junction, and a-Si:H/a-SiGe:H/nc-Si:H triple-junction cells. In addition, we collaborated with Colorado School of Mines, University of North Carolina, University of Oregon, Syracuse University, University of Utah, and NREL on material and solar cell characterizations.

Status/Accomplishments

Large-area (2B machine) deposition of a-Si:H/a-SiGe:H/a-SiGe:H triple-junction solar cells using the constraints of the 25 MW/year production line

- New cathodes with a structure similar to the 25 MW/year machine have been designed, fabricated, and installed in the 2B machine.

- Uniformity of films deposited using the new cathode has been studied. The results showed an improved uniformity.
- a-Si:H and a-SiGe:H alloy component cells have been deposited under the constraints of the 25 MW/year machine.
- a-SiGe:H alloy middle and bottom cells have been made using a SiH_4/GeH_4 mixture and show a similar performance to those made with a Si_2H_6/GeH_4 mixture.
- An initial active-area (0.25 cm^2) efficiency of 11.4% was achieved using an a-Si:H/a-SiGe:H/a-SiGe:H triple-junction cell deposited on a large-area Al/ZnO back reflector from the production line. This value corresponds to an initial total-area efficiency of 10.6%. The deposition conditions were under production constraints using SiH_4 and GeH_4 instead of Si_2H_6 and GeH_4 for the gas mixture.
- The same cell was light soaked for over 1000 hours. A stable active-area efficiency of 9.8% was achieved. This value corresponds to a stable total-area efficiency of 9.1%, and is the same as our best value achieved with Si_2H_6/GeH_4 mixture at high rates.

Small-area cells deposited using RF glow discharge at low rates

We have worked on developing and optimizing nc-Si:H materials and solar cells using RF glow discharge at low rates to search for the highest efficiency with different cell structures. The highest efficiency values achieved are listed below. We give values for active-area efficiency. The grid loss is typically ~7%, and the total area efficiency is therefore ~7% lower.

- 8.4% initial active-area (0.25 cm^2) cell efficiency for a nc-Si:H single-junction structure.
- 13.5% initial and 11.8% stable active-area (0.25 cm^2) cell efficiencies for an a-Si:H/nc-Si:H double-junction structure.
- 14.6% initial and 12.6% stable active-area (0.25 cm^2) cell efficiency for an a-Si:H/a-SiGe:H/nc-Si:H triple-junction structure.

Small-area cells deposited using MVHF glow discharge at high rates

We have used a modified very-high-frequency (MVHF) glow discharge to deposit nc-Si:H material and solar cells at high deposition rates of ~ 3-10 Å/s using parameters that satisfy production requirements. We have achieved the following results in this deposition regime.

- Initial and stable active-area (0.25 cm^2) efficiencies of 8.4% and 8.2% have been achieved using nc-Si:H single-junction cells made at high rates. The intrinsic nc-Si:H layer was deposited in 30 minutes.
- Initial and stable active-area (0.25 cm^2) efficiencies of 13.1% and 11.5% have been achieved using a-Si:H/nc-Si:H double-junction cells made at high rates. The intrinsic a-Si:H layer in the top cell and nc-Si:H layer in the bottom cell were deposited in 10 and 30 minutes, respectively.
- An initial active-area (0.25 cm^2) efficiency of 13.8% has been achieved using an a-Si:H/a-SiGe:H/nc-Si:H triple-junction cell made at high rates. The cell efficiency stabilized to 11.4% after prolonged light soaking.

Small-area cells deposited using RF glow discharge under high pressure at high deposition rates

In 2003, we started to use RF glow discharge under high pressure with high power to obtain a high rate deposition of nc-Si:H solar cells. The deposition rate is in the range of 3-5 Å/s. Within a very short period of time, we have achieved the following results.

- An initial active-area (0.25 cm^2) efficiency of 6.7% has been achieved for an nc-Si:H single-junction cell.
- An initial active-area (0.25 cm^2) efficiency of 12.3% has been achieved for an a-Si:H/nc-Si:H double-junction cell.

Large-area (2B machine) deposition of a-Si:H/nc-Si:H double-junction solar cells

Next, we tried to duplicate the above results in a large-area reactor. The results are summarized below.

- Initial 7.3% and stable 7.0% active-area (0.25 cm^2) efficiencies have been achieved using a nc-Si:H single-junction cell at a high rate of ~ 3-5 Å/s. The intrinsic layer deposition time was 50 minutes.
- An initial active-area (0.25 cm^2) efficiency of 13.2% has been achieved using a-Si:H/nc-Si:H double-junction cells at a low rate of ~ 1 Å/s. The intrinsic layer deposition time was 150 minutes. A stable active-area efficiency of 11.7% has also been achieved.
- An initial aperture-area (45 cm^2) efficiency of 12.3% has been achieved using an a-Si:H/nc-Si:H double-junction cell at a high rate of ~ 3-5 Å/s. The intrinsic layer deposition time was 50 minutes. The stable cell efficiency is 10.9%.
- An initial aperture-area (420 cm^2) efficiency of 11.8% has been achieved using an a-Si:H/nc-Si:H double-junction cell at a high rate of ~ 3-5 Å/s. The intrinsic layer deposition time was 50 minutes. The efficiency after encapsulation and light soaking stabilized at 9.5%.

Light-induced V_{oc} increase in mixed-phase solar cells

Solar cells made under conditions near the transition from a-Si:H to nc-Si:H phase show many interesting features. The most interesting observation is the increase of open-circuit voltage (V_{oc}) after prolonged light soaking. In the first year of this project, we carefully studied the phenomenon of light induced degradation in the mixed-phase solar cells and achieved the following results:

- A comprehensive explanation for the light-induced V_{oc} increase in the mixed-phase solar cells has been proposed based on a two-diode equivalent circuit model. This model is consistent with most of the existing experimental results.
- New experimental results with different a-Si:H buffer layer between the *p* and *i* layers support the two-diode equivalent circuit model.
- A study of the kinetics of light-induced V_{oc} change has been carried out, which has provided insight into the mechanism of the light-induced V_{oc} increase. The kinetic results are explained using the two-diode equivalent circuit model.

Stability of single-junction and multi-junction solar cells with nc-Si:H in the bottom cell

It has been reported that nc-Si:H solar cells show no light-induced degradation. However, nc-Si:H solar cells cover a very wide range in material structures, including different ratio of amorphous and crystalline components. nc-Si:H solar cells with certain volume fraction of nanocrystallites have shown light-induced degradation. During this project, we have systematically studied the light-induced degradation in nc-Si:H single-junction and multi-junction cells using nc-Si:H in the bottom cell. The following is a list of the key results:

- The light-induced degradation in nc-Si:H single-junction cell efficiency was found to be in the range of 0 to 15% depending on the deposition condition and cell structure.
- The spectrum dependence of the light-induced degradation suggests that the light-induced degradation occurs mainly in the amorphous phase or grain boundaries.
- No forward current induced degradation was observed.
- A reverse electrical bias does not reduce, but increases the light-induced degradation in some nc-Si:H single-junction cells.
- A model based on back-to-back connected diodes explains the reverse bias enhanced light-induced degradation.
- A bottom cell limited current mismatch improves the stable efficiency of multi-junction cells with a nc-Si:H bottom cell.
- An optimized deposition regime with a proper device design has been found to produce nc-Si:H with little light-induced degradation.

Optimization of Ag/ZnO back reflector

High efficiency solar cells require not only high quality active layers but also passive layers such as the back reflector and top transparent contact. In the R&D department of United Solar, we have developed high quality Ag/ZnO back reflectors for high efficiency a-Si:H/a-SiGe:H/a-SiGe:H triple-junction cells. Due to differences in the material properties and device structure of nc-Si:H solar cells, the previously optimized Ag/ZnO back reflector may not be the best for nc-Si:H solar cells because of the differences in the material properties and device structures in nc-Si:H solar cells,. On the other hand, any improvement in the Ag/ZnO may contribute to further improvement in the conventional a-Si:H/a-SiGe:H/a-SiGe:H triple-junction cells. Therefore, we have re-optimized the Ag/ZnO back reflector for both the nc-Si:H and a-SiGe:H solar cells. The following experiments have been carried out:

- The surface morphology of the Ag/ZnO back reflector was optimized by adjusting the sputtering deposition parameters.
- The surface morphology of the Ag/ZnO back reflector was modified by chemical etching using diluted HCl.
- Atomic Force Microscopy (AFM) was used to characterize the surface morphology.
- Light scattering properties were characterized and correlated with the surface morphology.
- Quality of Ag/ZnO back reflectors was evaluated using nc-Si:H and a-SiGe:H solar cells.

In conclusion, we have made significant progress in our understanding of multi-junction solar cells both using a-SiGe:H and nc-Si:H in the bottom cell. The progress in efficiency for nc-Si multi-junction solar cells is shown in the figure below.

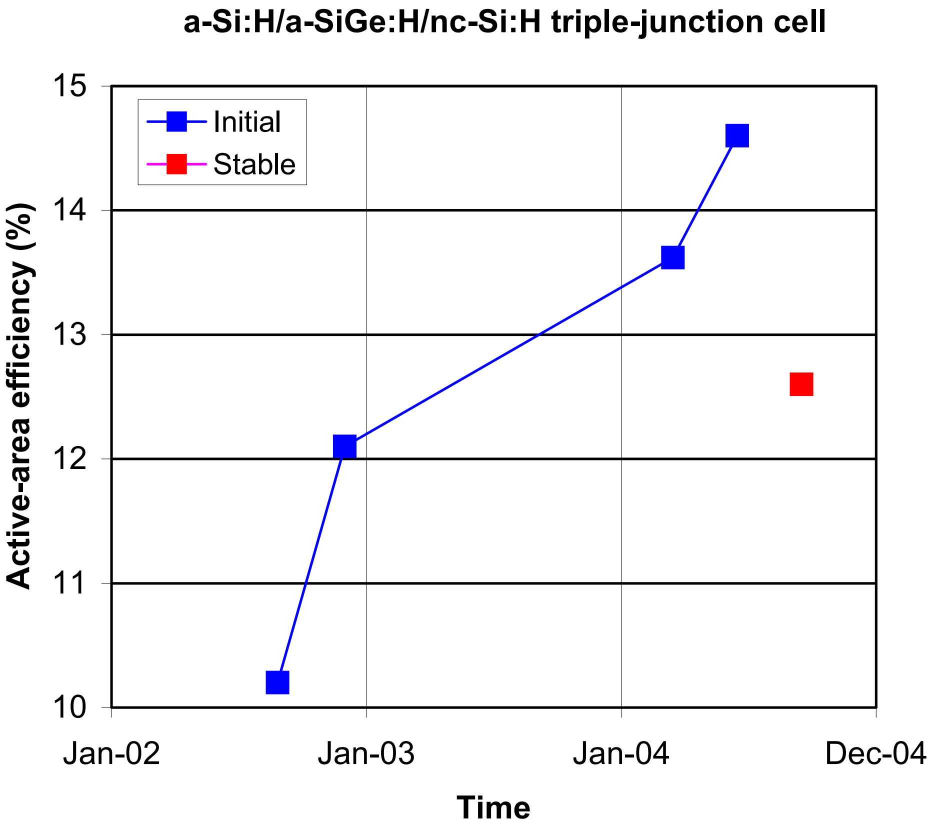

Publications

1. E. Stratakis, E. Spanakis, P. Tzanetakis, H. Fritzsche, S. Guha, and J. Yang, "Photoinduced stress in hydrogenated amorphous silicon films," Appl. Phys. Lett. **80**, 1734 (2002).
2. B. Yan, K. Lord, J. Yang, S. Guha, J. Smeets, and J-M. Jacquet, "Hydrogenated microcrystalline silicon solar cells made with modified very-high-frequency glow discharge," *Mat. Res. Soc. Symp. Proc.* **715**, 629 (2002).
3. J. Yang, K. Lord, B. Yan, A. Banerjee, S. Guha, D. Han, and K. Wang, "Correlation of light-induced enhancement of open-circuit voltage and structural change of heterogeneous silicon solar cells," *Mat. Res. Soc. Symp. Proc.* **715**, 601 (2002), (INVITED).
4. K. J. Beernink, G. Pietka, J. Noch, K. Younan, D. Wolf, A. Banerjee, J. Yang, and S. Guha, "Ultralight amorphous silicon alloy photovoltaic modules for space applications," *Mat. Res. Soc. Symp. Proc.,* V6.3 (2002).
5. J. Yang, K. Lord, B. Yan, A. Banerjee, and S. Guha, "Correlation of the open-circuit voltage enhancement of heterogeneous silicon solar cells and the Staebler-Wronski effect" *Proc. 29th IEEE Photovoltaic Specialists Conference*, (2002), p. 1094.
6. S. Guha and J. Yang, "Amorphous silicon alloy materials, cells, and modules," *Proc. 29th IEEE Photovoltaic Specialists Conference*, (2002), p. 1070 (INVITED).
7. Q. Wang, E. Iwaniczko, J. Yang, K. Lord, S. Guha, K. Wang, and D. Han, "Wide-gap thin film Si *n-i-p* solar cells deposited by hot-wire CVD," *Proc. 29th IEEE Photovoltaic Specialists Conference*, (2002), p. 1222.
8. B. D. Chapman, S. W. Han, G. T. Seidler, E. A. Stern, J. D. Cohen, S. Guha, and J. Yang, "Short-range compositional randomness of hydrogenated amorphous silicon-germanium films," *J. Appl. Phys.* **92**, 801 (2002).
9. D. L. Williamson, D. W. M. Marr, J. Yang, B. Yan, and S. Guha "Nonuniform H distribution in thin-film hydrogenated amorphous Si by small-angle neutron scattering", Phys. Rev. B **67**, 075314 (2002).
10. J. Yang, B. Yan, G. Yue, A. Banerjee, K. Lord, and S. Guha, "Status of hydrogenated microcrystalline silicon solar cells at United Solar," NCPV and Solar Program Review Meeting, Denver, March 24 – 26, 2003.
11. B. Yan, J. Yang, and S. Guha, "Hydrogenated microcrystalline silicon solar cells using microwave glow discharge," NCPV and Solar Program Review Meeting, Denver, March 24 – 26, 2003.
12. J. M. Owens, D. Han, B. Yan, J. Yang, K. Lord, and S. Guha, "Micro-Raman measurements of mixed-phase hydrogenated silicon solar cells," NCPV and Solar Program Review Meeting, Denver, March 24 – 26, 2003.
13. B. Nelson, H. Atwater, B. von Roedern, J. Yang, P. Sims, X. Deng, V. Dalal, D. Carlson, and T. Wang, "Amorphous and thin-film silicon," NCPV and Solar Program Review Meeting, Denver, March 24 – 26, 2003.
14. B. Yan, J. Yang, G. Yue, and S. Guha, "Correlation of material properties and open-circuit voltage of amorphous silicon based solar cells," *Mat. Res. Soc. Symp. Proc.* **762,** 363 (2003)
15. B. Yan, G. Yue, J. Yang, A. Banerjee, and S. Guha, "Hydrogenated microcrystalline silicon single-junction and multi-junction solar cells," *Mat. Res. Soc. Symp. Proc.* **762,** 309 (2003), (INVITED).

16. G. Yue, B. Yan, J. Yang, K. Lord, and S. Guha, "Kinetics of light-induced effects in mixed-phase hydrogenated silicon solar cells," *Mat. Res. Soc. Symp. Proc.* **762,** 21 (2003)
17. K. Zhu, J. Yang, W. Wang. E. Schiff, J. Liang, and S. Guha, "Bandtail limits to solar conversion efficiencies in amorphous silicon solar cells," *Mat. Res. Soc. Symp. Proc.* **762,** 309 (2003)
18. J. M. Owens, D. Han, B. Yan, J. Yang, K. Lord, and S. Guha, "Micro-Raman studies of mixed-phase hydrogenated silicon solar cells," *Mat. Res. Soc. Symp. Proc.* **762,** 339 (2003).
19. E. Iwaniczko, A. H. Mahan, B. Yan, L. N. Gedvilas, D. L. Williamson, and B. P. Nelson "Deposition of device quality μc-Si films and solar cells at high rates by HWCVD in a W filament regime where W/Si formation is minimal," *Mat. Res. Soc. Symp. Proc.* **762,** 387 (2003).
20. B. Yan, G. Yue, J. Yang, K. Lord, A. Banerjee, and S. Guha, "Microcrystalline silicon solar cells made using RF, MVHF, and microwave at various deposition rates," *Proc. of 3rd World Conference on Photovoltaic Energy Conversion,* (Osaka, May 11-18, 2003), p. 2773 (INVITED).
21. B. Yan, J. Yang, G. Yue, K. Lord, and S. Guha, "On the mechanism of light-induced open-circuit voltage increase in mixed-phase hydrogenated silicon solar cells," *Proc. of 3rd World Conference on Photovoltaic Energy Conversion,* (Osaka, May 11-18, 2003), p.1627.
22. S. Guha, "Roll-to-roll production of amorphous silicon based triple junction solar cells," *Proc. of 3rd World Conference on Photovoltaic Energy Conversion*, (Osaka, May 11-18, 2003), p.1533 (INVITED).
23. B. Yan, J. Yang, and S. Guha, "Effect of hydrogen dilution on the open-circuit voltage of hydrogenated amorphous silicon solar cells," *Appl. Phys. Lett.* **83**, 782 (2003).
24. S. Guha, J. Yang, A. Banerjee, B. Yan, and K. Lord, "High quality amorphous silicon materials and cells grown with hydrogen dilution," *Solar Energy Materials & Solar Cells* **78**, 329 (2003).
25. J. Yang, A. Banerjee, and S. Guha, "Amorphous silicon based photovoltaic-from earth to the "final frontier"," *Solar Energy Materials & Solar Cells* **78**, 597 (2003).
26. S. Guha, "Advances in amorphous silicon alloy multi-junction solar cells and modules," *Technical Digest of the International PVSEC-14,* (Bangkok, Thailand, 2004) p. 33.
27. S. O. Kasap, M. Gunes, R. E. Johanson, Q. Wang, J. Yang, and S. Guha, "Conductance Fluctuations in a-Si:H: effects of alloying and device structure," *J. Mat. Science: Materials in Electronics* **14**, 693 (2003).
28. A. Hilchey, C. Lawyer, K. Wang, D. Han, B. Yan, G. Yue, J. Yang, and S. Guha, "Buffer-layer effect on mixed-phase cells studied by micro-Raman and photoluminescence spectroscopy," *Mat. Res. Soc. Symp. Proc.* **808***,* 35 (2004).
29. S. Guha, "Amorphous and microcrystalline silicon based photovoltaic," *Mat. Res. Soc. Symp. Proc.* **808***,* 521 (2004) (INVITED).
30. B. Yan, G. Yue, J. Yang, S. Guha, D. L. Williamson, D. Han, and C.-S. Jiang, "Microstructure evolution with thickness and hydrogen dilution profile in microcrystalline silicon solar cells", *Mat. Res. Soc. Symp. Proc.* **808***,* 575 (2004).
31. J. J. Gutierrez, A. F. Halverson, E. D. Tweeten, J. D. Cohen, B. Yan, J. Yang, and S. Guha, "Electronic properties of RF glow discharge intrinsic microcrystalline silicon near the amorphous silicon phase boundary," *Mat. Res. Soc. Symp. Proc.* **808***,* 115 (2004).

32. B. Yan, G. Yue, A. Banerjee, J. Yang, and S. Guha, “Large-area hydrogenated amorphous and microcrystalline silicon double-junction solar cells,” *Mat. Res. Soc. Symp. Proc.* **808***,* 581 (2004).
33. C.-S. Jiang, H.R. Moutinho, Q. Wang, M.M. Al-Jassim, B. Yan, J. Yang, and S. Guha, “ Measurement of electric potential on amorphous silicon and amorphous silicon germanium alloy thin-film solar cells by scanning Kelvin probe microscopy,” *Mat. Res. Soc. Symp. Proc.* **808***,* 587 (2004).
34. G. Yue, B. Yan, J. M. Owens, J. Yang, and S. Guha, “Microcrystalline silicon solar cells deposited using modified very-high frequency glow discharge and its application in multi-junction structures,” *Mat. Res. Soc. Symp. Proc.* **808***,* 593 (2004).
35. Y. Xu, B. Yan, B. P. Nelson, E. Iwaniczko, R. C. Reedy, A. H. Mahan, and H. Branz, “Devices fabrication with narrow-bandgap a-SiGe:H alloys deposited by HWCVD,” *Mat. Res. Soc. Symp. Proc.* **808***,* 617 (2004).
36. K. Wang, A. Canning, J. R. Weinberg-Wolf, E. C. T. Harley, D. Han, B. Yan, G. Yue, J. Yang, and S. Guha, “Correlation of hydrogenated nanocrystalline silicon microstructure and solar cell performance,” *Mat. Res. Soc. Symp. Proc.* **808***,* 59 (2004).
37. B. Yan, G. Yue, J. Yang, S. Guha, D. L. Williamson, D. Han, and C.-S. Jiang, “Hydrogen dilution profiling for hydrogenated microcrystalline silicon solar cells,” *Appl. Phys. Lett.* **85**, 1925 (2004).
38. B. Yan, G. Yue, J. M. Owens, J. Yang, and S. Guha, “Light-induced metastability in hydrogenated nanocrystalline silicon solar cells”, *Appl. Phys. Lett.* **85**, 1755 (2004).
39. J. Yang, B. Yan, and S. Guha, “Amorphous and nanocrystalline silicon PV technology,” *Proc. of DOE Solar Energy Technologies Program Review Meeting*, (Denver, Colorado, October 25-28, 2004), p. 332.
40. B. Yan, G. Yue, J. Yang, and S. Guha, “High rate Deposition of hydrogenated microcrystalline silicon solar cells,” *Proc. of DOE Solar Energy Technologies Program Review Meeting*, (Denver, Colorado, October 25-28, 2004), p. 456.
41. K. Wang, D. Han, B. Yan, J. Yang, and S. Guha, “Correlation of material properties and nc-Si:H solar cell performance studied by Raman and photoluminescence spectroscopy,” *Proc. of DOE Solar Energy Technologies Program Review Meeting*, (Denver, Colorado, October 25-28, 2004), p. 438.
42. A. Halverson, J. Gutierrez, J. D. Cohen, B. Yan, J. Yang, and S. Guha, “Electronic properties of RF glow discharge microcrystalline silicon near the amorphous silicon phase boundary,” *Proc. of DOE Solar Energy Technologies Program Review Meeting*, (Denver, Colorado, October 25-28, 2004), p. 435.
43. S. Guha, “Can your roof provide your electrical needs? - The growth prospect of building-integrated photovoltaic,” *Proc. of 31st Photovoltaic Specialists Conference*, (Florida, January 3-7, 2005), p. 12 (INVITED).
44. J. Yang, B. Yan, G. Yue, and S. Guha, “Comparison of hydrogenated amorphous silicon germanium and nanocrystalline silicon for multijunction solar cells - pros, cons, and status”, *Proc. of 31st Photovoltaic Specialists Conference,* (Florida, January 3-7, 2005), p. 1359 (INVITED).
45. G. Yue, B. Yan, J. Yang, and S. Guha, “Study of metastability of hydrogenated nanocrystalline silicon solar cells,” *Proc. of 31st Photovoltaic Specialists Conference*, (Florida, January 3-7, 2005), p.1416.

46. B. Yan, J. M. Owens, J. Yang, and S. Guha, "High efficiency triple-junction solar cells with hydrogenated nanocrystalline silicon bottom cell," *Proc. of 31st Photovoltaic Specialists Conference*, (Florida, January 3-7, 2005), p. 1465.
47. J. Yang, B. Yan, and S. Guha, "Amorphous and nanocrystalline silicon-based multi-junction solar cells," *Thin Solid Films*, (2005), in press.
48. G. Yue, B. Yan, J. Yang, and S. Guha, "Effect of electrical bias on metastability in hydrogenated nanocrystalline silicon solar cells," *Appl. Phys. Lett.* **86**, 092103 (2005).
49. M. Weizman, N. H. Nickel, and B. Yan, "Structural properties of laser-crystallized polycrystalline SiGe thin films," *Mat. Res. Soc. Symp. Proc.* **862***,* A2.5 (2005).
50. N. H. Nickel, I. Seiber, M. Weizman, and B. Yan, "Hydrogen bonding in amorphous and polycrystalline SiGe alloys," *Mat. Res. Soc. Symp. Proc.* **862***,* A3.5 (2005).
51. G. Yue, G. Ganguly, B. Yan, J. Yang, and S. Guha, "Correlation between powder in the plasma and stability of high rate deposited a-Si:H," *Mat. Res. Soc. Symp. Proc.* **862***,* A11.3 (2005).
52. J. Liang, E. A. Schiff, S. Guha, B. Yan, and J. Yang, "Light-induced effects on the open-circuit voltage of a-Si:H solar cells," *Mat. Res. Soc. Symp. Proc.* **862***,* A13.6 (2005).
53. A. F. Halverson, J. J. Gutierrez, D. Cohen, B. Yan, J. Yang, and S. Guha, "The effect of hydrogen profiling and of light induced degradation on electronic properties of hydrogenated nanocrystalline silicon," *Mat. Res. Soc. Symp. Proc.* **862***,* A13.7 (2005).
54. J. Liang, E. A. Schiff, S. Guha, B. Yan, and J. Yang, "Temperature-dependent measurements on a-Si:H solar cells," *Mat. Res. Soc. Symp. Proc.* **862***,* 21.8 (2005).
55. B. Yan, J. M. Owens, C.-S. Jiang, J. Yang, and S. Guha, "Improved back reflector for high efficiency hydrogenated amorphous and nanocrystalline silicon solar cells," *Mat. Res. Soc. Symp. Proc.* **862***,* A23.3 (2005).
56. K. Wang, D. Han, B. Huie, J. R. Weiberg-Wolf, B. Yan, J. Yang, and S. Guha, "Structural and electronic properties of hydrogenated nanocrystalline silicon films made with hydrogen dilution profiling technique," *Mat. Res. Soc. Symp. Proc.* **862***,* A24.3 (2005).
57. S. Guha and J. Yang, "Large-area deposition of amorphous silicon alloys using a roll-to-roll operation," *Mat. Res. Soc. Symp. Proc.,* H1.1 (2005) (INVITED).

Section 1: Introduction

United Solar Ovonic Corporation (United Solar) reported stable cell efficiency of 13% and a module efficiency of 10.5% using an a-Si:H/a-SiGe:H/a-SiGe:H triple-junction structure [1-2]. This technology was successfully transferred to mass production with a 5 MW/year capacity in 1997. To expand our production capability, we designed and constructed a new 25 MW/year plant in Auburn Hills, Michigan. The new machine has been in production since early 2003 [3]. With the proven success of the roll-to-roll technology and high demand for our unique flexible solar panels, another 25 MW/year manufacturing machine is under construction and is expected produce solar panels in 2006. The main objective of the current R&D research program is to address the Department of Energy's (DOE) goal of attaining 15% thin film module efficiency by developing new materials, device designs, and inexpensive manufacturing processes. In the past, we worked on a-Si:H and a-SiGe:H alloy based solar cells. The a-Si:H/a-SiGe:H/a-SiGe:H triple-junction structure is currently the frontrunner for obtaining the highest stable cell efficiency. In this three-year program, we have continued to work on large-area deposition issues that impact the current and future production machines. For this purpose, we redesigned the cathodes for the 2B machine taking into account the constraints of the production machine. The new hardware has been fabricated and installed in the machine, and uniformity studies have been carried out. The component and multi-junction solar cells have been fabricated. The a-SiGe:H alloy middle and bottom cells made with the new cathode show an improvement in cell performance and uniformity. In addition, we have changed from a Si_2H_6/GeH_4 mixture to a SiH_4/GeH_4 mixture for reducing the cost. After optimizing the deposition parameters, the a-SiGe:H middle and bottom cells show similar performance to those made with the Si_2H_6/GeH_4 mixture.

In recent years, the nc-Si:H solar cell has emerged as a potential substitute for the middle and bottom cells in the multi-junction structure due to low light-induced degradation, and GeH_4 is not needed in the deposition process. Kaneka Corp. has reported an initial cell efficiency of over 14% using an a-Si:H/nc-Si:H double-junction structure [4], and Canon Inc. achieved an initial module efficiency of over 13% using an a-Si:H/nc-Si:H/nc-Si:H triple-junction structure [5]. Starting from 2002, we started to develop nc-Si:H solar cells with the objective of using nc-Si:H as the bottom intrinsic layer in a multi-junction structure. We have carried out the deposition of nc-Si:H materials and solar cells using the conventional RF glow discharge at a low rate of ~1 Å/s to explore the practical limits of achievable efficiency. Concurrently, we have worked on the modified VHF (MVHF) technique and high pressure and high power RF glow discharge at high deposition rates of ~3-10 Å/s to develop a technology that is compatible with production [6].

With the success of making high-rate nc-Si:H solar cells in a small-area machine, we started to fabricate a-Si:H/nc-Si:H double-junction solar cells using our large-area machine (2B). We first started with a low rate recipe using RF glow discharge, and then explored the high pressure and high power regime for high rate deposition. We have obtained good cell results.

Stability is a critical issue for a-Si:H based solar cells. Solar cells made near the amorphous/nanocrystalline transition but still at the amorphous side show an improved stability against prolonged light soaking. However, if hydrogen dilution exceeds a certain level, the cell performance starts to decrease. Especially, the open-circuit voltage (V_{oc}) drops sharply with an increase in hydrogen dilution and attain a value around 0.5 V [7], a typical value for nc-Si:H solar cells. The materials and solar cells made in the transition regime contain a large amount of amorphous component with very little crystallite inclusion. Normally, there is no indication of crystalline component on Raman spectra; only micro-Raman can find crystalline components in certain areas [8]. Solar cells made in the transition regime are called mixed-phase solar cells. One interesting phenomenon of the mixed-phase solar cells is the light-induced increase of V_{oc} [9, 10]. A better understanding for the unusual light-induced V_{oc} increase in mixed-phase solar cells will help us in obtaining an overall picture about the metastability of a-Si:H and nc-Si:H. In the first year of the program, we have systematically studied the light-induced V_{oc} increase in mixed-phase solar cells and proposed a two-diode parallel-connected model. This model explains most of the experimental results [11].

nc-Si:H solar cells have been reported to exhibit no light-induced degradation [12, 13]. However, the term nc-Si:H represents a wide spectrum of materials with various grain sizes and different crystalline volume fractions. Therefore, one expects different stability behaviors in nc-Si:H solar cells with different microstructures. In addition, in an a-Si:H/nc-Si:H double-junction structure, the top cell is usually an a-Si:H cell with a relatively thick intrinsic layer to generate enough current for current matching with the nc-Si:H bottom cell. A thick a-Si:H cell might lead to a poor overall stability. Therefore, the stability study of nc-Si:H solar cells is an interesting topic not only for the fundamental understanding of the materials, but also for obtaining an optimized design for a stable multi-junction solar cells. Over the past three years, we have systematically studied the light-induced degradation in various nc-Si:H cells and under various conditions. In the beginning, we found that our nc-Si:H solar cells showed not only light induced degradation but also suffered from ambient degradation. The nc-Si:H cell performance degraded without intentional light soaking [14]. We discovered that the ambient degradation is due to the porosity that causes post-deposition oxygen diffusion. By optimizing the deposition conditions, we successfully overcame this problem and made nc-Si:H cells with no ambient degradation. We also found that nc-Si:H solar cells also show certain light-induced degradation in the range of 0 to 15% [15], depending on the deposition condition. We have made systematic studies of the light-induced degradation in nc-Si:H under different conditions. A lack of light-induced degradation under red light suggested that the light-induced degradation is mainly in the amorphous phase or grain boundary region [15]. Light soaking under a reverse bias showed an enhanced light induced degradation, which is opposite to the case in a-Si:H solar cells [16]. Although a satisfactory explanation has not been obtained, we have proposed a back-to-back diode model by considering the different characteristics in grains, grain boundaries, and amorphous tissues. Our model explains our results in a self-consistent way [17].

Section 2: Amorphous Silicon Alloy Component and Multi-junction Cells and Modules Deposited in a Large-Area Reactor with Production Constraints

2.1. Introduction

In the past, the best cells in R&D were fabricated by optimizing each deposition parameter independently. Some of these parameters are incompatible with the new 25 MW/year roll-to-roll production machine. For example, the deposition rate for the intrinsic layer for the R&D case was lower than that of production. A focused effort has been initiated in R&D to embrace the limitations of the deposition parameters in production. One objective under the current NREL contract is to expand this approach to encompass standardization of deposition hardware for both R&D and manufacturing. One important issue that is being addressed is the design of the RF cathode assembly for the deposition of the *n*, *i*, and *p* layers. The ultimate objective is to do research in improving cell quality in R&D using similar deposition hardware and parameters as those used in production. Any advances made in R&D can then be translated relatively easily to production. With this in mind, the cathode assembly in all three deposition chambers of the large-area "2B machine" in R&D has been modified to mimic the 25 MW/year production machine. The new cathodes are referred to as "new cathodes".

In R&D, the best triple-junction cells employ a-SiGe:H intrinsic layers (for the middle and bottom cells) fabricated using Si_2H_6/GeH_4 gas flow. The rationale is that Si_2H_6 and GeH_4 have similar dissociation rates that in turn lead to a similar Si/Ge ratio in the films over large gas flow distances. Replacement of the Si_2H_6/GeH_4 gas mixture with a SiH_4/GeH_4 mixture will lead to substantial cost savings. The challenge is to deposit cells with good quality and with minimizing the effects of gas depletion using the new gas mixture. The deposition parameters for best cell performance are dependent on the cathode hardware geometry. Preliminary work on the optimization of middle and bottom cells fabricated using the SiH_4/GeH_4 gas mixture and the new RF cathode assembly has been done. The a-SiGe:H middle and bottom cells made with the new cathode using the SiH_4/GeH_4 gas mixture show a similar performance to those made with the Si_2H_6/GeH_4 mixture. We then used the newly developed recipe in a-Si:H/a-SiGe:H/a-SiGe:H triple-junction structures and obtained initial and stable active-area (0.25 cm^2) efficiencies of 11.4% and 9.8%. The stable active-area efficiency corresponds to a stable total-area (0.268 cm^2) efficiency of 9.1%, which is similar to that obtained from the previous best cell made with the Si_2H_6/GeH_4 mixture.

A prerequisite to fabricating large-area high efficiency modules is to optimize the performance and the uniformity of smaller area cells. This approach enables the diagnosis and analysis of the devices at both the cell and module levels. Evaluation of the small-area (total area = 0.268 cm^2, active area = 0.25 cm^2) cells using current density versus voltage (J-V) and quantum efficiency (QE) measurements provides information about the basic device efficiency without the complications of electrical and optical losses associated with modules. It also enables the evaluation and optimization of the device at the component cell level.

2.2. Experimental

Stainless steel substrates with no back reflectors have been used for depositing various layers for thickness uniformity studies. In order to quantify the thickness uniformity of various layers, the thickness of each layer has been measured at 26 locations over an 11” × 11” area using an optical method (Rudolph Thickness Monitor). The measurements have been made for layers both before and after the cathode change. Two independent quantities have been used for this analysis:

- hi-lo (%) = (maximum thickness – minimum thickness) / maximum thickness, and
- coefficient of variation of thickness distribution: CV (%) = standard deviation/average.

For component cell studies, stainless steel substrate with no back reflector is used for fabricating the a-Si:H top and a-SiGe:H middle cells. For the a-SiGe:H bottom cell and the final a-Si:H/a-SiGe:H/a-SiGe:H triple-junction structure, a textured Al/ZnO back reflector layer on stainless steel substrate is used for device fabrication. The deposition of the back reflector and a-Si:H and a-SiGe:H layers are made over an area of ~1 sq. ft. Conventional RF glow discharge technique is used for the semiconductor deposition. The completed large-area device is cut into several ~2”×2” pieces representing a 10”×10” area. The transparent Indium-Tin-Oxide (ITO) is deposited through an evaporation mask to yield an array of devices of total area 0.268 cm^2. These devices are used for J-V and QE measurements.

2.3. Layer thickness uniformity

Figure 1 shows hi-lo uniformity of various layers over an 11” × 11” area. The new cathode exhibits significantly improved hi-lo uniformity from ~55% to ~23%. Figure 2 shows uniformity distribution based on CV. The new cathode exhibits superior CV uniformity from ~22% to ~8%. Table I summarizes the average uniformity data of individual layers using both cathodes. Note that these are the average of all the values of hi-lo and CV uniformity as obtained from Figs. 1 and 2. Clearly, the average uniformity values are superior for the new cathode.

Table I: Average uniformity data of individual layers for standard and new cathodes.

Layer	Cathode	Hi - Lo (11" x 11")	CV (11" x 11")
I1	Standard	54%	22.5%
	Pore	**24%**	**10%**
I2	Standard	46%	17.9%
	Pore	**23%**	**8%**
I3	Standard	55%	21.3%
	Pore	**23%**	**8.5%**
N3	**Pore**	**21%**	**7.0%**
B1	Standard	49%	19.6%

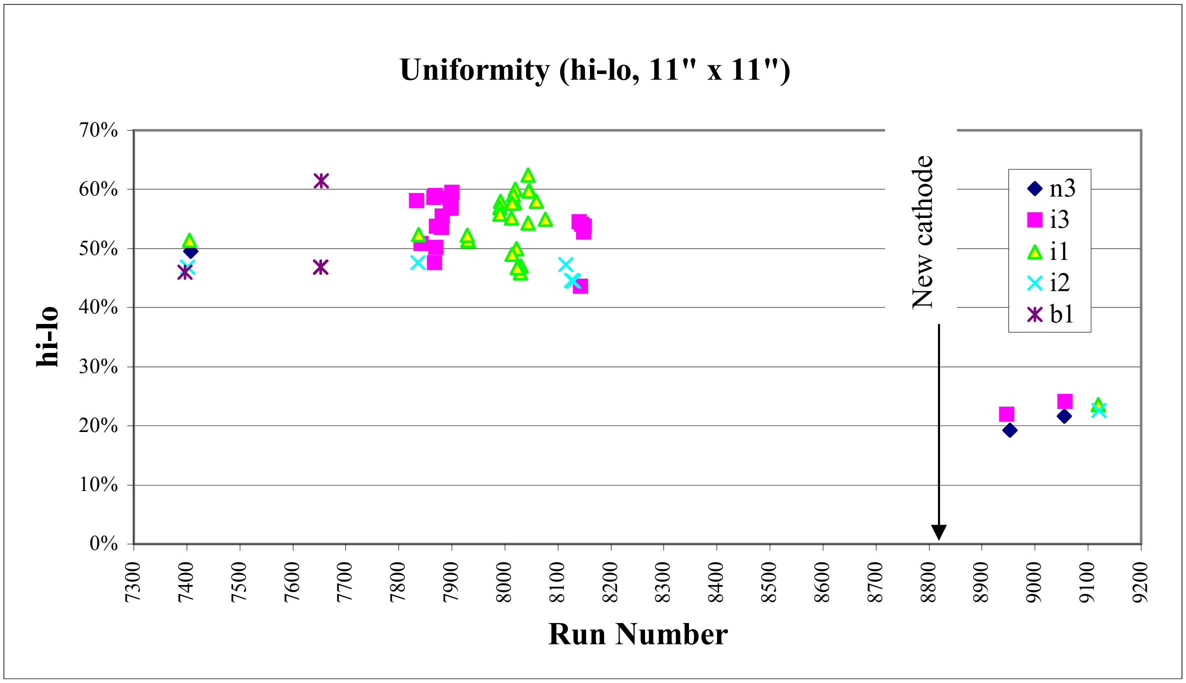

Figure 1. hi-lo uniformity over 11” × 11” before and after use the new cathode.

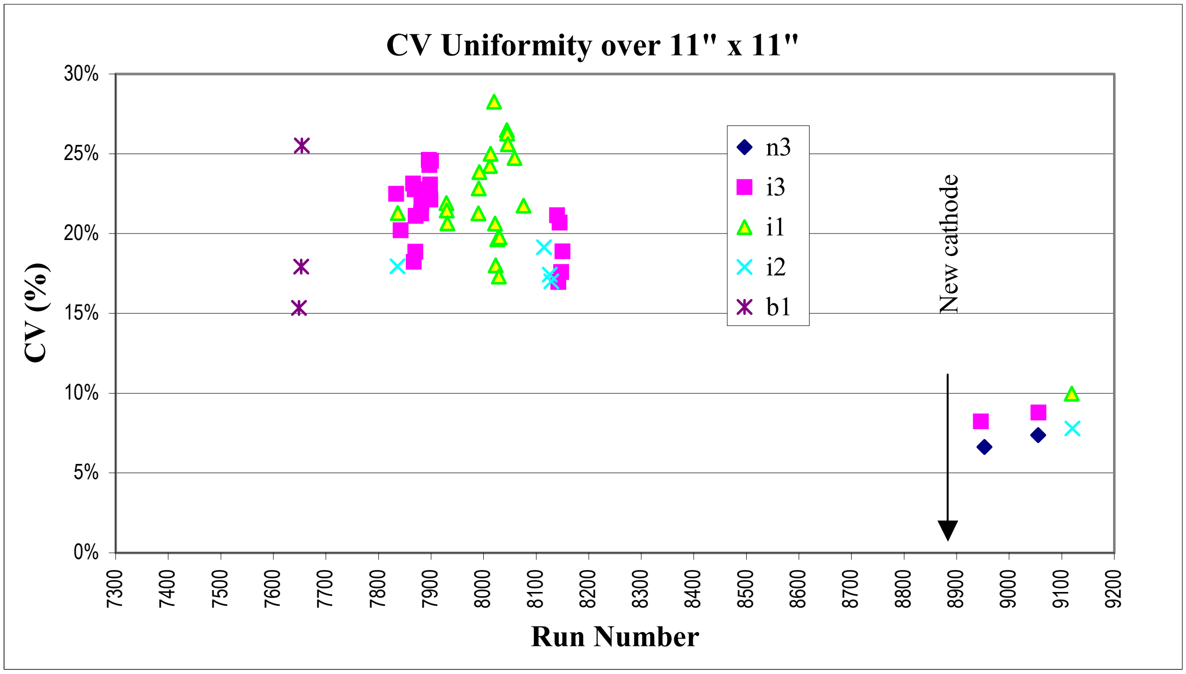

Figure 2. CV uniformity over 11” × 11” before and after use the new cathode.

2.4. Design of Experiments (DOE)

In order to improve the thickness uniformity we have undertaken to use the DOE technique. We have carried out a series of experiments using Taguchi Robust Design of Experiments (orthogonal arrays). Preliminary results indicate that there is scope for further improvement in the thickness uniformity distribution. In fact, even within the first DOE, some layers already provided significantly better uniformity than what we had ever achieved before. For example, the best uniformity we had ever realized for the a-SiGe:H intrinsic layer in the bottom cell (I1) was 10% (based on CV); in the DOE, one of the depositions reduced the thickness distribution to 5.9%.

2.5. Uniformity of component cell performance

2.5.1. Top cell on stainless steel substrate

Seven ~2”×2” pieces of the top cell, representing the large-area 10”×10” stainless steel substrate with no back reflector, were selected. The J-V characteristics were measured using AM1.5 illumination. The initial performance of devices and their average values are listed in Table II. Each value in the table represents the average of two 0.268 cm^2 devices on that substrate. The best average total-area efficiency is ~6.4% for sample RLC1 while the average of all cells on the seven pieces is 6.16%. The standard deviation and coefficient of variation of the seven samples are also listed at the bottom of Table II. The standard deviation is 0.24, and the coefficient of variation is 3.8%.

Table II: Initial performance of top cells measured over a10"×10" deposition area.

Sample	Substrate	Area	Source	Efficiency	J_{sc}	V_{oc}	FF	R_s
2B9117		(cm^2)		(%)	(mA/cm^2)	(V)		$\Omega.cm^2$
LN	SS	0.268	1.5	5.75	7.63	1.003	0.751	6.4
LLC1	SS	0.268	1.5	6.36	8.55	1.004	0.741	7.0
LS	SS	0.268	1.5	6.25	8.47	0.999	0.738	8.3
RN	SS	0.268	1.5	6.06	8.14	1.005	0.741	8.5
RLC1	SS	0.268	1.5	6.42	8.62	1.006	0.742	7.6
RS	SS	0.268	1.5	6.29	8.45	1.006	0.741	8.1
LC1	SS	0.268	1.5	6.02	8.42	0.997	0.717	10.2
Average				**6.16**	**8.33**	**1.003**	**0.738**	**8.0**
Standard Deviation				**0.24**	**0.34**	**0.003**	**0.011**	**1.21**
Coefficient of Variation				**3.83%**	**4.10%**	**0.34%**	**1.42%**	**15.13%**

2.5.2. Middle cell on stainless steel substrate

Similar work has been done on the middle cell on a stainless steel substrate with no back reflector. Nine representative ~2”×2” pieces with 0.268 cm^2 total-area devices were prepared. The initial performance of the devices was measured under AM1.5 illumination using a 530-nm cut-on filter, as listed in Table III. The average values of total-area P_{max} at wavelength >530 nm of the nine substrates are in the range of 3.11-3.45 mW/cm^2. Sample LLC1 exhibits the best

Table III: Initial performance of middle cells measured over a 10" × 10" deposition area.

Sample	Substrate	Area	Source	P_{max}	J_{sc}	V_{oc}	FF	R_s
2B9179		(cm^2)	(nm)	(mW/cm^2)	(mA/cm^2)	(V)		$\Omega.cm^2$
LN	SS	0.268	530	3.28	6.99	0.690	0.685	9.7
LLC1	SS	0.268	530	3.45	7.42	0.678	0.687	8.4
LS	SS	0.268	530	3.23	7.29	0.673	0.658	9.3
RN	SS	0.268	530	3.18	7.40	0.668	0.644	11.1
RLC1	SS	0.268	530	3.25	7.19	0.674	0.671	9.7
RS	SS	0.268	530	3.24	7.31	0.673	0.659	11.2
N	SS	0.268	530	3.17	6.88	0.680	0.677	8.7
LC1	SS	0.268	530	3.19	6.75	0.683	0.691	8.9
S	SS	0.268	530	3.11	6.62	0.683	0.688	8.9
Average				**3.23**	**7.10**	**0.678**	**0.673**	**9.5**
Standard Deviation				**0.10**	**0.29**	**0.01**	**0.02**	**1.01**
Coefficient of Variation				**2.99%**	**4.12%**	**0.99%**	**2.45%**	**10.56%**

performance. The average performance is 3.2 mW/cm^2. The standard deviation and coefficient of variation of the nine samples are also listed at the bottom of Table III. The standard deviation is 0.10 and the coefficient of variation is ~2.99%.

2.5.3. Bottom cell on Al/ZnO back reflector

For the bottom cell, an Al/ZnO back reflector substrate has been used. Seven representative ~2”x2” pieces with 0.268 cm^2 total-area devices were prepared. The initial performance of the devices was measured under AM1.5 illumination using a 610 nm cut-on filter, as listed in Table IV. The P_{max} at wavelength>610 nm for the best bottom cell is 3.08 mW/cm^2 while the average of all the cells is 2.99 mW/cm^2.

Table IV: Initial performance of bottom cells measured over a 10" × 10" deposition area.

Sample	Substrate	Area	Source	P_{max}	J_{sc}	V_{oc}	FF	R_s
2B9170		(cm^2)	(nm)	(mW/cm^2)	(mA/cm^2)	(V)		$\Omega.cm^2$
LN	Al/ZnO	0.268	610	3.08	8.14	0.595	0.636	10.5
LLC1	Al/ZnO	0.268	610	3.06	8.82	0.573	0.606	10.6
LS	Al/ZnO	0.268	610	2.97	7.85	0.591	0.639	10.1
RN	Al/ZnO	0.268	610	3.00	7.47	0.613	0.656	10.7
RLC1	Al/ZnO	0.268	610	2.94	7.53	0.604	0.647	10.2
RS	Al/ZnO	0.268	610	3.05	7.83	0.606	0.643	11.6
LC1	Al/ZnO	0.268	610	2.83	8.29	0.568	0.600	10.1
Average				2.99	7.99	0.593	0.632	10.5
Standard Deviation				0.09	0.47	0.02	0.02	0.53
Coefficient of Variation				2.97%	5.91%	2.86%	3.35%	4.98%

2.5.4. a-Si:H/a-SiGe:H/a-SiGe:H triple-junction structure on Al/ZnO back reflector

For a-Si:H/a-SiGe:H/a-SiGe:H triple-junction solar cells with production constraints, we have achieved an initial efficiency of 11.2%. This result was achieved with (i) the new cathode design that resembles the one on the production line; (ii) a back reflector obtained from the production line, and (iii) a SiH_4 and GeH_4 mixture instead of a Si_2H_6 and GeH_4 mixture. Table V lists the individual solar cell parameters in the initial and stable (100 mW/cm^2 white light illumination for 1070 hours) states. The overall degradation loss is seen to be 12.5% comprising losses in FF (6.9%), V_{oc} (4.2%), and J_{sc} (1.3%). The stable active-area efficiency is 9.83%. This corresponds to a stable total-area efficiency of 9.1% and ties with the previous record made with a Si_2H_6 and GeH_4 mixture. Figure 3 shows the (a) J-V characteristics and (b) QE of this solar cell.

Table V: The initial and stable performance of the a-Si:H/a-SiGe:H/a-SiGe:H triple cell deposited under production constraints.

Run No.	State	V_{oc} (V)	FF	J_{sc} (mA/cm^2)	QE (mA/cm^2)				P_{max} (mW/cm^2)
					Top	Mid.	Bot.	Total	
9619 S	Initial	2.198	0.736	6.94	7.19	7.55	6.94	21.69	11.23
	Stable	2.104	0.682	6.85	7.07	7.29	6.85	21.20	9.83
	Degr.	4.23%	6.93%	1.3%	1.67%	3.44%	1.3%	2.26%	12.5%

2.6. Summary

We have designed, fabricated, and installed a new cathode in our 2B large-area deposition system. The new cathode has improved the film thickness and cell performance significantly. Using the new cathode, we have focused on the optimization of a-Si:H and a-SiGe:H component cells as well as the a-Si:H/a-SiGe:H/a-SiGe:H triple-junction structures using a SiH_4/GeH_4 mixture instead of the traditional Si_2H_6/GeH_4 mixture. We have optimized the deposition process and achieved a similar cell performance for the SiH_4/GeH_4 mixture as the previous Si_2H_6/GeH_4 mixture.

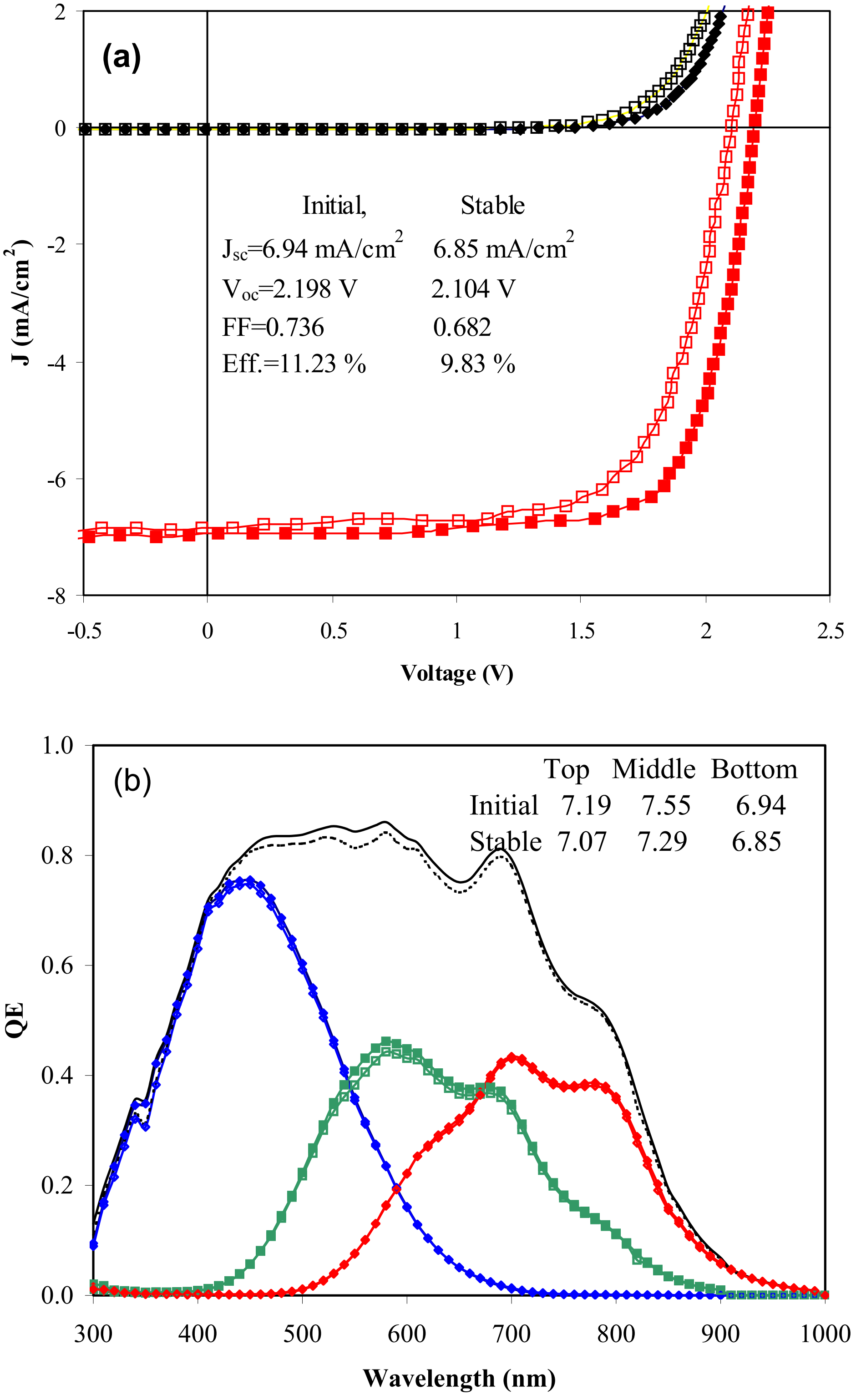

Figure 3. (a) J-V characteristics and (b) quantum efficiency of an a-Si:H/a-SiGe:H/a-SiGe:H triple-junction solar cell before and after 1000 hours of light soaking.

Section 3: Fundamental Study of nc-Si:H and Optimization of High Efficiency nc-Si:H Solar Cells

3.1. Introduction

One of the objectives of this program is to explore the highest achievable efficiency using a-Si:H based thin film solar cell technology. To date, the highest stable efficiency of 13% has been achieved using an a-Si:H/a-SiGe:H/a-SiGe:H triple-junction structure [1]. a-SiGe:H has a higher defect density than a-Si:H. nc-Si:H was found to be a potential substitute for the a-SiGe:H bottom cell since it offers a higher current density and a better stability under prolonged illumination than a-SiGe:H [12, 13]. The bandgap of nc-Si:H with a high crystalline volume fraction (f_c) is normally close to 1.1 eV, which is the same value as crystalline silicon. Therefore, nc-Si:H solar cells generally have a higher short-circuit current density (J_{sc}), but a lower V_{oc} than a-Si:H and a-SiGe:H cells. Due to the nature of the indirect optical transition in the crystalline phase of this material, a relative thick intrinsic nc-Si:H layer is required for obtaining a high J_{sc}. Normally, the intrinsic nc-Si:H layer in an *n-i-p* structure is over 1 μm thick, and sometimes it needs to be a few μm thick, which not only requires a high deposition rate to be considered for manufacturing, but also causes many issues in optimizing material properties and device design. First, the deposition conditions are different for making a-Si:H and nc-Si:H. A very high hydrogen dilution reduces the deposition rate. In order to achieve a high deposition rate, new deposition methods and deposition parameters have to be explored. In the literature, two methods have been widely used for high rate deposition of nc-Si:H solar cells, namely, very high frequency (VHF) glow discharge [12, 13] and RF glow discharge with high pressure and high power at the silane depletion regimes [18 – 20]. In this section, we present the results for nc-Si:H cells made primarily using conventional RF glow discharge at low rates. Although the low rate deposition will not be used in manufacturing, it can help us to understand the issues related to the nc-Si:H material properties and solar cell design.

3.2. Experimental

A multi-chamber RF system (Line System) has been used to deposit a-Si:H, a-SiGe:H, and nc-Si:H materials and solar cells. For comparison, nc-Si:H solar cells were also made using modified very high frequency (MVHF) glow discharge at high rates. The a-Si:H top and a-SiGe:H middle cells were deposited on specular stainless steel substrates. The component nc-Si:H bottom cell was deposited on stainless steel and on Al/ZnO or AgZnO back reflectors to enhance the long-wavelength absorption. ITO dots with a total-area of 0.268 cm^2 were deposited on the *p* layer, and metal grid fingers were deposited for the top contact. The active-area of the cells is 0.25 cm^2. The solar cell performance was measured under an AM1.5 solar simulator at 25 °C and QE curves were measured from 300 to 1000 nm at room temperature and used as a calibration for J_{sc}. In order to check the individual cell performance in the double-junction structure, the light J-V characteristics were also measured under an AM1.5 solar simulator with a 610 nm cut-on filter and a 585 nm cut-off filter.

The structural properties of nc-Si:H films and solar cells have been characterized by photoluminescence (PL), Raman spectroscopy (D. Han's group at University of North Carolina), X-ray diffraction (XRD) and small angle X-ray diffraction (SAXS) (D. Williamson at the Colorado School of Mines), and Atomic Force Microcopy (AFM) (C.-S. Jiang at NREL). The electronic properties and defect distributions were measured using drive-level capacitance, transient photocapacitance, and transient photocurrent spectroscopy (D. Cohen's group at Oregon University). These characterizations provide useful information for understanding the material properties and their correlation to cell performance. The major results have been or will be reported by the collaborators and only limited results will be presented in this report. The device properties were also characterized by dark current-voltage (J-V) measurements at different temperatures.

3.3. Thickness dependence of nc-Si:H solar cells

As mentioned before, the advantages of nc-Si:H cells over a-SiGe:H cells are higher J_{sc} and minimal light-induced degradation. However, some unsolved issues still limit the further improvement of cell efficiency. One big drawback is the lower V_{oc}, which is normally lower than 0.5 V for the cells with high J_{sc} (e.g. > 24 mA/cm^2). In order to improve the cell efficiency further, we need to understand the limitations of V_{oc} in nc-Si:H solar cells. For this purpose, we studied the thickness dependence of nc-Si:H single-junction solar cells.

Figure 4 shows the J-V parameters of the solar cells as a function of the intrinsic layer thickness. It was observed that J_{sc} increases but FF decreases with the increase of the intrinsic layer thickness. This phenomenon is similar to that observed in a-Si:H silicon solar cells. For a thicker cell, a higher J_{sc} results from a higher optical absorption, and a lower FF from a reduced collection. A considerable difference from a-Si:H solar cells is that V_{oc} decreases significantly with intrinsic layer thickness. In a-Si:H solar cells, the V_{oc} also decreases with intrinsic layer thickness, but the change is normally very small unless nanocrystalline formation occurs. For the nc-Si:H cells shown in Fig. 4, the V_{oc} decreases dramatically with the intrinsic layer thickness. Although we do not fully understand what causes the thickness dependence of V_{oc} at this time, we have considered a few possible mechanisms. First, it is known that the amount of nanocrystalline inclusion (grain size and crystalline volume fraction) increases with film thickness if the deposition conditions remain the same during deposition. We have also found that V_{oc} decreases with an increase of H_2 dilution. Therefore, with the increase of the nanocrystalline portion, V_{oc} varies from over 1.0 V in the fully a-Si:H phase to below 0.5 V in substantially nanocrystalline phase. The mixed-phase solar cells have V_{oc}'s in between, depending on the amount of crystalline volume fraction [9, 10]. Based on the two observations, we conclude that a thicker nc-Si:H cell has a higher average crystalline volume fraction, hence, lower V_{oc}. Second, for nc-Si:H cells with an intrinsic layer thickness of around 1 μm, its V_{oc} is normally below 0.5 V, which is much lower than that of crystalline silicon solar cells. Although we may consider grains to have a similar bandgap as crystalline silicon, the distorted bonds in the grain boundary regions lead to an increase in bandtail states and cause a lower V_{oc}. In addition, impurity is another issue. We found a significant amount of oxygen impurity

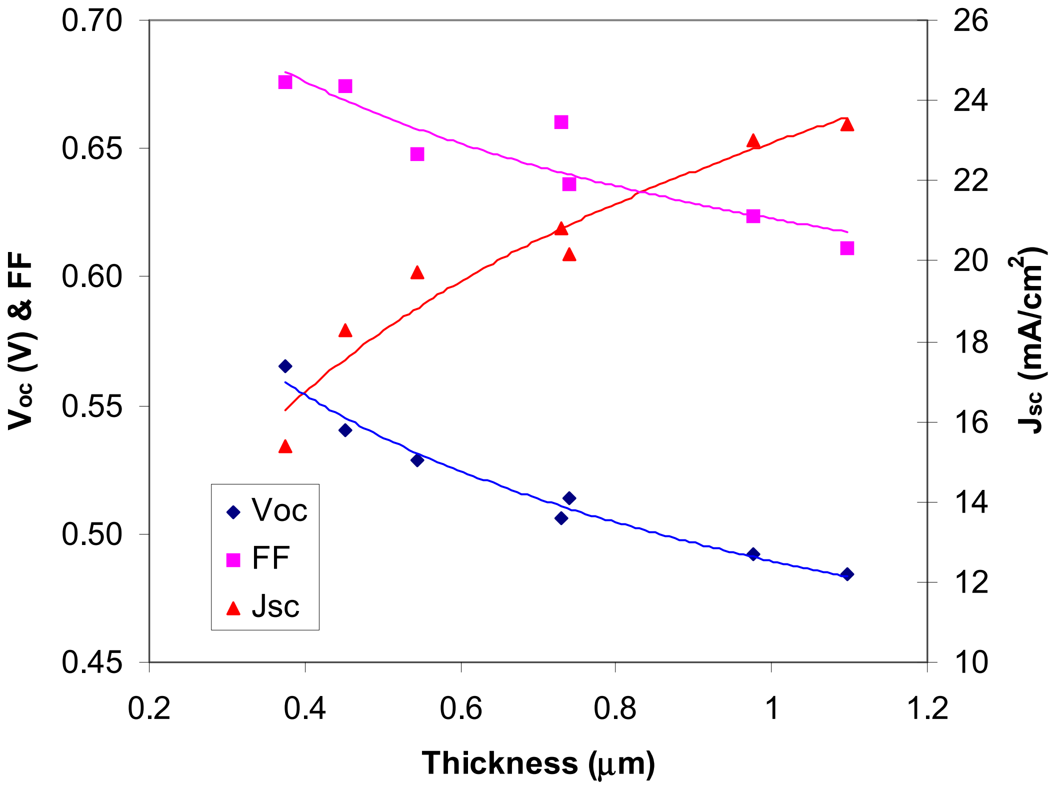

Figure 4. J-V characteristics of nc-Si:H single-junction solar cells versus the intrinsic layer thickness.

in unoptimized nc-Si:H silicon films. Even for optimized nc-Si:H films, SIMS analysis showed a large tail diffusing into the film.

Oxygen atoms can form *n*-type doping centers, which shift the Fermi level toward the conduction band and lead to a high dark conductivity. In an *n-i-p* structure, a higher dark conductivity causes a higher dark current density and a lower V_{oc}. Since we found that the post-deposition impurity diffusion can be blocked by an a-Si:H layer, the oxygen problem is not a major issue for multi-junction solar cells, but the incorporation of oxygen during the deposition is still a concern.

Based on the above results, it is clear that the challenge is to understand the thickness dependence of cell performance and to fabricate thick nc-Si:H solar cells that yield high J_{sc} without affecting V_{oc} and FF. However, for thick nc-Si:H solar cells, the J_{sc} may not increase with intrinsic layer thickness. In general, the J_{sc} increases with intrinsic layer thickness in a given range. For a particular nc-Si:H solar cell, it has been reported that the intrinsic nc-Si:H layer was as thick as 4-5 μm thick. However, we find that under our current deposition condition, the J_{sc} reaches a maximum at around 22-24 mA/cm^2 with a thickness around 1 to 1.2 μm. Increasing the thickness further leads to a decrease in J_{sc}, caused by a reduction of spectral response in the long wavelength region. Two mechanisms could be responsible for the low J_{sc} for thick nc-Si:H solar cells. One possibility is nanocrystallite collision due to the textured substrate [21, 22]. It has been reported that grains in the nc-Si:H films deposited on a textured substrate grow perpendicular to the local substrate surface and collide with each other when the film exceeds a certain thickness. Thus, crystallite collision results in a high defect density at the grain boundaries and, therefore, low cell performance. A second possible mechanism is the increase of crystalline volume fraction (f_c) and grain size with film thickness. A high value of f_c could cause poor grain boundary passivation, high microvoid density, and poor cell performance [23, 24].

In order to distinguish the two mechanisms, we have done a few systematic studies including nc-Si:H cell performance as a function of intrinsic layer thickness for cells on different substrate. The same experiments have been performed several times. Here, we present a set of experimental data from the MVHF system at high rates. Two sets of nc-Si:H single-junction solar cells were made using MVHF glow discharge with different intrinsic layer thicknesses. One set was made on textured Ag/ZnO coated stainless steel (BR), and another on specular stainless steel (SS). The same growth recipe was used for both sets of solar cells on the two different substrates. The thickness of the samples was obtained using an optical method. The thickness showed a linear dependence on deposition time and confirmed a constant deposition rate. We found that the deposition rates are the same on SS and BR. The reason for comparing nc-Si:H cells deposited on SS and BR is that on a flat substrate (SS), the cell performance would not have the problem of crystallite collision that is expected to happen on textured BR. Thus, we can expect less deterioration of cell performance with an increase of thickness.

Table VI lists the J-V characteristics of nc-Si:H solar cells deposited on BR substrates with different intrinsic layer thicknesses. One can see that the J_{sc}, calibrated by quantum efficiency measurements, increases with increasing thickness up to 1 μm and then saturates. For the cell with a thickness around 2 μm, J_{sc} is actually lower than that of the cell with a thickness

Table VI: J-V characteristics of nc-Si:H cells deposited using MVHF on Ag/ZnO BR with different thicknesses, where FF_b and FF_r represent, respectively, the fill factor under blue and red light.

Run No.	Thickness (nm)	J_{sc} (mA/cm^2)	V_{oc} (V)	FF	P_{max} (mW/cm^2)	FF_b	FF_r
12116	290	16.41	0.503	0.638	5.27	0.620	0.610
12120	490	19.77	0.476	0.633	5.96	0.626	0.636
12121	940	23.25	0.443	0.585	6.03	0.617	0.620
12119	990	22.47	0.436	0.612	6.00	0.628	0.619
12122	1340	23.23	0.424	0.533	5.25	0.568	0.597
12124	1930	21.80	0.392	0.491	4.20	0.521	0.569

around 1 µm. As is usually observed, both the V_{oc} and FF decrease monotonically with increasing thickness. The overall cell efficiency reaches a maximum with a thickness around 1 µm. Figure 5 (a) plots the quantum efficiency (QE) of the six cells. One can see that for cells with a thin nc-Si:H intrinsic layer, the long wavelength response increases with cell thickness; but for the cell with a thick intrinsic layer around 2 µm, the response at the middle and long wavelength region is lower than that in the 1 µm thick cells. The remarkable increase of quantum efficiency under reverse bias indicates an insufficient collection, which can be related to excess recombination through defects in the intrinsic layer.

Table VII lists the J-V characteristics of the nc-Si:H solar cells on SS made with the same recipe as the corresponding cells deposited on BR, which are listed in Table VI. One can see that the behaviors of the V_{oc} and FF versus thickness are similar for cells on SS as for those on BR, but that J_{sc} keeps increasing up to the thickness of ~ 2 µm. Moreover, compared to cells of the same thickness on BR, the cells on SS have smaller J_{sc} and V_{oc}, but higher FF. From Fig. 5 (b), one can see the continued increase of the long wavelength response with thickness. The difference between the reverse biased quantum efficiency and the quantum efficiency under the short-circuit condition is much smaller for the 2 µm cell on SS than on BR. This implies that the cells on SS have fewer problems with carrier collection than on BR.

Table VII: J-V characteristics of nc-Si:H solar cells deposited using MVHF on SS with different thicknesses, where FF_b and FF_r represent, respectively, the fill factor under blue and red light.

Run No.	Thickness (nm)	Q (mA/cm^2)	V_{oc} (V)	FF	P_{max} (mW/cm^2)	FF_b	FF_r
12129	335	9.45	0.47	0.651	2.89	0.650	0.668
12125	470	10.98	0.466	0.672	3.44	0.664	0.67
12127	720	12.99	0.439	0.64	3.65	0.608	0.627
12123	1040	14.8	0.434	0.621	3.99	0.649	0.655
12128	1305	16.51	0.414	0.578	3.95	0.615	0.632
12126	1980	17.87	0.393	0.51	3.58	0.584	0.612

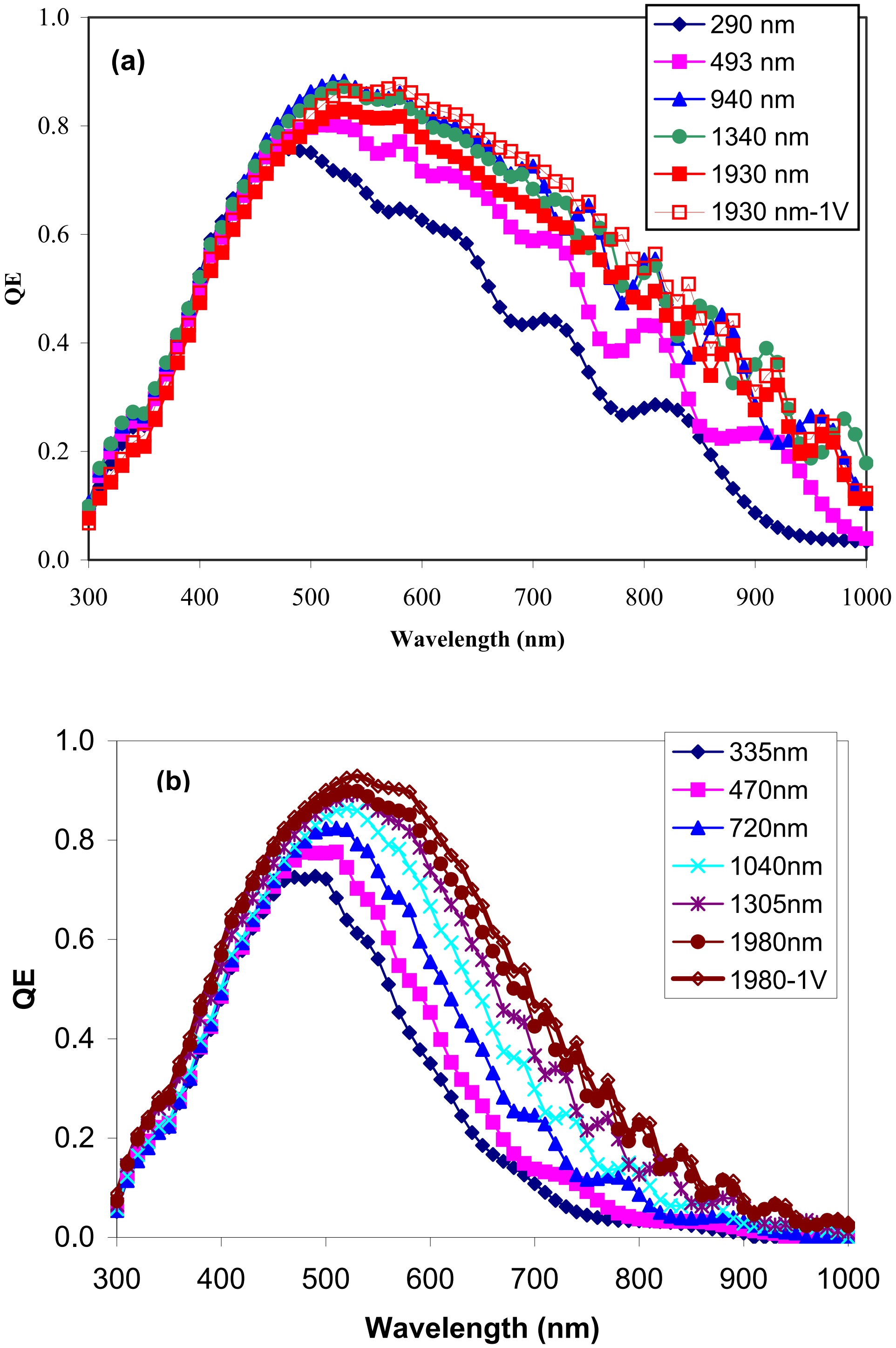

Figure 5. Quantum efficiency of nc-Si:H cells deposited using MVHF on (a) BR and on (b) SS with different thicknesses.

Table VIII: Comparison of the solar cell performances with different substrates. For the measurements of the solar cells on BR, the light intensity was adjusted to have a J_{sc} similar to the solar cells on SS using neutral density filters.

Thickness (nm)	Substrate	J_{sc} (mA/cm^2)	V_{oc} (V)	FF	P_{max} (mW/cm^2)
470	BR	11.7	0.451	0.646	3.42
	SS	11.8	0.467	0.669	3.69
1040	BR	15.4	0.421	0.636	4.12
	SS	15.6	0.435	0.623	4.22
1305	BR	17.0	0.413	0.551	3.88
	SS	17.5	0.416	0.579	4.22
1980	BR	18.7	0.385	0.501	3.61
	SS	18.8	0.395	0.508	3.76

Due to a lower reflectance and a lower light trapping effect from the specular SS substrate, the light absorption of the cells on SS is much less than that on BR even with the same thickness. This leads to a smaller J_{sc}, which causes a narrower quasi-Fermi level splitting and gives rise to a lower V_{oc}. Furthermore, the narrower quasi-Fermi level splitting reduces the recombination rate of the excited carriers, which yields a higher FF for cells on SS and hence, a smaller difference between the zero and negatively biased quantum efficiency. A fair comparison of V_{oc} and FF for cells on different substrates would be under similar J_{sc}, instead of under the same light intensity.

In this case, we may expect a similar splitting of the quasi-Fermi levels. For this purpose, the solar cells on BR were re-measured with reduced light intensities by using neutral density filters to generate similar current densities to those in the solar cells on SS. Table VIII lists J-V characteristics of four pairs of solar cells with different thicknesses. The two cells in each pair have a similar thickness, but one is on BR and the other on SS. One can see that when the solar cells on BR were adjusted to have J_{sc}'s similar to those on SS, the V_{oc} and FF also became very similar. This indicates that the BR substrate used at our lab does not have a pronounced effect on the carrier transport in the nc-Si:H solar cells. In conclusion, we found that the nanocrystallite collision for cells on BR could be a limitation of low J_{sc}, but it is not the main factor. Therefore, the other mechanism, which is the increase of crystalline volume fraction, could be responsible for the low J_{sc} in the thicker nc-Si:H solar cells.

3.4. Microstructure changes with thickness in nc-Si:H solar cells

As shown in the previous section, the evolution of crystallinity with thickness is probably the dominant contribution for the deterioration of cell performance with intrinsic layer thickness in our nc-Si:H solar cells. Although the collision of nanocrystallites may be present to some extent in the *n-i-p* type cells on the textured Ag/ZnO BR, it is not the limiting factor. The increase of crystalline volume fraction and grain size has been well documented in the literature [25, 26]. However, the properties of nc-Si:H material depend on deposition conditions and cells structures. In order to understand the increase of crystalline volume fraction and grain size with the intrinsic layer thickness, we have studied the microstructures of the nc-Si:H solar cells using Raman spectroscopy at the University of North Carolina at Chapel Hill, small angle X-ray scattering (SAXS) and X-ray diffraction (XRD) at Colorado School of Mines, and Atomic Force Microscopy (AFM) at NREL.

A 514.5-nm laser was used as an excitation source for obtaining the Raman scattering spectra. The measurements were made on the nc-Si:H cells on Ag/ZnO BR. The upper plot in Fig. 6 shows an example of the Raman spectra of nc-Si:H solar cells, where the curve can be decomposed into three components: i) a very sharp peak at 515-520 cm^{-1} from the crystalline phase, ii) the middle term located at 490-500 cm^{-1} and assigned to grain boundaries or intermediate order, and iii) a broad peak at 480 cm^{-1} from the amorphous regions. A calculation using the intensity ratios of the three peaks gives an average of the crystalline volume fraction in the absorption depth probed by the excitation source. The lower plot in Fig. 6 shows the thickness dependence of the crystalline volume fraction for the cells made on Ag/ZnO BR. It clearly shows the increase of crystalline volume fraction from 60% to 80% when the thickness is increased from 0.3 μm to 2.0 μm.

The two sets of nc-Si:H solar cells were also characterized by XRD. As shown in Fig. 7, all three XRD peaks increase dramatically with the increase of thickness, but the (220) peak grows faster than the (111) and (311) peaks as illustrated by the top plot in Fig. 8. This demonstrates enhanced (220) preferred orientation with increasing thickness but shows this effect to be reduced on the BR substrate, consistent with the crystallite collisional growth mechanism. Analysis of the (220) linewidths yields increasing grain size with thickness, but the grain sizes are clearly smaller for the BR series compared to the SS series, suggesting grain collisions reduce grain size for a given film thickness. The lower plot of Fig. 8 shows that the XRD integrated intensity (sum of (111), (220), and (311) peaks) grows faster than a linear trend. This is consistent with increasing crystalline volume fraction with thickness. The larger integrated intensities for the SS series is likely due to the enhanced (220) preferred orientation shown in the upper plot of Fig. 8. Also, the nature of the substrate is known to play a role in the amorphous to nanocrystalline transition [27].

Figure 9 shows the AFM images of two samples on SS substrate, one with a thickness of 0.3 μm and the other with a thickness of 2.0 μm. The images clearly show the increases in the size of the surface micro-features as well as the surface roughness. Similar results were observed on the samples deposited on Ag/ZnO, but with complex features due to the substrate texture. Figure 10 plots the surface roughness defined as the root mean square (RMS) versus the cell thickness of the samples on BR and SS substrates. For the samples on SS, the roughness monotonically increases with increasing thickness, which is likely related to the evolution of the nanocrystallites in nc-Si:H. However, for the cells on BR, the roughness also increases with thickness, but the total roughness is dominated by the surface of the substrate.

In summary, we have investigated the effect of the substrate and thickness on nc-Si:H solar cell performance. We found that the BR substrate has certain influence on the cell performance and material structure, but it is not the main reason for the low J_{sc} of thick nc-Si:H solar cells at the current stage. Therefore, we believe that the increasing volume fraction of nc-

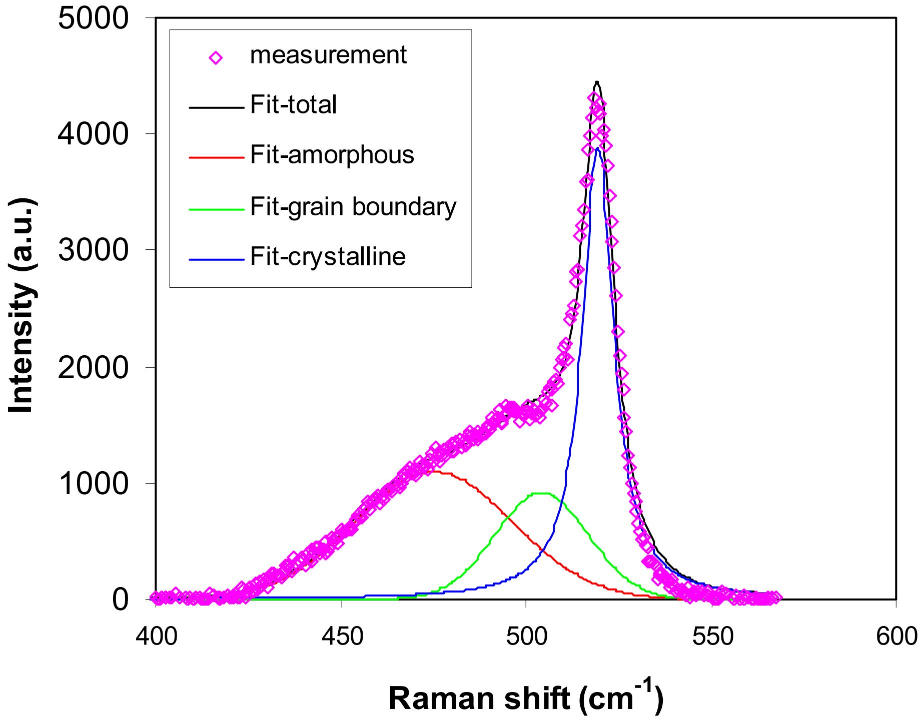

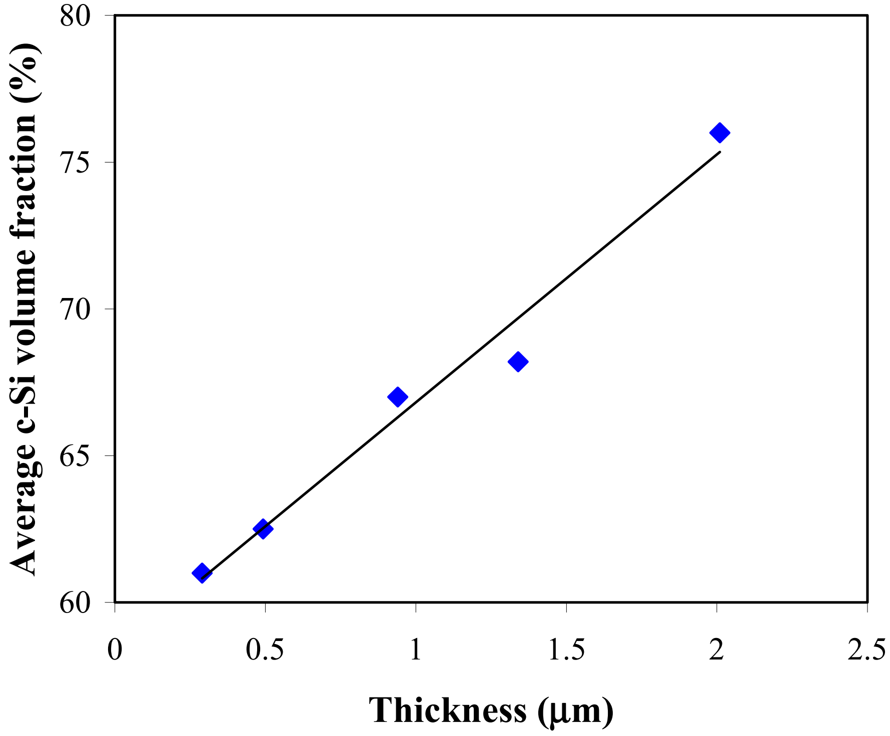

Figure 6. (upper) Raman spectrum of a nc-Si:H solar cell with three components of the decomposition and (lower) the average crystalline volume fraction versus cell thickness.

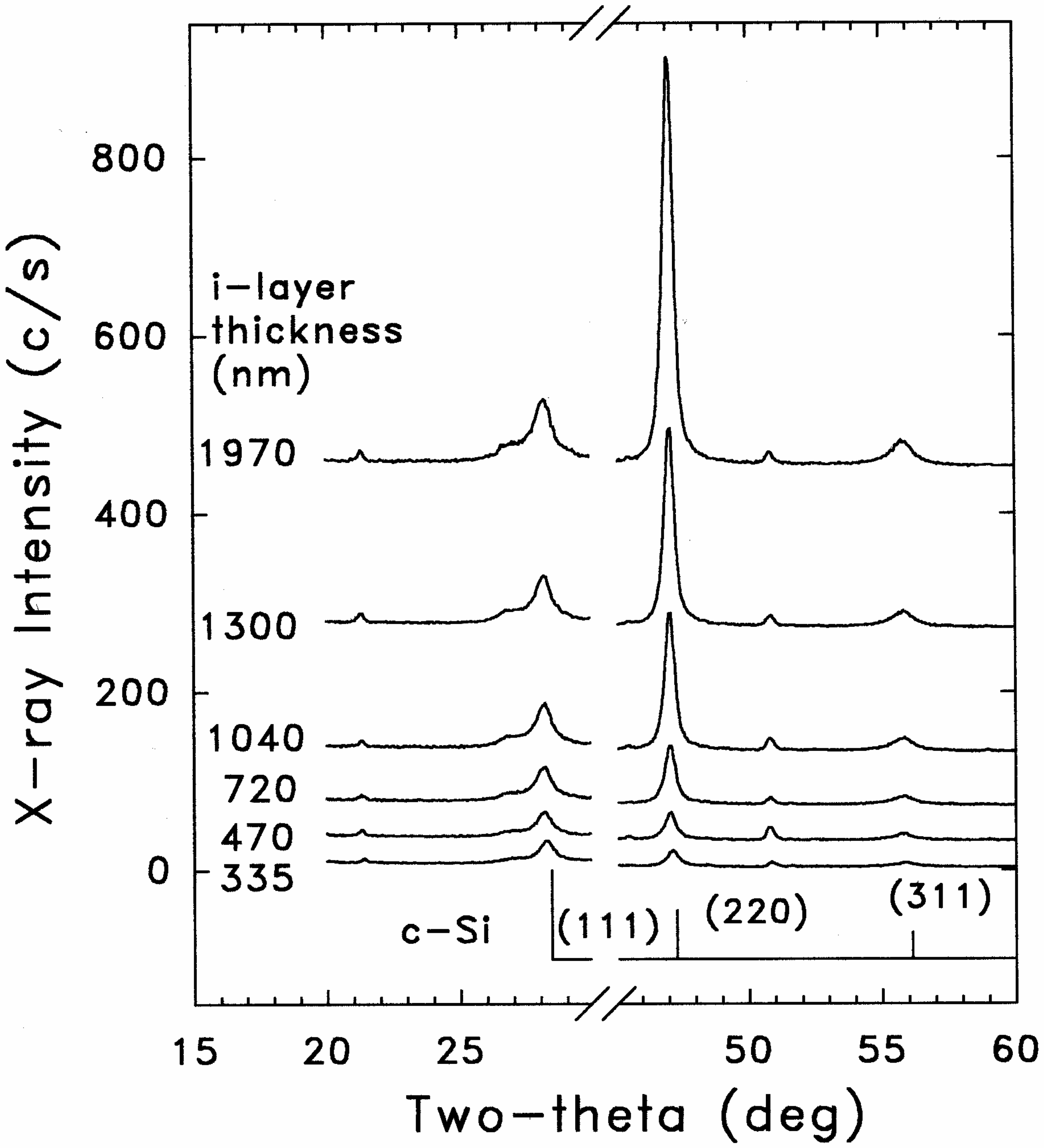

Figure 7. XRD patterns from the nc-Si:H solar cells on SS with different thicknesses. Stick diagram of c-Si random powder pattern is also shown.

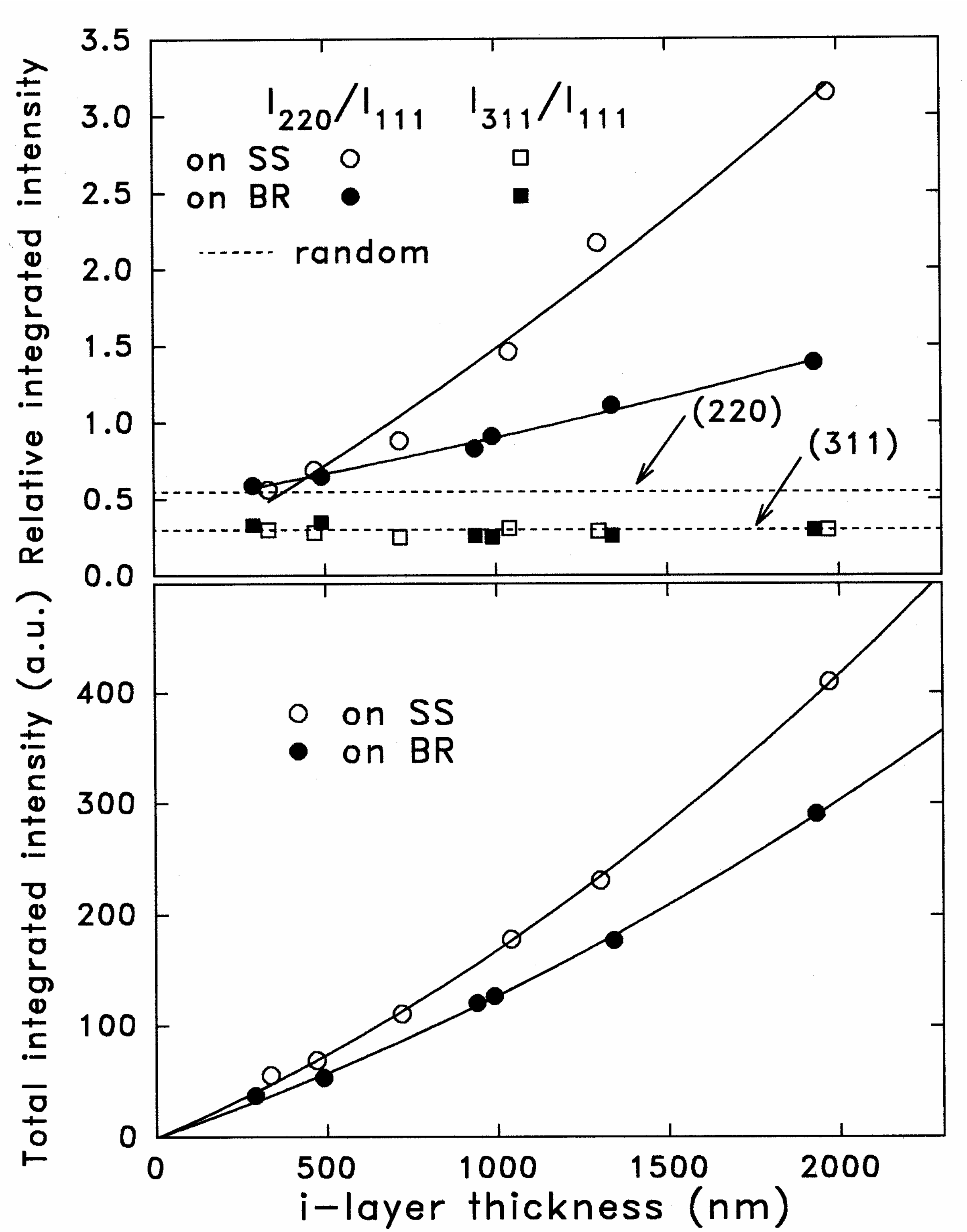

Figure 8. (upper) Relative and (lower) total integrated XRD intensities for the nc-Si:H solar cells. Solid lines were drawn to guide the eye.

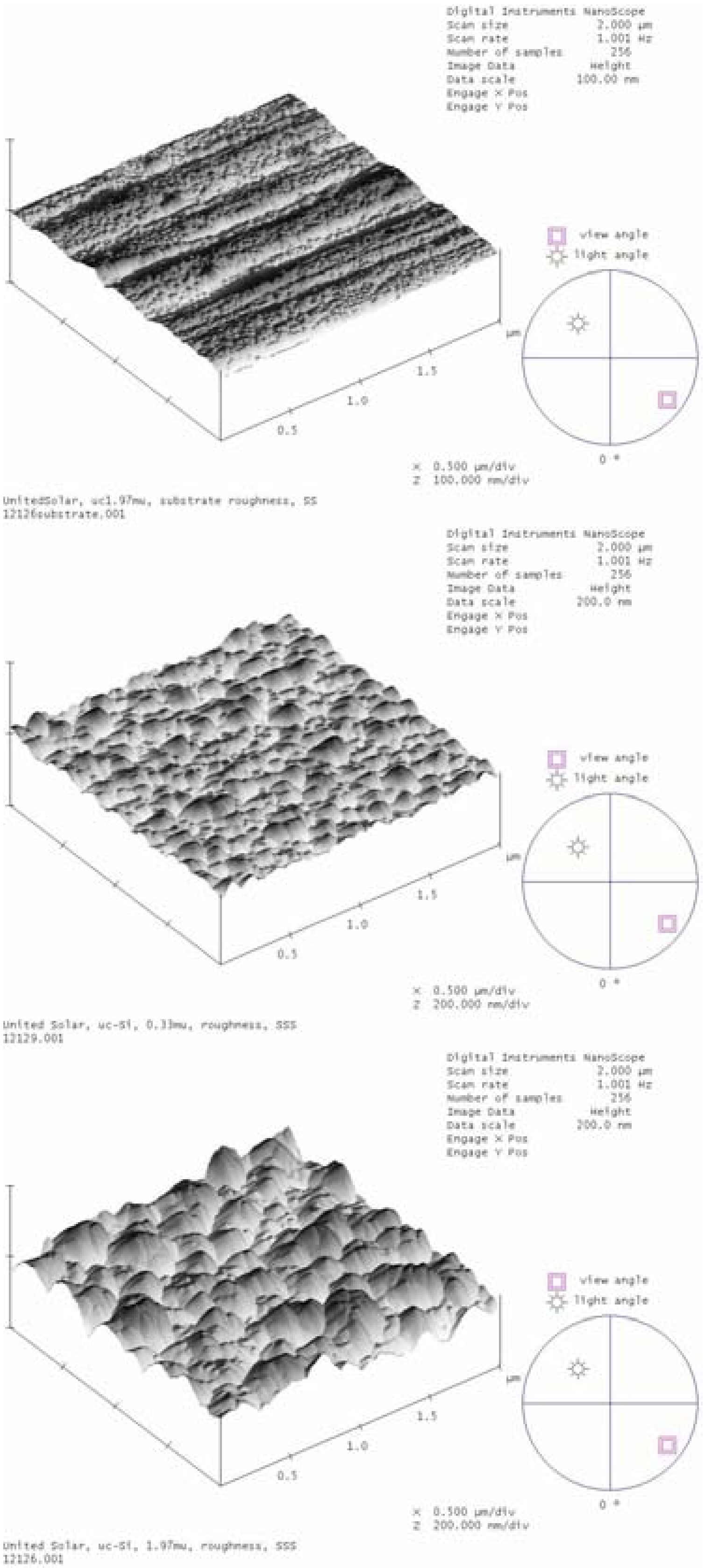

Figure 9. AFM images of (upper) a SS substrate, (middle) a 0.3-µm thick nc-Si:H solar cell and (bottom) a 2-µm thick nc-Si:H solar cell on SS substrate.

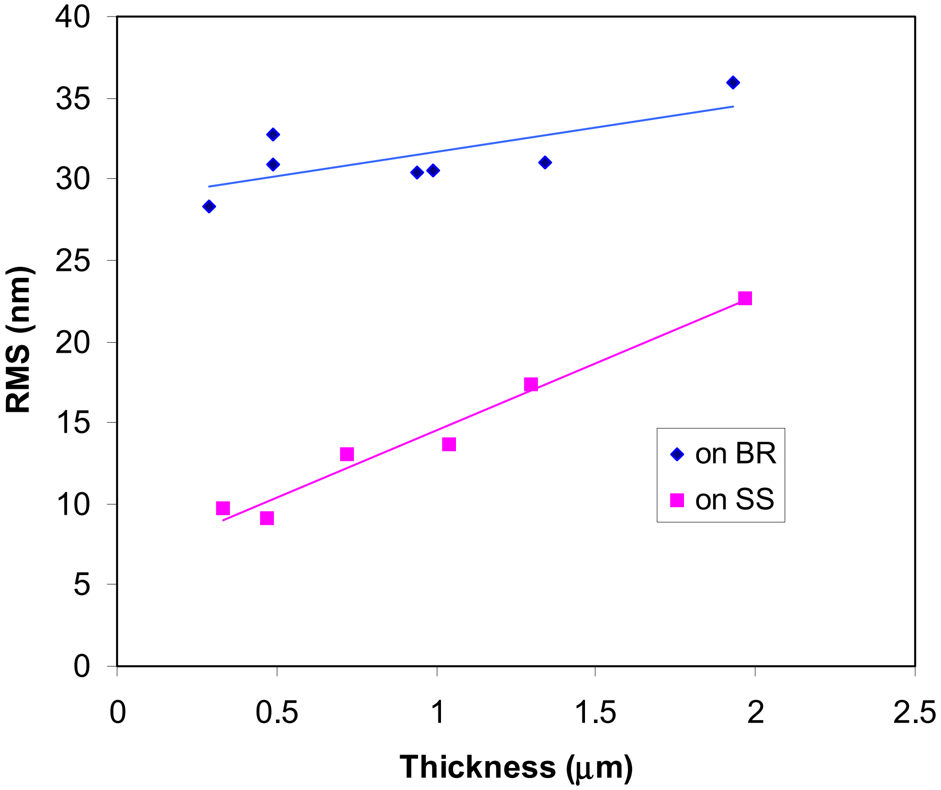

Figure 10. The surface roughness of the nc-Si:H solar cells versus the intrinsic layer thickness.

Si:H with increasing thickness should be responsible for the low J_{sc} problem in thick nc-Si:H solar cells. The material analyses using Raman, XRD and AFM confirm that the crystalline volume fraction and grain size increase with the intrinsic layer thickness significantly.

3.5. Hydrogen dilution profiling in nc-Si:H solar cell deposition

From the results of thickness dependence of the cell performance and structure, we conjecture that the increase in crystalline volume fraction and grain size with intrinsic layer thickness is the main cause for the poor cell performance for thick nc-Si:H solar cells. The exact mechanism for such phenomenon is not clear. As suspected by Finger *et al.* [23], the poor grain boundary passivation could be the main problem for the nc-Si:H materials with a high crystalline volume fraction and large grains. Of course, finding a way to obtain improved grain boundary passivation is a desirable approach for high efficiency nc-Si:H solar cells, especially for a high crystalline volume fraction and large grains. For the short term, we need to develop a way to avoid the increase of crystalline volume fraction and grain size, and hence, reduce the grain boundary defect density. It has been confirmed in many ways that the crystalline volume fraction and grain size grow with the nc-Si:H layer thickness when a constant hydrogen dilution ratio is used. Therefore, we believe that using a proper hydrogen dilution profile with a decreasing hydrogen dilution ratio during the deposition to control the crystalline size and volume fraction could have some effects on the improvement of thick nc-Si:H cell performance.

The hydrogen dilution profiling technique has been used in the deposition of nc-Si:H solar cells using RF at a low rate ~ 1 Å/s and MVHF and a high rate of 3-10 Å/s. Here we present the results of the nc-Si:H solar cells deposited using the Line System with RF excitation at a low deposition rate of ~ 1 Å/s. Textured Ag/ZnO BR was used as a substrate to enhance the light trapping effect. Table IX gives a summary of the J-V characteristics of nc-Si:H single-junction solar cells made with various hydrogen dilution profiles during the intrinsic layer deposition. The first five cells were made using the same recipe to check the reproducibility. It shows clearly that the fill factor (FF) has a large variation from run to run. A major factor that affects the reproducibility is the series resistance of the ITO. The ITO process was optimized for a-Si:H based solar cells, which have a larger V_{oc}, but a lower J_{sc} than nc-Si:H solar cells. From the table, one can easily see that the cells with a higher FF have a lower series resistance. The series resistances listed in the table were deduced from the inverse of the derivative of the light J-V characteristics under the open circuit condition, which includes the contribution from the ITO resistance, junctions, and the intrinsic layer. At this moment, we are not sure whether the main portion of the series resistance is from the ITO or from the intrinsic layer. Although the baseline data are somewhat scattered, the average efficiency is around 6.6%, which is the maximum average value made in a thickness series for cells with the given dilution ratio. Increasing the intrinsic layer deposition time by 20% did not increase the value of $J_{sc.}$ Instead, the response in the middle and long wavelength region was reduced. This phenomenon has been observed many times before. As shown in the previous subsections, the increase of crystalline volume fraction and grain size with thickness is the main origin of the reduction of response in the middle and long wavelength regions. Proper hydrogen dilution profiling can control the crystalline growth evolution. We used this technique of reducing the hydrogen dilution ratio during the intrinsic layer deposition to control the nanostructure evolution. From Line Sample 14578 to 14660, we gradually increase the slope of the hydrogen dilution versus time. As a result, the cell

Table IX: Summary of J-V characteristics of nc-Si:H single-junction solar cells made with various hydrogen dilution profiles. From Profile 1 to Profile 6, the slope of hydrogen dilution ratio versus time was increased.

Sample #	Eff (%)	J_{sc} (mA/cm^2)	V_{oc} (V)	FF			R_s (Ω.cm^2)	Comments
				AM1.5	Blue	Red		
14554	6.74	22.58	0.495	0.603	0.652	0.615	4.4	Baseline
14568	6.48	22.15	0.488	0.599	0.648	0.599	4.0	
14592	6.78	21.32	0.488	0.642	0.690	0.658	3.1	
14594	6.61	20.79	0.486	0.654	0.687	0.648	3.1	
14596	6.61	22.05	0.482	0.622	0.656	0.605	4.0	
14559	6.54	21.48	0.482	0.632	0.678	0.637	4.0	20% thicker than baseline
14562	6.81	21.57	0.484	0.652	0.692	0.651	3.4	
14578	6.63	23.22	0.482	0.594	0.646	0.631	4.3	Profile 1
14580	7.04	22.58	0.484	0.644	0.688	0.662	3.2	Profile 2
14612	7.29	24.41	0.485	0.616	0.659	0.647	3.6	Profile 3
14619	7.81	24.63	0.492	0.645	0.683	0.641	3.4	Profile 4
14642	8.01	23.42	0.502	0.681	0.706	0.700	2.7	Profile 5
14660	8.37	25.15	0.502	0.663	0.679	0.693	3.1	Profile 6

performance has improved significantly. The J_{sc} has improved from approximately 22 mA/cm^2 in the baseline cells to over 25 mA/cm^2 in the best cell (Sample 14660). The previous record for a nc-Si:H single-junction cell without hydrogen dilution profiling was an initial active-area efficiency of 7.4%. Using the hydrogen profiling technique, we achieved a new record of 8.4%. From Fig. 11, one can see that the middle and long wavelength responses have been significantly improved in the cell with proper hydrogen dilution profiling. Figure 12 plots the (a) J-V characteristics and (b) QE curve of the best nc-Si:H single-junction solar cell.

In order to confirm that the hydrogen dilution indeed controls the nanocrystalline evolution, we characterized the nc-Si:H films made with constant hydrogen dilution and with hydrogen dilution profiling using Raman and drive-level-capacitance profiling (DLCP) measurements. Three nc-Si:H films were deposited using RF glow discharge on 10-µm thick Al foil substrates. Sample L14678 was deposited with a constant hydrogen dilution that produces the best solar cell under the given condition. The hydrogen dilution ratio in Sample L14679 was 20% higher than L14678. Sample L14680 was deposited with a hydrogen dilution profiling, in which the hydrogen dilution was continually decreased during the film growth, but with an average dilution ratio equal to that in Sample L14678. The thicknesses are 0.96, 0.84, and 1.04 µm for L14678, L14679, and L14680, respectively. In addition, two a-Si:H/nc-Si:H/a-Si:H sandwich structures were deposited on specular stainless steel substrates for the DLCP measurements, where the 0.25-µm thick a-Si:H layers serve as caps for the 0.75-µm thick nc-Si:H layer.

The Raman measurements were made using three different lasers with wavelengths of 610 nm (red), 514.5 nm (green), and 480 nm (blue). Due to the different penetration depth, the red light probes the bulk of the films, while the green and blue lights only measure the top surface layer of the films. Figure 13 shows the Raman spectra for the three samples measured with the three wavelengths. One can see that for the two samples with constant hydrogen dilution, the amorphous component in the bulk (red) is greater than those in the surface layers (green and blue). This result implies that the crystallinity increases as the film grows thicker, which is consistent with the results in the previous subsection. In contrast, for the profiled sample (L14680), the amorphous component in the bulk (red) is actually smaller than that near the surface layer. In other words, the crystallinity decreases with the increase in thickness. In order to obtain more detailed structural information, the spectra were de-convoluted into three components: i) a sharp Lorentzian peak at ~520 cm^{-1} for the crystalline component, ii) an intermediate Gaussian peak at ~490-510 cm^{-1} for the grain boundary component, and iii) a broad Gaussian peak at ~480 cm^{-1} for the amorphous component. We then determined f_c and f_{gb} using the formulas given previously. Table X lists the calculated values of f_c and f_{gb}. It clearly shows that the average f_c increases from the bulk to the top surface for the two samples made with constant hydrogen dilution ratios, but that f_{gb} does not increase from the bulk to the top surface. Instead, it slightly decreases. Comparing L14679 to L14678, we find that a 20% increase in hydrogen dilution increases f_c by 12.5% (red) in the bulk, and 17% near the top surface (blue). However, f_{gb} does not increase, but slightly decreases. The most important result is that the sample made with hydrogen dilution profiling does not show any increase in f_c. In fact, f_c decreases from 75% in the bulk to 62-66% in the top surface layer.

Figure 14 compares DLCP measurements of samples made with a constant hydrogen dilution (L14140) and profiled hydrogen dilution (L14661). The profiles of defect density for the two samples appear significantly different. Specifically, for the sample with constant hydrogen dilution, the DLCP density increases in the direction of the film growth, exceeding 10^{16} cm^{-3} as we approach the Schottky interface at the top surface of the film. This variation is present in all the samples deposited under constant hydrogen dilution and is again believed to result from the increase in crystalline volume fraction and crystallite size as the film growth progresses. In contrast, when hydrogen profiling is employed to control the nanocrystalline evolution, the sample exhibits a DLCP profile that reaches a maximum value below 10^{16} cm^{-3} near the middle of the film, before decreasing again toward the top surface.

In summary, the Raman measurements provide evidence that hydrogen dilution profiling indeed controls the nanocrystalline structural evolution along the growth direction. The DLCP measurements show that the defect density increases with the film thickness for the samples made with constant hydrogen dilution, which could be related to the structural evolution. The hydrogen dilution profiling effectively controls the increase in the defect density along the growth direction. These measurements provide insight into how hydrogen dilution profiling modifies the structure of these nc-Si:H materials, which in turn improves the nc-Si:H solar cell performance.

Table X: The f_c and f_{gb} values as well as c-Si peak energy positions of the spectra in Fig. 13.

Film No.	f_c (%)			f_{gb} (%)			c-Si peak (cm^{-1})		
	red	green	blue	red	green	blue	red	green	blue
L14678	72	78	76	23	23	21	514	520	517
L14679	81	85	89	25	20	16	517	519	518
L14680	75	62	66	28	24	14	518	518	518

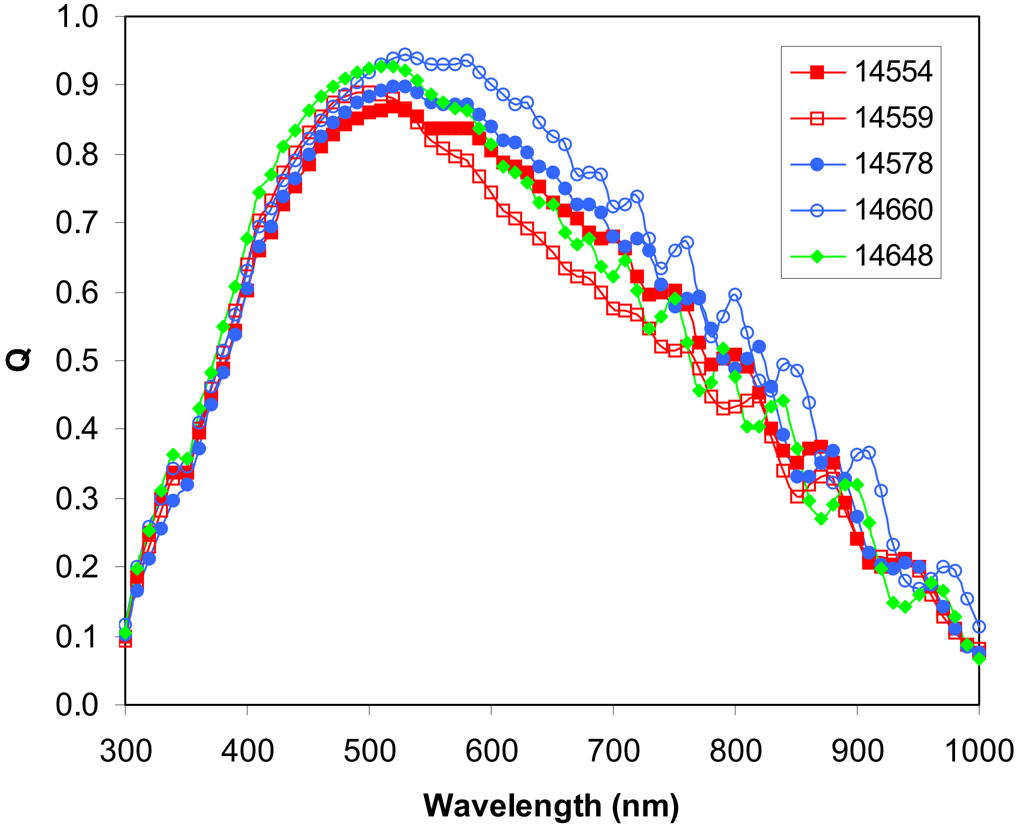

1.0
0.9
0.8
0.7
0.6
0.5
0.4
0.3
0.2
0.1
0.0
Q
300
400
500
600
700
800
900
1000
Wavelength (nm)
14554
14559
14578
14660
14648

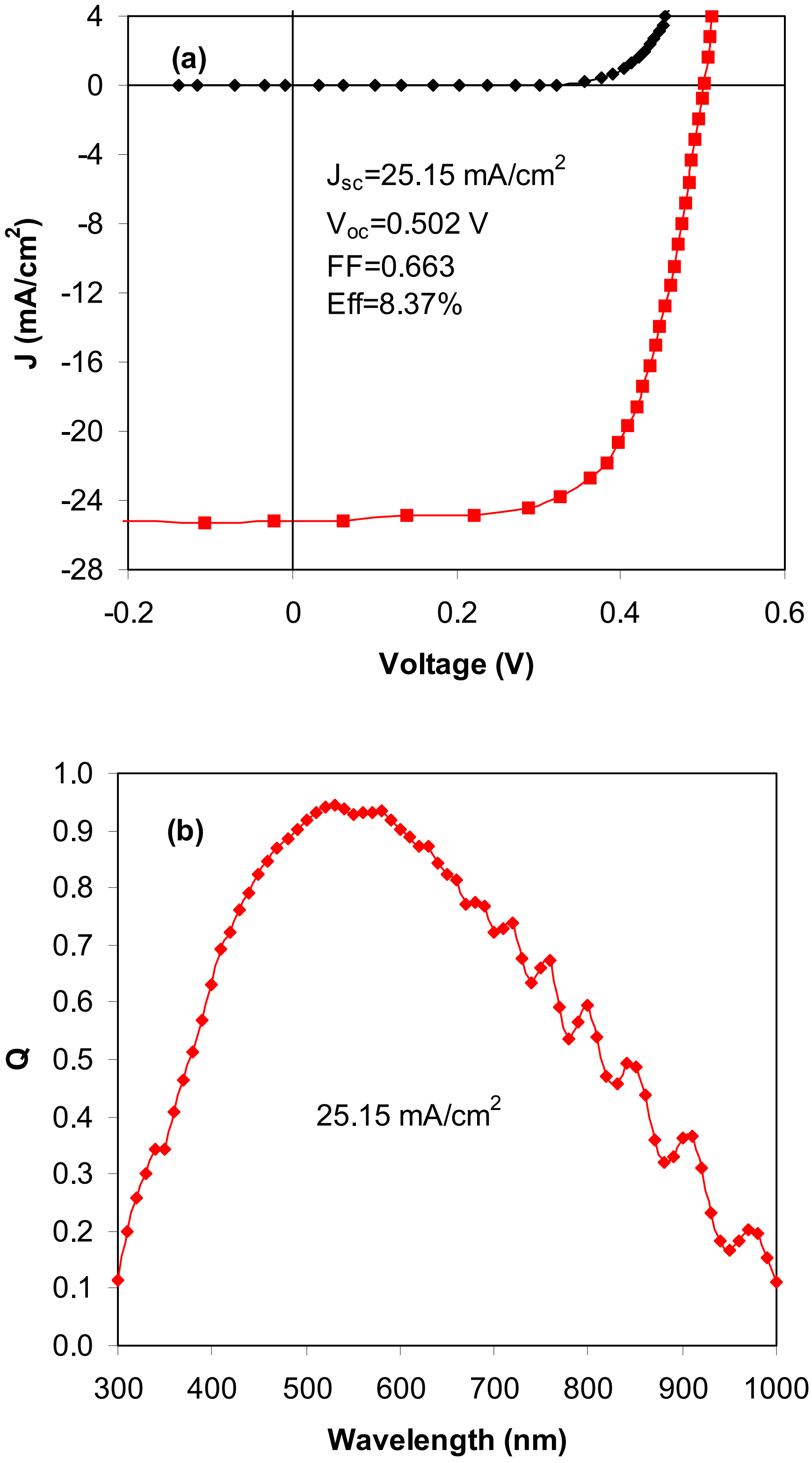

Figure 12. (a) J-V characteristics and (b) quantum efficiency of a nc-Si:H single-junction solar cell with an initial active-area efficiency of 8.37%.

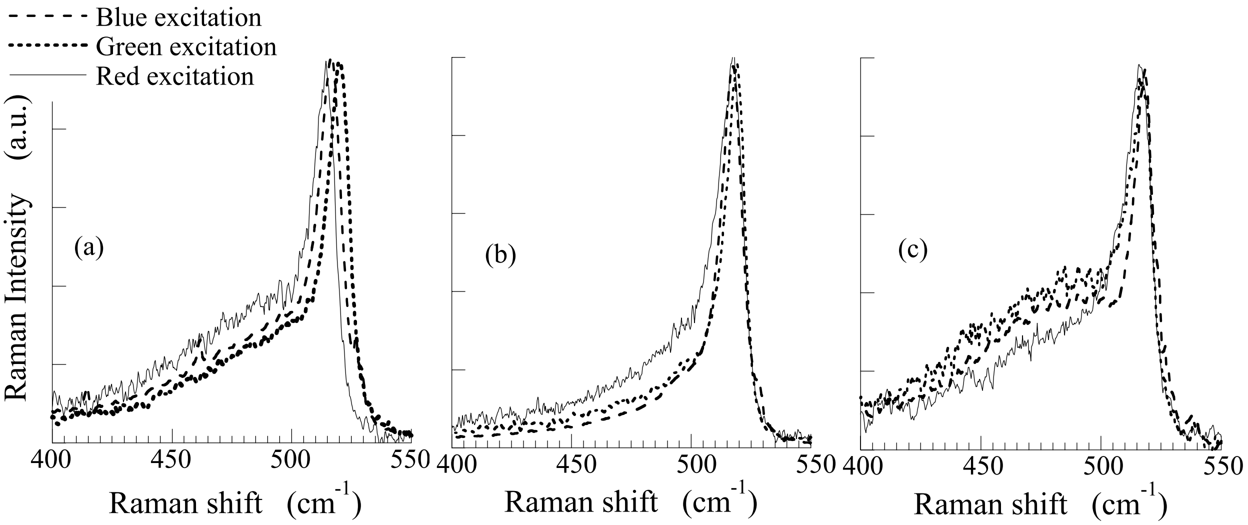

Figure 13. Raman spectra films of (a) L14678, (b) L14679, and (c) L14680 excited by the blue, green, and red lasers, respectively.

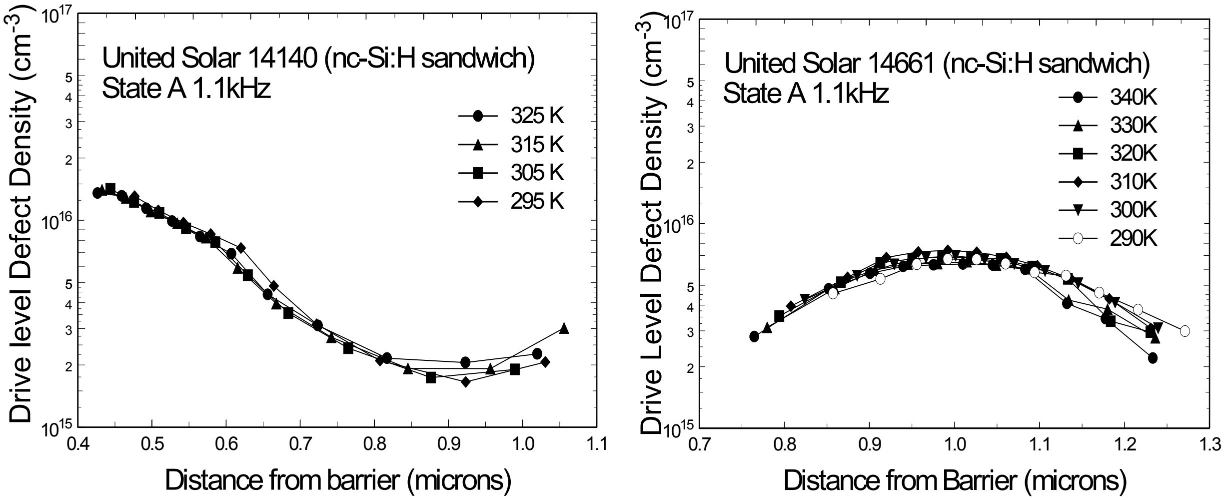

Figure 14. Comparison of DLCP spectra of a nc-Si:H device grown using a constant hydrogen dilution (left) with one grown with hydrogen profiling (right).

3.6. Control of interfaces

High material quality in all the layers of the device is essential, but does not ensure high solar cell efficiency. Previous studies of a-Si:H and a-SiGe:H solar cells showed that an optimized interface between the intrinsic layer and doped layers is also important. Similarly, for nc-Si:H *n-i-p* solar cells, we need to optimize the material quality for each layer as well as control the interface. Figure 15 shows the light J-V characteristics of solar cells with different interface layers: (a) optimized *n/i* and *i/p* buffer layers, (b) *n/i* buffer layer only, (c) *i/p* buffer layer only, and (d) no *n/i* and *i/p* buffer layers. The four solar cells were made on a Ag/ZnO back reflector with the same recipe except for different buffer layers at the *n/i* and *i/p* interfaces. The nc-Si:H layer was deposited using a RF glow discharge at ~1 Å/s with a thickness ~0.9 μm. Comparing the results of Figs. 15 (a) and (b), we find that without the *i/p* buffer layer, the V_{oc} and FF are lower. The lower V_{oc} may be attributed to the higher shunt current as shown in Fig. 16, where the cell with no *i/p* buffer layer has a significantly higher shunt current at lower bias than the cell with *i/p* buffer layer. The mechanism for the high shunt current is not clear. We believe that leakage through the grain boundaries is probably the source of shunt current in nc-Si:H solar cells. Comparing the results of Figs. 15 (a) and (c), we find that V_{oc} is slightly higher, but J_{sc} and FF are lower for the cell with no *n/i* buffer layer than with the *n/i* buffer layer. The higher V_{oc} and lower J_{sc} indicate a lower average crystalline volume fraction in the intrinsic layer for the sample with no *n/i* buffer layer than with the *n/i* buffer layer. The poorer FF with no *n/i* buffer layer may be due to a poorer carrier transport. Normally, there is a crossover between the dark and light J-V curves as shown in Figs. 15 (c) and (d); a phenomenon that often appears in mixed-phase solar cells. The crossover is due to a low forward current in the dark as shown in Fig. 16, where the dark J-V levels off from the exponential line at the high voltage for the samples with no *n/i* buffers. The cell with no buffer layer has the lowest efficiency with a large crossover between dark and light J-V characteristics, and the dark J-V shows a high shunt current at low bias and levels off at high bias. From this study we conclude that as in the case of a-Si:H and a-SiGe:H alloy solar cells, the interfaces between the intrinsic nc-Si:H layer and the doped layers are also very important. We continue to work on the optimization of the interface layers.

3.7. Dark J-V measurements for nc-Si:H solar cells

The carrier transport properties are important for cell performance. Many techniques have been used to measure the carrier transport properties such as carrier mobility and lifetime in nc-Si:H materials. However, most of the techniques require special sample structure or special substrate. In addition, it has been shown that nc-Si:H material properties depend on cell thickness and substrate, which leads to a question whether or not the obtained transport parameters represent the real situation in solar cells. It has been widely accepted that the most reliable material properties should be directly obtained from the device. For this purpose, we carried out dark J-V measurements on actual nc-Si:H solar cells.

Figure 17 shows a series of dark J-V characteristics measured at different temperatures for nc-Si:H solar cells deposited on Ag/ZnO back-reflector (BR) coated stainless steel substrates and on stainless steel with no back reflectors. The interfaces were tailored to reduce the

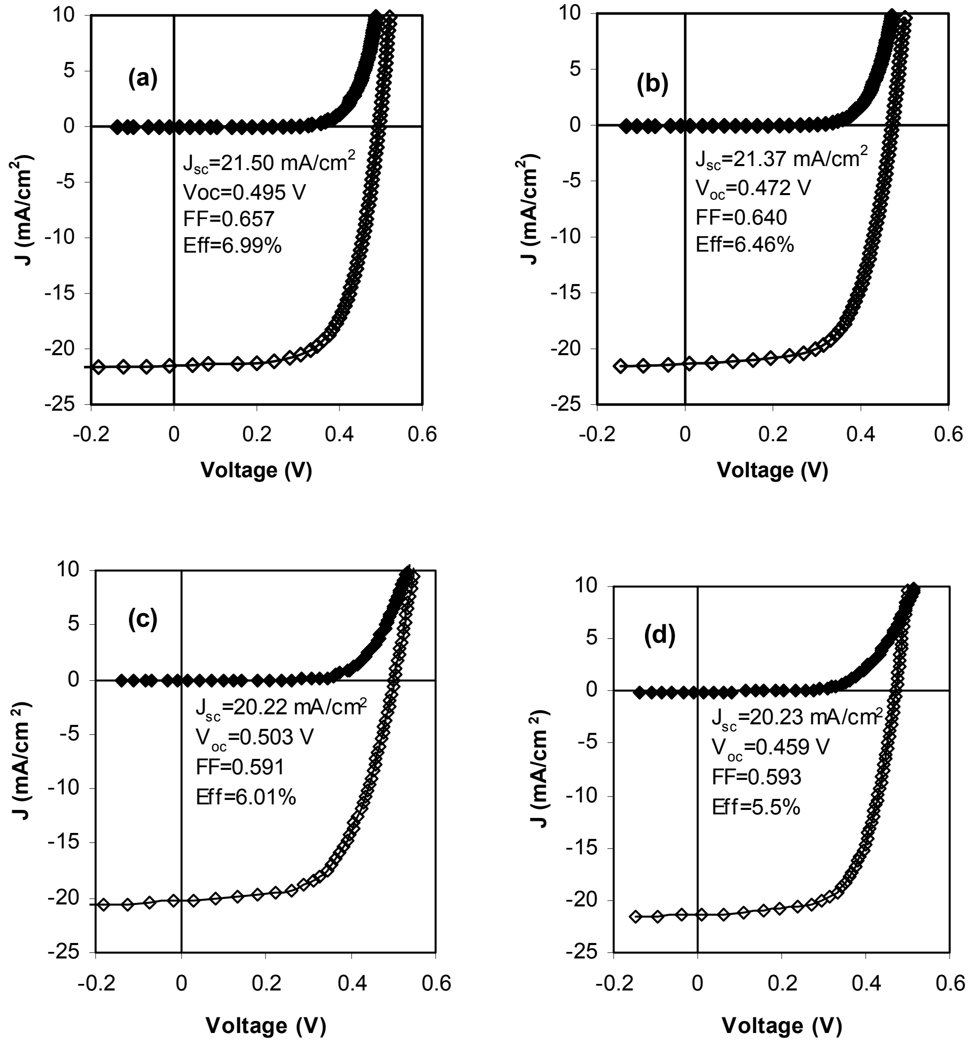

Figure 15. J-V characteristics of nc-Si:H single-junction solar cells deposited using RF glow discharge with different interface layers: (a) with both *n/i* and *i/p* buffer layer, (b) with *n/i* buffer layer only, (c) with *i/p* buffer only, and (d) with no *n/i* and *i/p* buffer layers.

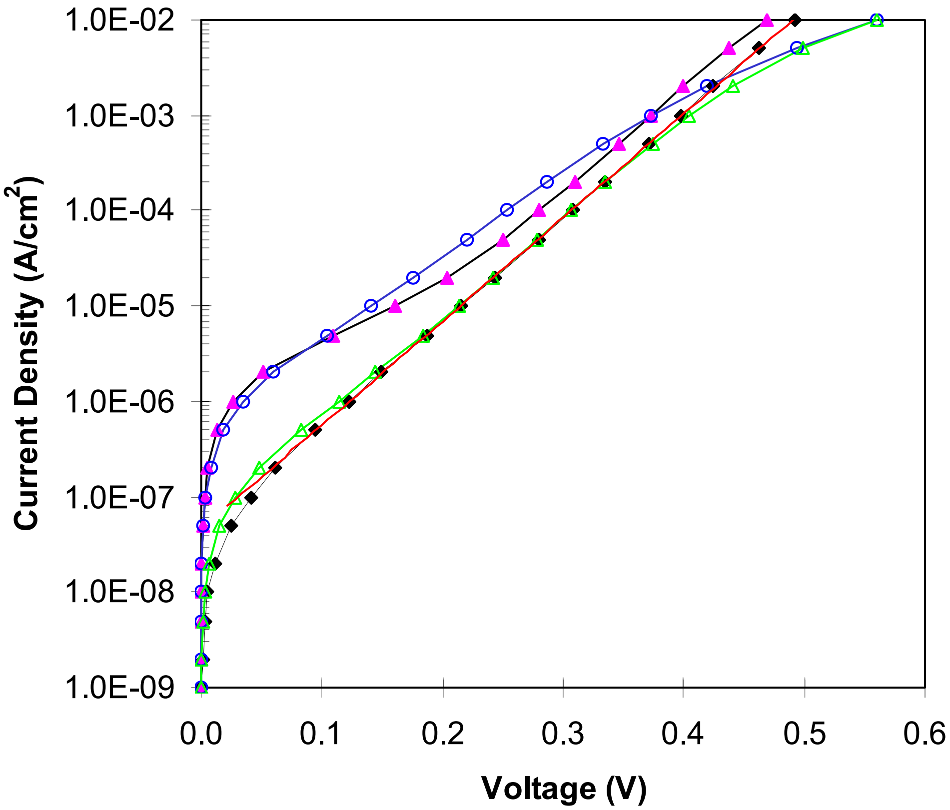

Figure 16. Dark J-V characteristics of nc-Si:H solar cells made with (◆) both *n/i* layer and *i/p* buffer layers, (▲) only *n/i* buffer layer, (△) only *i/p* buffer layer, and (○) no *i/n* and *i/p* buffer layers.

incubation layer and reduce shunt current. The dark J-V curves show perfect diode characteristics over a wide range of temperature as described by the equation:

$$J(V) = J_0 \left\{ \exp\left(\frac{qV}{nkT} \right) - 1 \right\} \qquad (1)$$

where J_0 is the reverse saturation current density, n the diode quality factor, -q the charge of an electron, k the Boltzmann constant, and T the measurement temperature.

Figure 18 (a) plots J_0 versus 1000/T for two cells deposited using the same recipe but one on SS and the other on Ag/ZnO back reflector coated SS. Both cells show a linear relationship on the semi-log plot and give the same activation energy of 0.65 eV. If the Fermi-level is at the center of the bandgap, twice the value of the activation energy is equal to the electronic bandgap. Since most nc-Si:H materials show weak *n*-type transport, we can conclude that the electronic bandgap in the nc-Si:H intrinsic layer is >1.3 eV. Referring to Fig. 18 (a), the curve for the BR cell is shifted by a factor of 3 higher than the SS cell. The shift may be partially attributed to the larger effective area of the BR cell due to the texture of the back reflector. Figure 18 (b) plots n versus T for the same two samples. The decrease of n with the increase of temperature indicates an increased diffusion length (or mobility) at high temperature; the larger n for the cell on Ag/ZnO back reflector is probably due to a higher recombination rate and a larger effective path for carrier transport across the intrinsic layer due to the texture of Ag/ZnO back reflector.

3.8. Summary

During the past three years, we have investigated many issues related to the nc-Si:H material properties and device design, fabrication, and characterization. One problem for nc-Si:H in solar cells is the nanocrystalline evolution with thickness. The increase of crystalline volume fraction and grain size degrades nc-Si:H solar cell performance and limits the intrinsic layer thickness. We have developed a hydrogen dilution profiling technique to control the nanocrystalline evolution and successfully improved the nc-Si:H cell performance. Significant collaborations with many team members have been carried out for characterizing the nc-Si:H properties and identifying the problems in the materials and devices. We have worked on the device design including the interface layers for nc-Si:H solar cells. We have developed proper buffer layers at the *n/i* and *i/p* interfaces to improve the nc-Si:H cell performance. We used dark J-V characteristics to obtain the nc-Si:H material properties and to detect any problems in the devices. Overall, the fundamental studies have built the solid foundation for high efficiency multi-junction solar cells using nc-Si:H as the bottom cell.

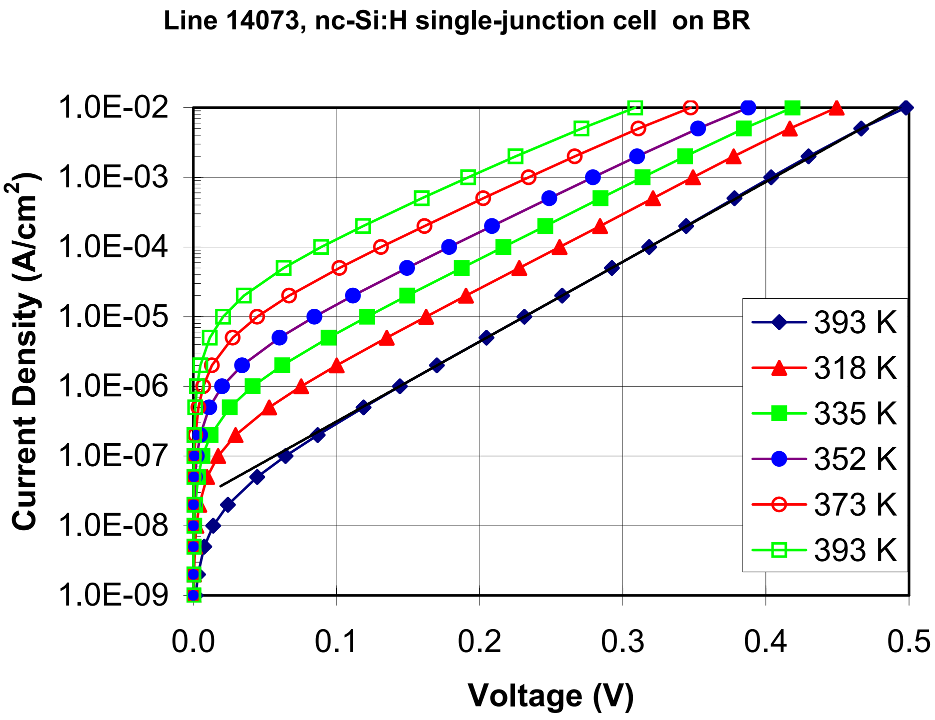
Line 14073, nc-Si:H single-junction cell on BR

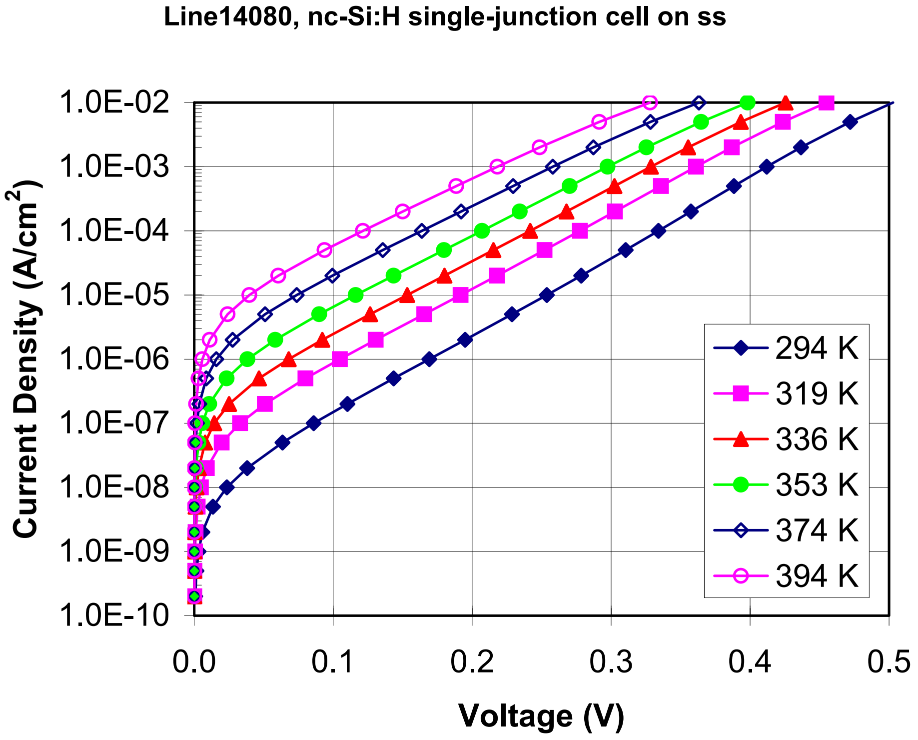
Line14080, nc-Si:H single-junction cell on ss

Figure 17. Dark J-V characteristics measured at different temperatures for nc-Si:H solar cells deposited on Ag/ZnO back reflector and on stainless steel (SS).

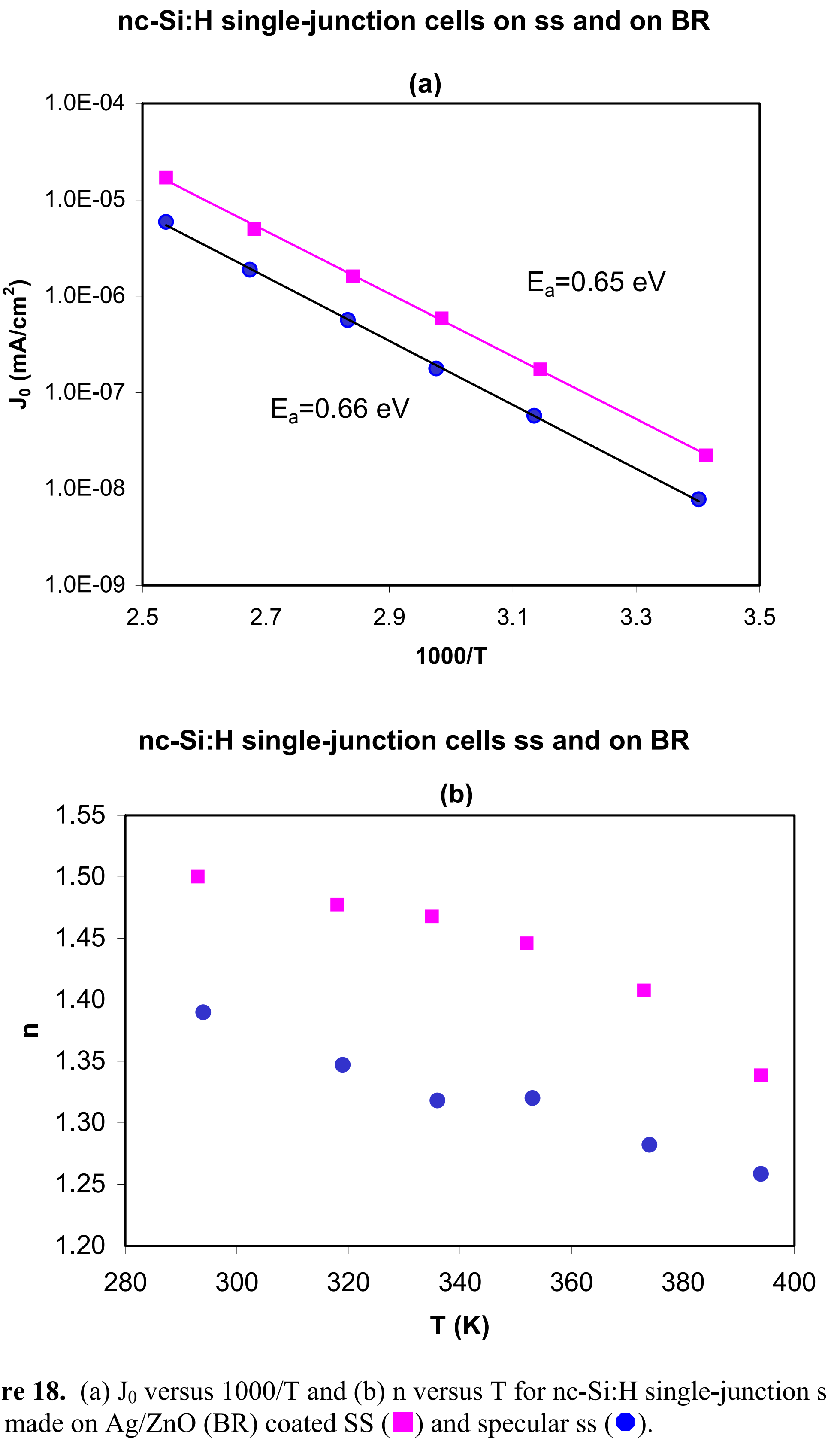

Figure 18. (a) J_0 versus 1000/T and (b) n versus T for nc-Si:H single-junction solar cells made on Ag/ZnO (BR) coated SS (■) and specular ss (●).

Section 4: Optimization of Ag/ZnO Back Reflector

4.1. Introduction

As discussed above, a-Si:H and a-SiGe:H based solar cell technology is one of the most attractive photovoltaic technologies, due to its low cost and large-scale manufacturing abilities. Among the techniques for improving cell performance, light trapping with textured BR is an important one for enhancing J_{sc} [28]. A textured Ag/ZnO BR was used for achieving 14.6% initial and 13.0% stable efficiencies in an a-Si:H/a-SiGe:H/a-SiGe:H triple-junction structure [1]. Recently, nc-Si:H solar cells have attracted remarkable attention due to their superior long wavelength response and improved stability over a-SiGe:H [12, 13]. Using our conventional Ag/ZnO BR, we have achieved high efficiencies with a-Si:H/nc-Si:H double-junction and a-Si:H/a-SiGe:H/nc-Si:H triple-junction structures [6, 29]. However, because of the nature of the nc-Si:H structure, the optimized Ag/ZnO BR used for a-Si:H and a-SiGe:H solar cells may not necessarily be the best choice for the nc-Si:H solar cells. Optimizing the Ag/ZnO BR has the potential of improving the nc-Si:H cell efficiency further; hence, achieving even higher efficiencies in the multi-junction cells with a nc-Si:H bottom cell. In addition, an improved BR may result in an even higher efficiency for a-Si:H/a-SiGe:H/a-SiGe:H triple-junction cells. In this program, we have worked on the optimization of the Ag/ZnO BR by searching the deposition parameter space and etching the deposited BR using diluted HCl to modify the surface morphology. The optimized BRs have shown an improvement in a-SiGe:H and nc-Si:H solar cell performance. Here, we report the results on the correlation of the BR preparation condition, surface morphology on BRs, and solar cell performance.

4.2. Experimental

We deposited Ag/ZnO BR on specular stainless steel substrates using a sputtering method. The texture of the Ag and ZnO layers was controlled by deposition parameters such as pressure, substrate temperature, and RF power. In addition, we used chemical etching with 0.5% HCl [30] to modify the texture on the BR surface. The surface morphology was investigated by AFM at NREL. To characterize the scattering effect from the textured surface, the scattered light intensity from a He-Ne laser, which illuminates the sample perpendicularly to the sample surface, was measured at different angles. Details of the measurements were given in the last quarterly report. Finally, a-SiGe:H and nc-Si:H solar cells were deposited on BR substrates made under various conditions to correlate the surface properties of the BR to the solar cell performance. The solar cells were deposited using RF glow discharge at low rates in different deposition systems. J-V characteristics were measured under an AM1.5 solar simulator at 25 °C and QE curves were measured from 300 to 1000 nm at room temperature.

4.3. Texture and light scattering of Ag/ZnO back reflector

The texture of the Ag/ZnO BR can be controlled by the sputtering parameters such as substrate temperature, gas flow rate, RF power, and the thickness of the Ag and ZnO layers. A proper chemical etching can also modify the surface morphology. Figure 19 shows four AFM pictures of BRs made under various conditions and chemical treatments, where (a) is a conventional BR (5BR1748) developed previously [28], (b) a BR (R7900) with large micro-

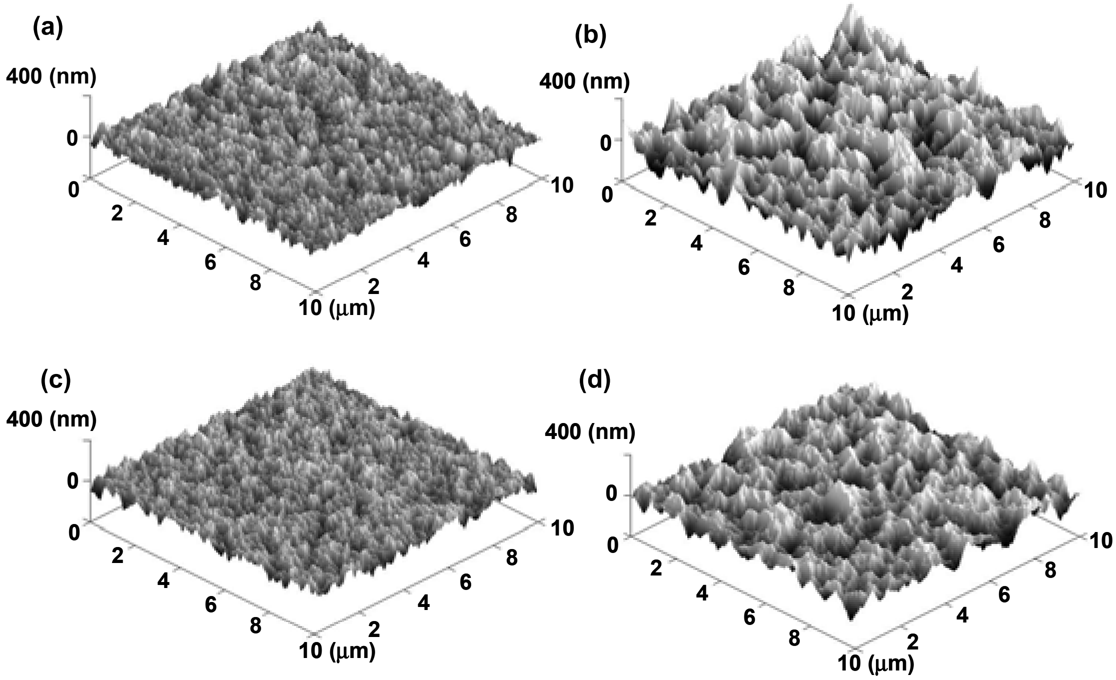

Figure 19. AFM pictures of four Ag/ZnO BRs made with various deposition parameters and chemical etchings. Details of the sample preparation are given in the text.

features created by adjusting the deposition parameter, (c) is a BR (R7948) with a thicker ZnO before chemical etching, and (d) the same BR as in (c), but after 30-second chemical etching in 0.5% HCl. The micro-feature size on the conventional BR is on the order of 0.1-0.2 μm with a root mean square (RMS) roughness of 38.2 nm. By adjusting the deposition parameters, we can increase the feature size to as large as 0.5-1.0 μm with RMS of 80.5 nm (Fig. 19 (b)). In addition, the chemical etching modifies the micro-features on the BR surface. It seems that the small features are etched away and the feature size increases. Correspondingly, the RMS increases from 39.6 nm to 63.2 nm after a 30-second etching in 0.5% HCl as shown by comparing Fig. 1 (c) and (d).

Figure 20 (upper) plots the RMS versus the etching time for six BRs with different initial RMS. It clearly shows that RMS increases after etching. On the four samples with lower initial RMS, the RMS increases with the etching time up to 20 seconds. No additional roughness increase was observed for the etching time longer than 20 seconds. For one sample (R7900) with an initial RMS of 80 nm, the RMS increases to 140 nm after 30 seconds of etching. Figure 20 (lower) shows the difference between the total microscopic surface area and the flat surface area. It does not show a unique trend of the area difference. If we assume that the surface micro-features are all pyramids, the angles between the feature surface and base are in the range of 27 and 38°. The upper plot in Fig. 21 shows the measured scattered light intensity, $I(\theta)$, versus the angle, θ, between the scattering beam and the sample surface, where the laser is incident from 90°, and the lower plot shows the total scattered light intensity, $I(\theta)\cos\theta$, at all the positions with the same θ, where $\cos\theta$ takes into account the geometry factor. In the figure, sample R7948 has an initial RMS of 39.2 nm; and the RMS increases to 63.2 nm after 30 seconds of etching, while sample R7900 has an initial RMS of 80.5 nm and 139.2 nm after 30 seconds of etching. Since the angle between the micro-feature surface and the base does not change very much, the increase of RMS is mainly due to the increase of the feature size. Because the light cannot distinguish the features with sizes much smaller than the wavelength of the light, the BRs with small micro-features do not scatter the light effectively. With the increase of the micro-feature size, the scattered light intensity increases. Another interesting phenomenon is the fine structures on the scattered light curves as shown in Fig. 21. We initially thought they were measurement noise, but later on, we found they are real signals and can be reproduced by repeated measurement without changing the position of the sample. Further investigation of possible correlation between the micro-features on the BR surface and scattered light intensity is ongoing.

4.4. a-SiGe:H bottom cells on various BR substrates

The final qualification for BR is to check whether it improves the solar cell performance. We deposited a-SiGe:H alloy solar cells on the different BRs described above. The deposition conditions were given previously. Table XI lists the BR properties and the corresponding a-SiGe:H solar cell performance, where the solar cells were made with a bottom cell recipe for a-Si:H/a-SiGe:H/a-SiGe:H triple-junction solar cells. The J-V characteristics were measured under an AM1.5 solar simulator with a 630-nm cut-on filter, and the J_{sc} was obtained from QE measurements. We find that the overall solar cell performance is improved by increasing the micro-feature size. Although there is a large run-to-run variation, the J_{sc} shows a tendency to

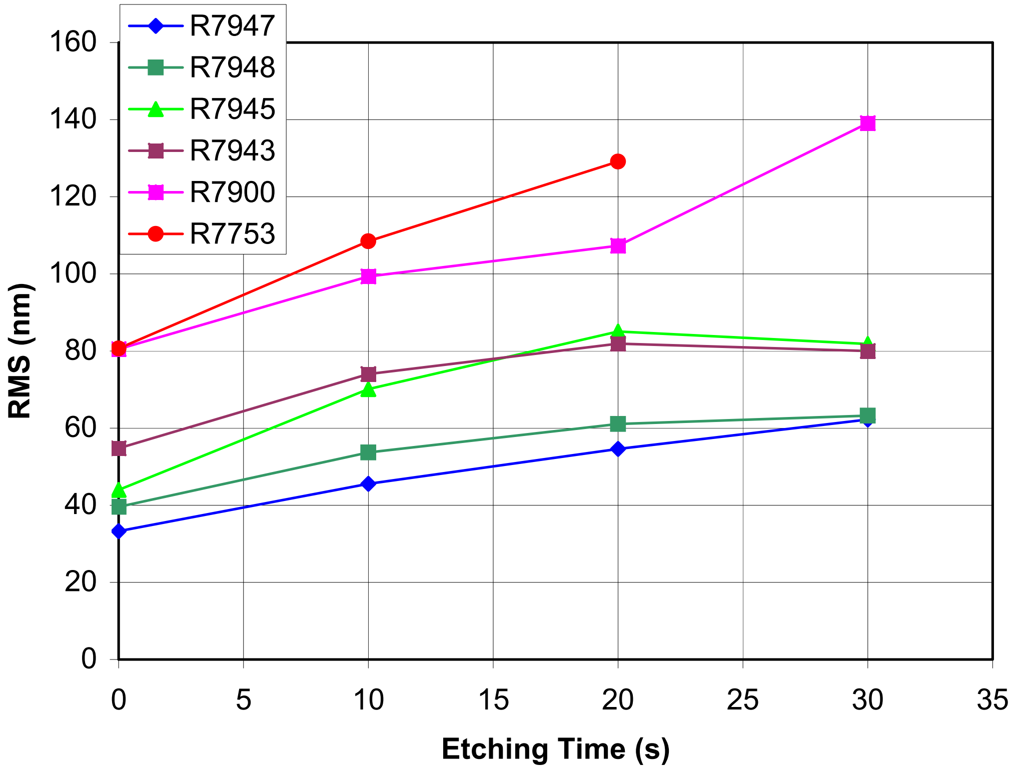

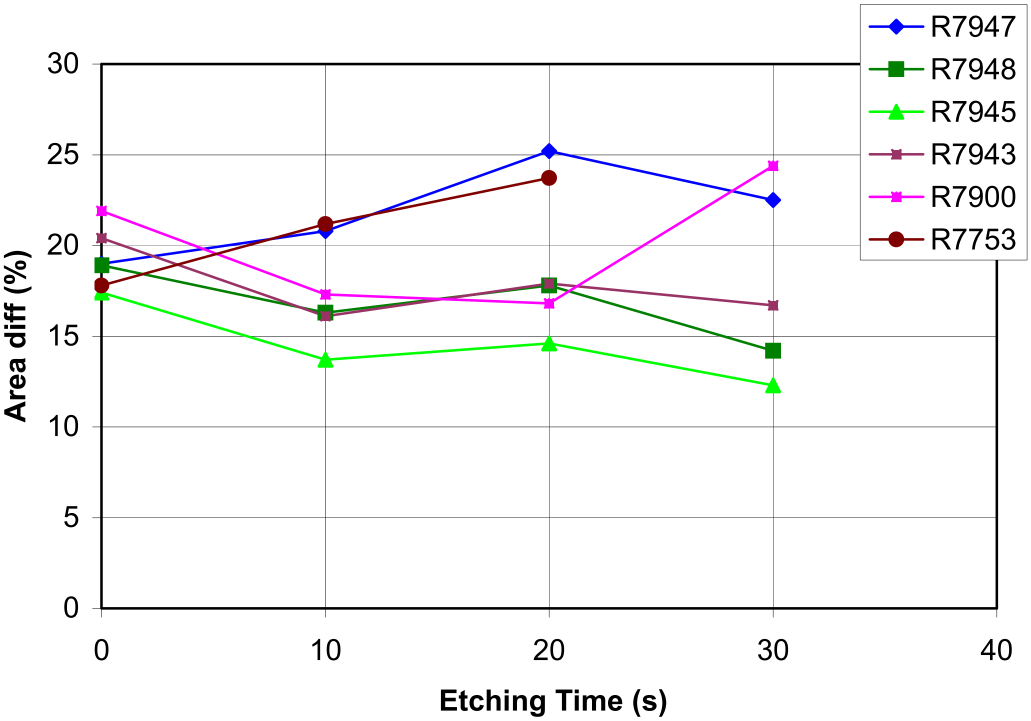

Figure 20. (upper) RMS and (lower) area-difference versus the etching time in 0.5% HCl for Ag/ZnO BRs with different original roughness.

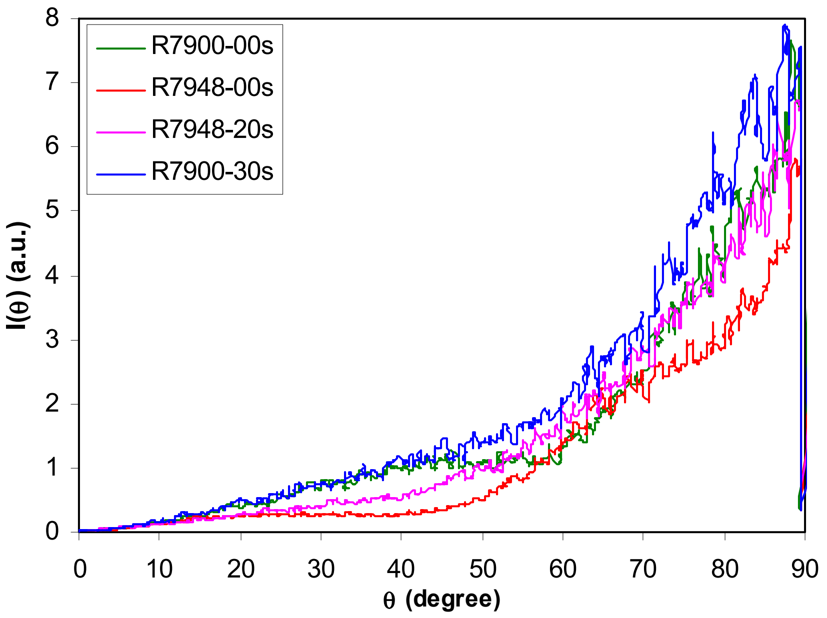

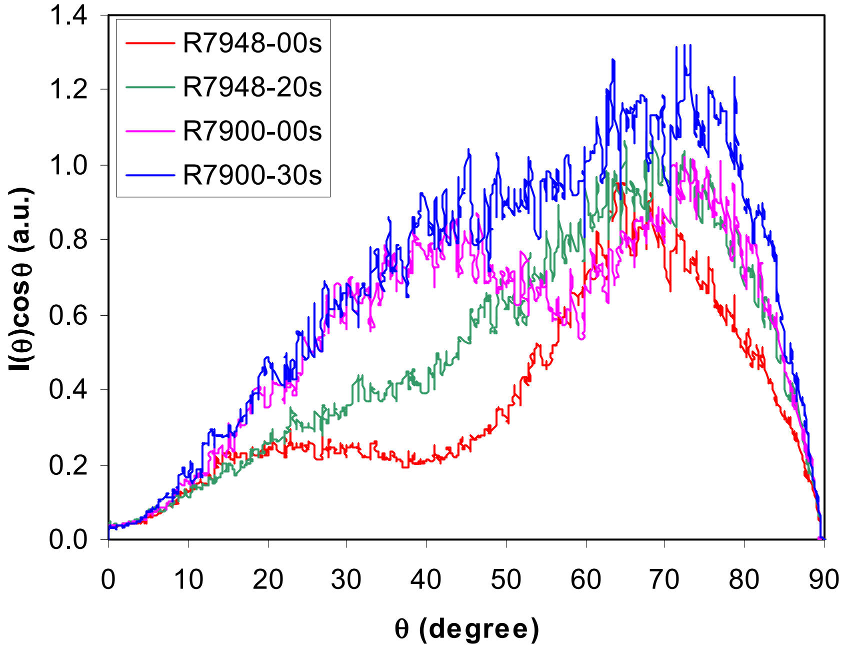

Figure 21. (upper) Scattered light intensity, I(θ),versus the angle, θ, between the detector and the sample surface, (lower) the I(θ)cosθ versus θ.

increase with the RMS as plotted in Fig. 22 (upper). However, the gain in J_{sc} is not as large as expected. Two possible mechanisms could explain the lack of strong correlation between the J_{sc} and the roughness of the substrate. First, for the substrate with micro-feature size smaller than the wavelength of the light, the light cannot distinguish the micro-features, and therefore, the small features do not contribute to the light trapping effectively. For example, for a wavelength of 900 nm, by taking the wavelength compression factor of 3-4 (n_{Si}/n_{air}) into account, the micro-features with sizes smaller than 225-300 nm would not scatter the light effectively. The clear interference fringes on the QE curves for the cells on the BRs with smaller features as shown in Fig. 23 confirms the explanation. Second, for the BR with larger micro-features, the feature sizes could be larger than the cell thickness. Normally, for an a-SiGe:H bottom cell, the total thickness of the semiconductor layers is thinner than the long wavelength of the solar spectrum. If the semiconductor layers grow conformally with the substrate morphology, even though the micro-features can effectively scatter the light (as confirmed by less interference on the QE curves in Fig. 23), the light hardly reaches the total reflection condition in the semiconductor layers. Therefore, the effect of texture on J_{sc} is not very large.

It is interesting to note that the V_{oc} increases for the cells deposited on the BR with a high RMS as shown by Fig. 22 (lower). This result was unexpected, but was confirmed by repeated experiments. One explanation could be that for the cells deposited on the BRs with smaller micro-features, the high density of sharp peaks on the substrate causes significant back diffusion of photo-generated carriers at the *p/i* and *i/n* interfaces. Sharp peaks can also cause an increase in the shunt current density. Increasing the micro-feature size is equivalent to decreasing the peak density, hence, reducing the loss of V_{oc}.

Table XI: BR properties and a-SiGe:H alloy solar cell performance. The J-V characteristics were measured under an AM1.5 solar simulator with a 630-nm long pass filter; J_{sc} was obtained from QE .

Sample #	BR #	Etching (sec)	RMS (nm)	P_{max} (mW/cm^2)	J_{sc} (mA/cm^2)	V_{oc} (V)	FF
B8564	5BR1748	0	38.2	4.07	10.16	0.641	0.625
R8539	R7749	0	65.3	4.57	11.03	0.650	0.638
R8534	R7900	0	80.5	4.38	10.06	0.654	0.665
R8538	R7753	0	80.7	4.47	11.10	0.651	0.612
R8549	R7753	10	108.5	4.58	10.83	0.655	0.646
B8563	R7948	0	39.6	3.65	9.71	0.627	0.608
B8556	R7948	20	61.1	4.34	10.75	0.637	0.633
B8554	R7948	30	63.2	4.01	10.49	0.623	0.614
B8535	R7943	0	54.8	4.20	10.49	0.635	0.631
B8553	R7943	10	74.0	4.56	10.99	0.651	0.638
B8552	R7943	30	80.0	4.25	10.21	0.651	0.640

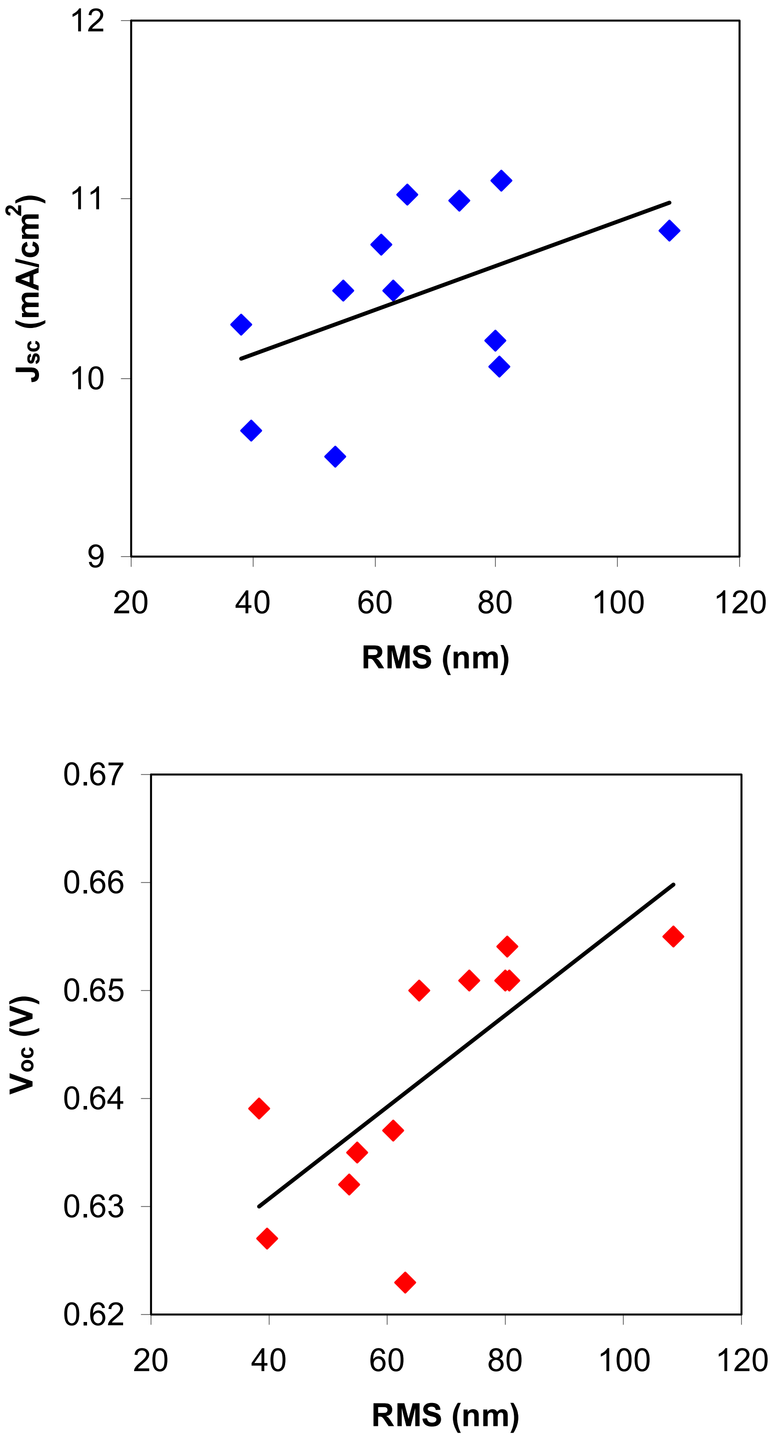

Figure 22. J_{sc} (upper) and V_{oc} (lower) versus the RMS of the Ag/ZnO BR substrates. The measurements were made under an AM1.5 solar simulator with a 630-nm cut-on filter.

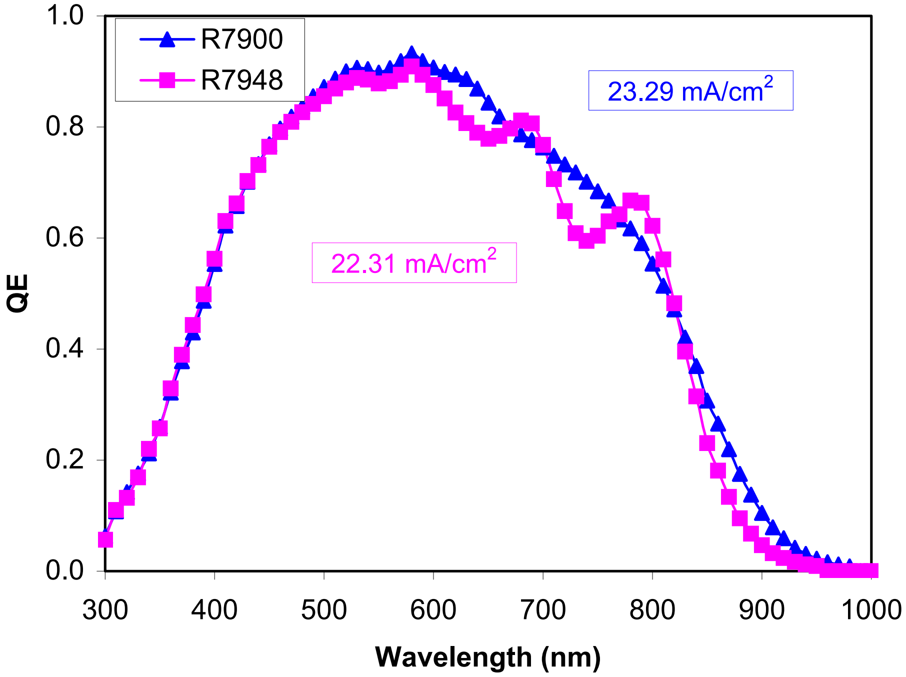

Figure 23. QE curves for a-SiGe:H bottom solar cells on R7900 and R7948 without etching.

4.5. nc-Si:H solar cells on various BR substrates

We also deposited nc-Si:H cells on different BRs. Table XII summarizes J-V characteristics along with the properties of the substrates, where the four solar cells were deposited under the same conditions. It clearly shows that the J_{sc} increases with the increase of the micro-feature size on the BR. Figure 24 plots the QE curves of the four nc-Si:H solar cells. Similar to the a-SiGe:H solar cells, the increase of micro-feature size eliminates the interference fringes from the QE curves, indicating a diffusive scattering in the device. The difference as compared to the a-SiGe:H cells is a clear gain in the J_{sc} obtained by increasing the roughness on the BR surface. The interpretation for the difference in the two cases could be as follows: the intrinsic layer in the nc-Si:H cells is over 1 μm thick, which is a few times larger than the relevant wavelength of the light in the spectrum (taking the wavelength compression factor into account). Certain light, scattered at small angles θ, may reach the condition of total internal reflection at the semiconductor/ITO interface or the ITO/air interface, and hence, the light can be trapped in the semiconductor layers with multiple passes. In addition, the growth of nc-Si:H also produces extra features as previously observed. In this case, the growth of nc-Si:H could not be conformal with the substrate morphology, and therefore, the effective light trapping can be achieved by large micro-features on the substrate.

4.6. Summary

We have studied the correlations between the preparation conditions and micro-features on the Ag/ZnO BRs, as well as solar cell performance. We can control the micro-feature size by adjusting the deposition condition and subsequent chemical etching process. The RMS measured by AFM varies from 30 to 120 nm. For a-SiGe:H, we find that the improved Ag/ZnO BR with large micro-features leads to an enhanced V_{oc}. We believe that the increase in the micro-feature size reduces the density of the sharp peaks on the BR surface and consequently reduces the back diffusion of photo-generated carriers at the *n/i* and *i/p* interfaces. It can also decrease the shunt current density. Hence, the cell performance was improved. For nc-Si:H solar cells, a clear gain in the J_{sc} has been observed by increasing the micro-feature size on the BR surface, which is due to the effective light trapping by optimizing surface morphology on the BR.

Table XII: BR properties and nc-Si:H solar cell performance. The J-V characteristics were measured under an AM1.5 solar simulator with J_{sc} obtained from QE

Sample #	BR #	Etching (sec)	RMS (nm)	P_{max} (mW/cm^2)	J_{sc} (mA/cm^2)	V_{oc} (V)	FF
L15204	R7947	0	33.3	5.87	20.52	0.485	0.590
L15203	R7947	30	62.2	7.32	21.48	0.500	0.682
L15201	R7900	0	80.5	7.06	22.62	0.480	0.650
L15196	R7900	20	107.3	7.10	24.10	0.483	0.610

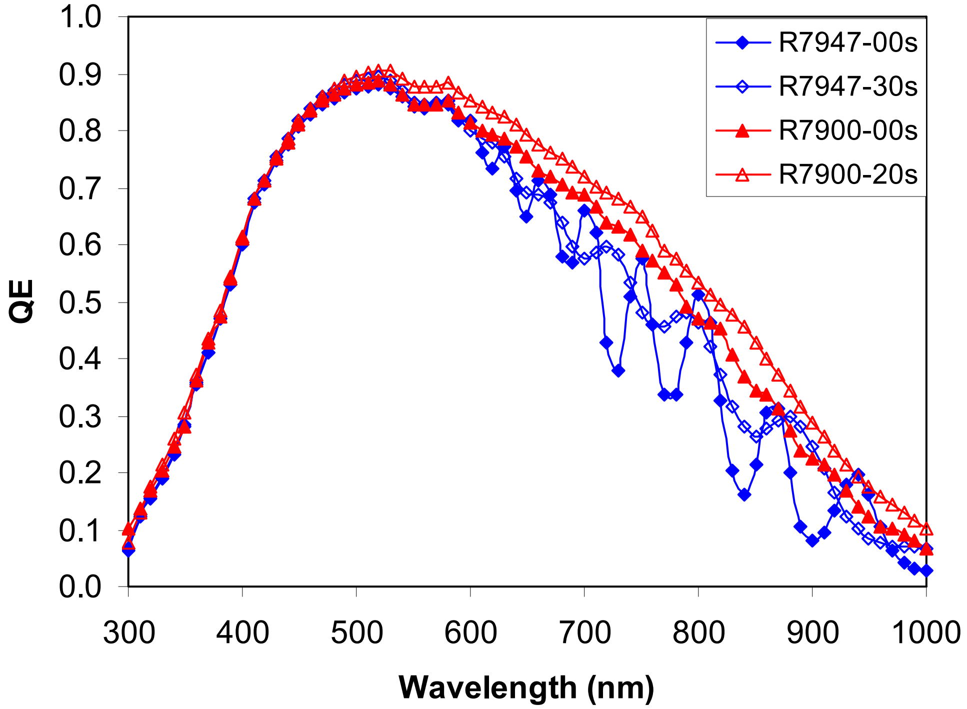

Figure 24. QE curves for nc-Si:H solar cells deposited on different BRs as described in Table XII.

Section 5: High Efficiency Multi-junction Cell with nc-Si:H Bottom Cell

As described in the previous section, we have made significant progress in optimization of nc-Si:H solar cells, and achieved an initial active-area efficiency of 8.4% with nc-Si:H single-junction cells. In addition, the Ag/ZnO BR is also re-optimized for the nc-Si:H solar cells. The main purpose of developing nc-Si:H is for use in multi-junction structures. In this section, we present our best a-Si:H/nc-Si:H double-junction and a-Si:H/a-SiGe:H/nc-Si:H triple-junction solar cells.

5.1. Optimization of a-Si:H/nc-Si:H double-junction solar cell

To achieve a high efficiency a-Si:H/nc-Si:H double-junction cell, we need to have an optimized a-Si:H top cell and a nc-Si:H bottom cell as well as the tunnel *p/n* junction that connects the top and bottom cells. At United Solar, we have accumulated a lot of experience for making high performance a-Si:H top cells. Therefore, the main task focused on the nc-Si:H bottom cell. As shown in Fig. 12, we have obtained reasonably good nc-Si:H single-junction cells. We used a similar recipe in an a-Si:H/nc-Si:H double-junction structure and achieved an initial active-area efficiency of 13.45%. Figure 25 shows (a) the J-V characteristics and (b) quantum efficiency of the best a-Si:H/nc-Si:H double-junction cell. The J_{sc} is calculated from the quantum efficiency measurement of the bottom cell, which is measured up to 1000 nm. At this wavelength, the cell has a response of ~15% indicating that the current contribution of the bottom cell, and thereby the total current density from the QE, would be higher if the measurements could go beyond 1000 nm.

The J-V characteristics of the same double-junction cell were also measured under a blue light (<585 nm) or a red light (>610 nm). Under the blue light, light-absorption/current-generation is predominantly in the top cell. Since the top and bottom cells are connected in series, the external current is limited by the bottom cell. In this case, the measured FF reflects the bottom cell FF under a reduced light intensity. It was found that the bottom cell FF is 0.802, which is much better than the single-junction nc-Si:H shown in Fig. 12. This result suggests that the nc-Si:H bottom cell quality is indeed superior to that of the a-SiGe:H alloy bottom cell.

Table XIII: Stability comparison of different a-Si:H/nc-Si:H double-junction solar cells made using RF at low rates. The underlined data are the limited current densities.

Sample No.	State	Efficiency (%)	J_{sc} (mA/cm^2)		V_{oc} (V)	FF
			Top	Bott.		
13986	Initial	12.99	12.35	12.12	1.437	0.746
	Stable	10.88	11.57	11.88	1.405	0.669
	Degradation	16.2 %	6.3 %	1.9 %	2.2 %	10.3 %
14066	Initial	12.29	12.15	11.31	1.420	0.765
	Stable	11.15	11.48	11.25	1.396	0.710
	Degradation	9.3 %	5.5 %	0.5 %	1.7 %	7.2 %
14643	Initial	13.45	12.75	12.61	1.439	0.741
	Stable	**11.81**	12.22	12.38	1.399	0.691
	Degradation	12.2%	4.2%	1.8%	2.8%	6.7%

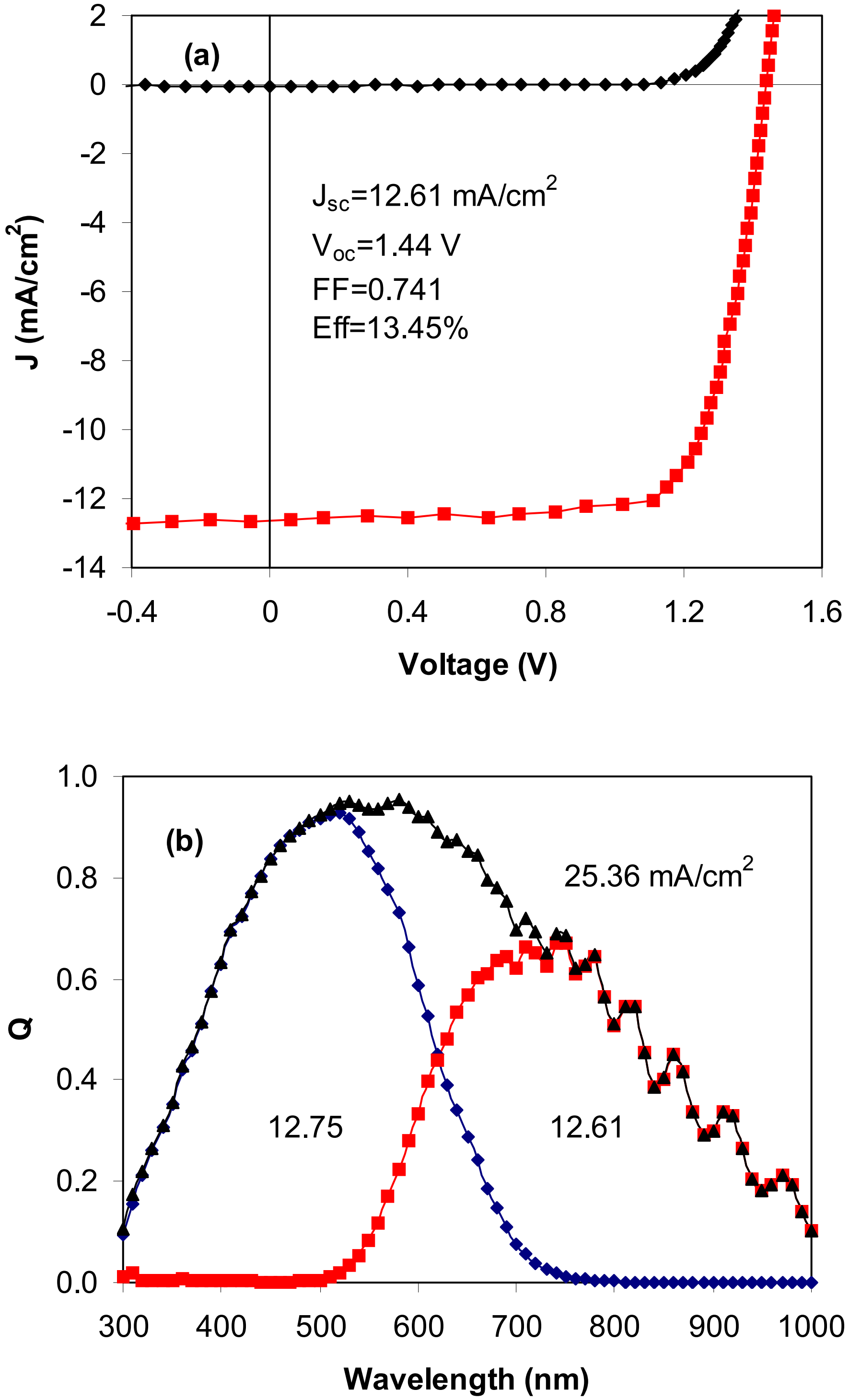

Figure 25. (a) J-V characteristics and (b) quantum efficiency of an a-Si:H/nc-Si:H double-junction solar cell with an initial active-area efficiency of 13.45%.

Under the red light, the J-V characteristics reflect the top cell performance. The FF of 0.750 is similar to a single-junction a-Si:H top cell under a low light intensity illumination.

The stability under prolonged light soaking is an important issue for a-Si:H based solar cells. We have performed light soaking experiments for a-Si:H/nc-Si:H double-junction cells under 100 mW/cm^2 of white light at 50 °C for over 1000 hours. Table XIII summarizes the initial and stable performance for three representative solar cells. The best cell stabilized at 11.8% active-area efficiency, which corresponds to a total-area stable efficiency of 11.0%. It has been noticed that the cell with a bottom cell limited J_{sc} shows a lower light-induced degradation than those with matched current between the top and bottom cells.

5.2. Optimization of a-Si:H/a-SiGe:H/nc-Si:H triple-junction solar cell

By incorporating the improved nc-Si:H cell in an a-Si:H/a-SiGe:H/nc-Si:H triple-junction structure, we have obtained an initial active-area efficiency of 14.6%, which ties the record of the initial efficiency achieved using the a-Si:H/a-SiGe:H/a-SiGe:H triple-junction structure [1]. We also did the stability experiment on the high efficiency a-Si:H/a-SiGe:H/nc-Si:H triple-junction solar cells. A standard light soaking condition has been used with 100 mW/cm^2 of white light at 50 ºC for more than 1000 hours.

Table XIV lists initial and stable J-V characteristics of a series of a-Si:H/a-SiGe:H/nc-Si:H triple-junction solar cells. The highest stable efficiency was 12.6% from Line 14866. This cell degraded by 13.5%, which is mainly from the reduction of FF. Figure 26 shows the J-V characteristics of the cell with the highest stable efficiency. From the QE spectra, one can see that the bottom cell response does not change after the light soaking, but the top cell and middle cell degraded. Overall, the stable efficiency is not better than the best stable efficiency of 13% achieved using an a-Si:H/a-SiGe:H/a-SiGe:H triple-junction cell [1]. Although the nc-Si:H bottom cell does not degrade very much, the thicker a-Si:H top cell and a-SiGe:H middle cell might have caused the high overall degradation.

Table XIV: Stability of a-Si:H/a-SiGe:H/nc-Si:H triple-junction solar cells made using RF glow discharge at low rate. The underline QE data indicate the limiting current densities.

Sample	State	Eff (%)	J_{sc} (mA/cm^2)	V_{oc} (V)	FF	QE (mA/cm^2)		
						T	M	B
14863	Initial	14.55	8.52	2.190	0.780	8.72	9.37	8.52
	Stable	**12.59**	8.33	2.128	0.710	8.33	8.98	8.43
	Deg.	13.5%	2.2%	2.8%	9.0%	4.5%	4.2%	1.1%
14866	Initial	14.59	8.76	2.184	0.762	8.85	9.21	8.76
	Stable	12.35	8.40	2.125	0.692	8.40	8.76	8.68
	Deg.	15.4%	4.2%	2.7%	10.0%	4.2%	4.9%	0.9%
14876	Initial	12.32	7.29	2.136	0.791	8.56	8.62	7.29
	Stable	11.20	7.12	2.136	0.737	8.38	8.11	7.12
	Deg.	9.1%	2.3%	0%	6.8%	2.1%	5.9%	2.3%
14877	Initial	13.93	8.33	2.194	0.762	8.91	8.81	8.33
	Stable	12.44	8.28	2.141	0.702	8.59	8.39	8.28
	Deg.	10.7%	0.6%	2.4%	7.9%	3.4%	4.6%	0.6%

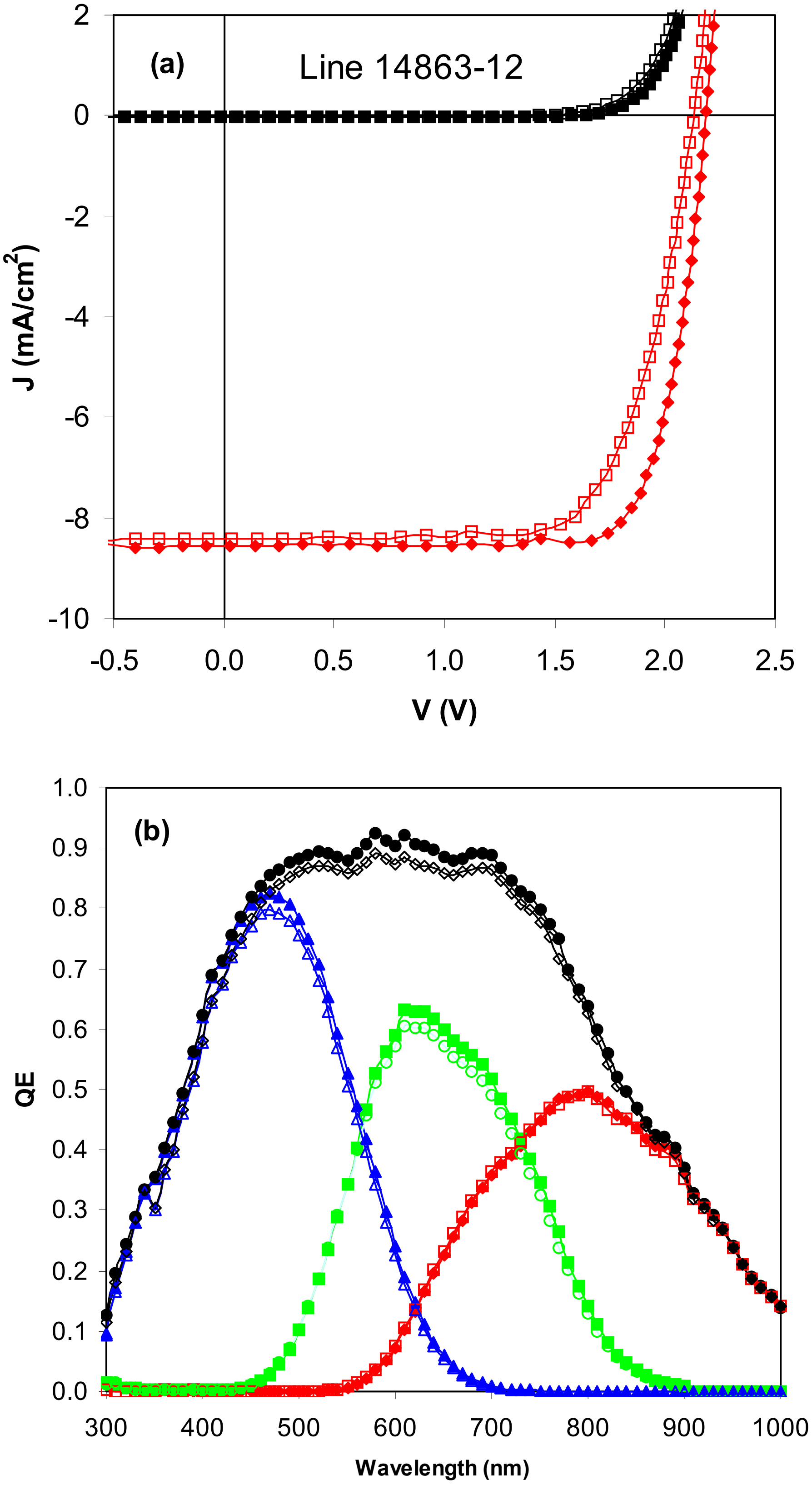

Figure 26. (a) J-V characteristics and (b) quantum efficiency of an a-Si:H/a-SiGe:H/nc-Si:H triple-junction cell at the initial (solid symbols) and stable (open symbols) states.

Section 6: High Rate Deposition of nc-Si:H Single-junction and Multi-junction Solar Cells Using Modified VHF Glow Discharge

6.1. Introduction

As discussed in section 1, nc-Si:H appears to have a potential for substituting the a-SiGe:H bottom cell in the multi-junction solar cells. At United Solar, we decided to explore the possibility of using nc-Si:H in our multi-junction solar cells. The first issue is the deposition rate. Normally, nc-Si:H is deposited with a very high hydrogen dilution rate, which significantly reduces the deposition rate. It is very well known that the nc-Si:H deposition rate is much lower than that of a-Si:H under similar conditions except for a lower hydrogen dilution rate. In order to solve the deposition issue, many techniques have been developed by different research groups. Among them, the VHF glow discharge has been widely used for high-rate nc-Si:H deposition partially due to a lower ion energy and a higher ion flux intensity [12, 13]. Recently, the VHF glow discharge with high pressure and high power has shown a remarkable advantage in improving nc-Si:H solar cell performance [31-33]. We have evaluated all the possibilities for high-rate nc-Si:H deposition and believe that our MVHF is the first choice because this technique has been proven to be a good method for high rate nc-Si:H deposition and we have accumulated some experiences using this technique in making a-Si:H and a-SiGe:H alloy solar cells. Although the deposition rate is a critical factor to determine whether a deposition technique can be used or not in solar cell manufacturing, the actual deposition time of each layer is a main parameter for machine design. For a thicker nc-Si:H layer, the deposition rate should be higher than for a thinner layer if the deposition time is fixed. Based on our experience of machine design, we believe that a deposition time of 20-30 minutes of nc-Si:H intrinsic layer deposition time is a good target for this program. As shown in Fig. 27, for an intrinsic layer of 1-2 μm with 30 minutes of deposition time, the deposition rate should be around 6 to 12 Å/s. In this program, we have used the MVHF to make nc-Si:H solar cells at high rates. The first goal is to achieve a high efficiency with 30 minutes of nc-Si:H intrinsic layer deposition time. With our consistent effort, we have achieved initial active-area efficiencies of 8.3%, 13.1%, and 13.8% with nc-Si:H single-junction, a-Si:H/nc-Si:H double-junction, and a-Si:H/a-SiGe:H/nc-Si:H triple-junction solar cells, respectively.

6.2. Experimental

A multi-chamber system with three RF chambers and one MVHF chamber is used to deposit nc-Si:H single-junction and multi-junction solar cells. The *n-i-p* structures were deposited on Ag/ZnO BR coated SS substrates. The a-Si:H and nc-Si:H intrinsic layers were prepared using the MVHF glow discharge with an excitation frequency of 65-75 MHz. The doped and buffer layers were deposited with a RF glow discharge, as well as the a-SiGe:H intrinsic layer of the middle cell in the a-Si:H/a-SiGe:H/nc-Si:H triple-junction devices. The solar cells were completed with ITO dots having a total-area of 0.268 cm^2 (active-area of 0.25 cm^2 after the grid fingers) on the top *p* layer. J-V characteristics were measured under an AM1.5 solar simulator at 25 ^{o}C. QE curves were measured from 300 to 1000 nm. Stabilized efficiencies were obtained by over 1000 hours of light soaking under a 100 mW/cm^2 white light at 50 ^{o}C.

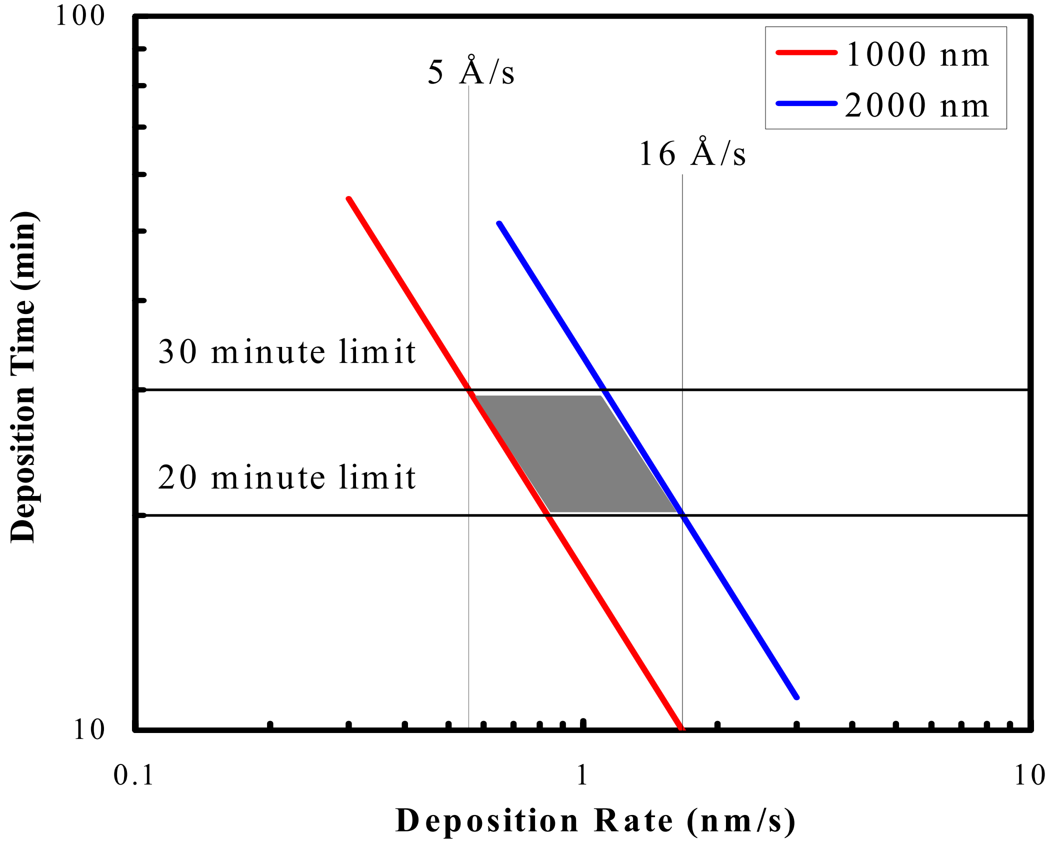

Figure 27. Deposition time for nc-Si:H films as a function of the deposition rate. The shaded region represents the field of interest for solar cell production.

Table XV: Typical J-V characteristics of nc-Si:H single-junction solar cells made using MVHF glow discharge with 30 minutes of intrinsic layer deposition time.

Sample No.	J_{sc} (mA/cm^2)	V_{oc} (V)	FF	Eff (%)
13310	23.08	0.564	0.632	8.23
13348	22.72	0.544	0.660	8.16
13461	23.34	0.559	0.640	8.35
13474	23.43	0.558	0.628	8.21
13491	24.88	0.543	0.599	8.09

6.3. MVHF high rate nc-Si:H single-junction solar cell

For obtaining high efficiency multi-junction solar cells, a prerequisite is to develop a high quality nc-Si:H material and solar cell. Previously, we have reported a nc-Si:H single-junction solar cell with an initial active-area efficiency of 7.7%, where the intrinsic layer was deposited in 50 minutes [34]. As shown in the previous sections, the nc-Si:H solar cells critically depend on the material quality, especially the microstructure. A material containing a high density of microvoids or cracks normally has a high density of defects related to poor grain boundary passivation and contamination due to post oxygen diffusion [14]. We have found that the increase of grain size and crystalline volume fraction with increasing thickness is the main obstacle for obtaining high efficiency in thick nc-Si:H solar cells as discussed in Section 3. To solve this problem, we used the hydrogen dilution profiling technique to keep the nc-Si:H material structure close to the nanocrystalline/amorphous transition region throughout the entire intrinsic layer, as discussed in the previous section. The hydrogen dilution profiling technique has been proven as a useful method for improving the nc-Si:H performance (see Section 3). Recently, we have used the hydrogen dilution profiling technique in the MVHF high-rate deposition and made a significant progress in the cell efficiency. Table XV lists some nc-Si:H single-junction solar cells with 30 minutes of intrinsic layer deposition time. These cells show initial active-area (0.25 cm^2) efficiencies of over 8%. The J-V characteristics and quantum efficiency of the best cell are shown in Fig. 28, which has an initial active-area efficiency of 8.35%. There are two other major factors contributing to the high efficiency nc-Si:H solar cells. First, we explored new plasma parameters such as the high pressure and high power regime. Second, we modified the VHF deposition chamber based on the uniformity in the thickness and cell performance. Compared to the old record cell with an efficiency of 7.7% (J_{sc}=21.3 mA/cm^2, V_{oc}=0.528 V, FF=0.683) reported in the Phase II annual report, the new record cell shows higher J_{sc} and V_{oc}, even through the deposition time was decreased from 50 minutes to 30 minutes. The higher J_{sc} is mainly due to the increased thickness of the intrinsic layer. Previously, without using hydrogen dilution profiling, the J_{sc} decreases with an increase of the thickness when the thickness is over a critical value. Now, we can increase the intrinsic layer thickness to a higher value without any loss in J_{sc}. As shown in Fig. 4 of section 3, V_{oc} normally decreases with thickness dramatically. We used to have difficulties in obtaining V_{oc} over 0.5 V for nc-Si:H with an intrinsic layer thickness of over 1 μm. Now, the champion cell shows a V_{oc} over 0.55 V. We believe that the improved V_{oc} is also due to the improved nc-Si:H intrinsic layer quality by using proper hydrogen dilution profiling and other newly developed plasma parameters. In addition, the optimized *n/i* and *i/p* buffer layers also play an important role.

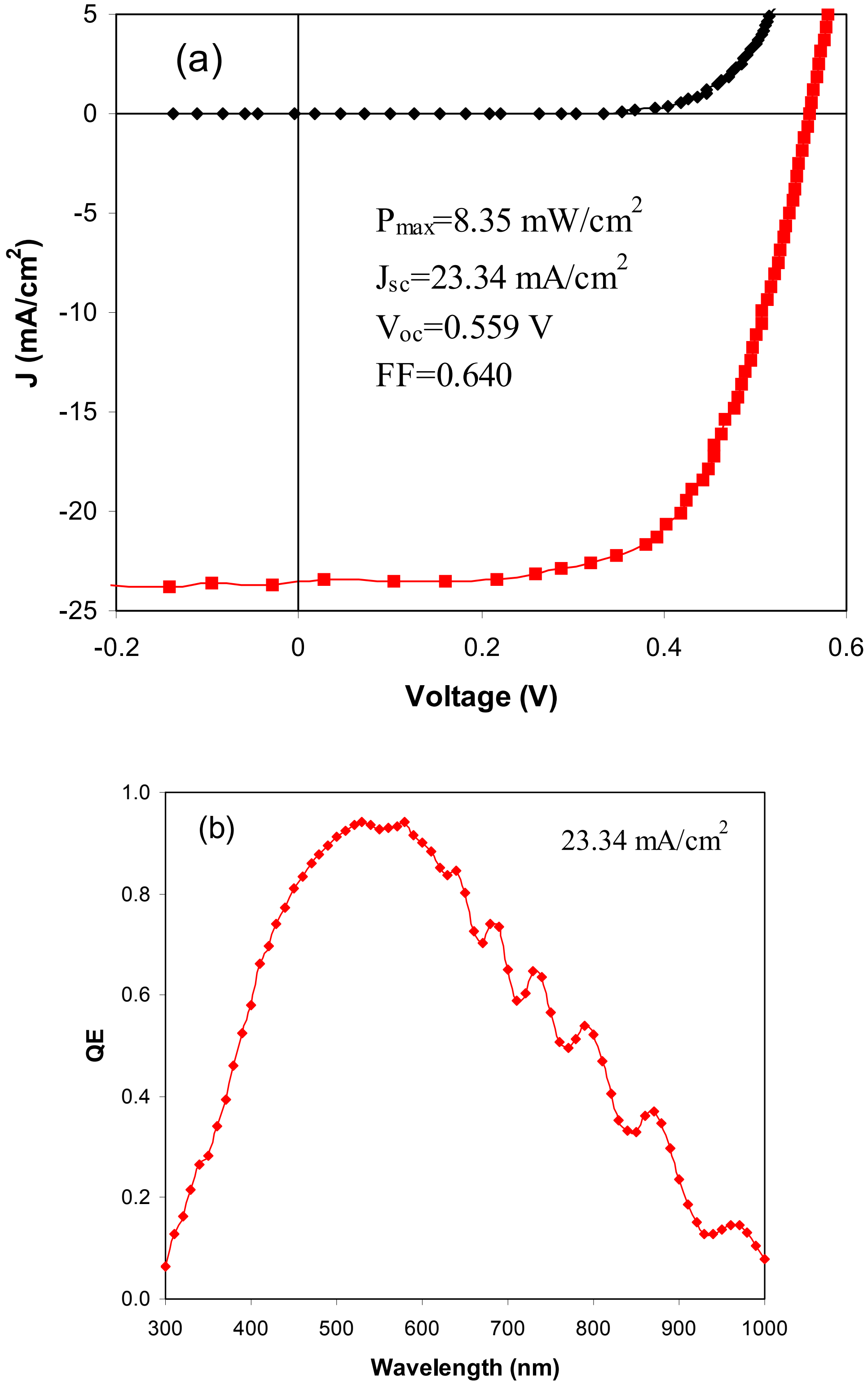

Figure 28. (a) J-V characteristics and (b) quantum efficiency of a nc-Si:H single junction solar cell with an intrinsic layer thickness of 0.6 µm.

Table XVI: J-V characteristics of a-Si:H/nc-Si:H double-junction solar cells made in the first year using MVHF with different bottom cell deposition times (t).

Sample No.	t (min)	Eff. (%)	QE(mA/cm^2)		J_{sc} (mA/cm^2)	Voc (V)	FF
			Top	Bott.			
12065	210	12.51	11.54	11.45	11.45	1.425	0.767
11569	60	12.04	12.09	12.07	12.07	1.359	0.734
11635	50	12.33	11.91	11.99	11.91	1.392	0.744
11797	35	11.34	11.77	10.73	10.73	1.385	0.763
11835	30	11.35	11.19	11.10	11.10	1.406	0.727

6.4. a-Si:H/nc-Si:H double-junction cells made with MVHF at high rates

The technical issues for the high-rate MVHF a-Si:H/nc-Si:H double-junction cell are similar to the low-rate double-junction cell discussed in Section 5. Therefore, the experience and knowledge learned in the low rate are mostly useful for the high rate deposition. Except that the high quality a-Si:H top cell and nc-Si:H bottom cell are optimized separately, a special attention is paid to the current mismatching between the top and bottom cells and tunnel-junction. Details are given in the previous quarterly and annual reports. In the first year, we have achieved an initial active-area efficiency of over 12% with a nc-Si:H intrinsic layer in the bottom cell deposited in 50 minutes. Table XVI summarizes the a-Si:H/nc-Si:H with different bottom cell intrinsic layer deposition times. It clearly shows the difficulties in making high efficiency a-Si:H/nc-Si:H with shorter deposition time for the bottom cells.

As presented above, we have made significant progress in optimizing the nc-Si:H at high deposition rates and achieved an initial active-area efficiency of 8.35%. We incorporated the improved nc-Si:H bottom cell in an a-Si:H/nc-Si:H structure and achieved the initial active-area efficiency of over 13%. Figure 29 shows the (a) J-V characteristics and (b) QE curve of the champion cell. This cell was also measured under an AM1.5 illumination with blue (<585 nm) and red (>610 nm) filters to evaluate the bottom and top cell performance. A FF of 0.846 was

Table XVII: J-V characteristics of a-Si:H/nc-Si:H tandem solar cells made using MVHF at high deposition rates at the initial and light-soaked states, where the a-Si:H and nc-Si:H intrinsic layers in the top and bottom cells were made with 10 and 30 minutes.

Sample No.	Status	V_{oc} (V)	FF	Q(mA/cm^2)		J_{sc} (mA/cm^2)	Eff (%)
				Top	Bottom		
R13528	Initial	1.445	0.755	12.00	12.17	12.00	13.1
	Light soaked	1.407	0.678	11.54	12.20	11.54	11.0
	Degradation	2.63%	10.2%	3.83%	0	3.83%	16.0%
R13536	Initial	1.444	0.741	12.28	12.12	12.12	13.0
	Light soaked	1.406	0.657	11.82	12.13	11.82	10.9
	Degradation	2.63%	11.3%	3.75%	0	2.48%	16.2%
R13580	Initial	1.454	0.750	12.67	11.68	11.68	12.7
	Light soaked	1.419	0.694	12.27	11.72	11.72	**11.5**
	Degradation	2.41%	7.47%	3.16%	0	0	9.44%

obtained under the blue light and 0.768 under the red light, which indicates the high quality nc-Si:H bottom and a-Si:H top cells, respectively.

Several high-rate MVHF a-Si:H/nc-Si:H double-junction cells were selected for light soaking under 100 mW/cm^2 of white light at 50 °C. Currently, 750 hours of light soaking has been performed. Table XVII lists the cell performance at the initial and light-soaked states. The highest stable active-area efficiency is 11.5%, which corresponds to a stable total-area efficiency of 10.7%.

6.5. a-Si:H/a-SiGe:H/nc-Si:H triple-junction cells made with MVHF at high rates

During this program, we have also investigated the a-Si:H/a-SiGe:H/nc-Si:H triple-junction cell using MVHF at high rates. At the first stage, we used an a-SiGe:H middle cell made using RF at a low rate because the best MVHF high-rate a-SiGe:H middle cells were made at a relatively higher substrate temperature than the nc-Si:H bottom cell deposition temperature; the a-Si:H top and nc-Si:H bottom cells were deposited using MVHF at high deposition rates. The nc-Si:H intrinsic layers in the bottom cells were deposited for 50-60 minutes. The best initial active-area efficiency achieved is 13.8%, and the J-V characteristics and quantum efficiency are shown in Fig. 30.

As known from our previous reports, the light-induced degradation strongly depends on the current mismatching in a-Si:H/nc-Si:H double junction solar cells. The degradation could be 5% for a cell with a strong bottom-cell-limited current mismatching to 16% for a cell with a matched current or a top-cell limited current mismatching. A similar experiment was done with the MVHF a-Si:H/a-SiGe:H/nc-Si:H triple-junction solar cells. Table XVIII lists the initial and stabilized cell performance for four cells with different current mismatching. One can see the cell (#12468) with a strong bottom-cell-limited current mismatching has the lowest light-induced degradation. Clearly, it benefits from the bottom-cell-limited design. Overall, the a-Si:H/a-SiGe:H/nc-Si:H triple-junction cells show a degradation in a range from 8.5 to 19%, which is similar to the degradation in a-Si:H/nc-Si:H double-junction solar cells. The highest active-area stable efficiency for the a-Si:H/a-SiGe:H/nc-Si:H triple-junction cell is 11.4%, which is from the cell with an initial active area efficiency of 12.8%. The cell with the highest initial active-area efficiency of 13.8% (#12852) does not have the highest stable efficiency. Actually, this cell degrades by 18% due to the smaller middle cell current after light soaking. Compared to a-Si:H/nc-Si:H double-junction cells, the a-Si:H/a-SiGe:H/nc-Si:H triple-junction cells do not show better stability. The reason could be that although the top cell is thinner in the triple-junction structure, the degradation in the less stable a-SiGe:H middle cell has affected the overall light-induced degradation.

6.6. Summary

We have made nc-Si:H single-junction solar cells using MVHF at high deposition rates and achieved an initial active-area efficiency of 8.35% with a nc-Si:H intrinsic layer deposition time of 30 minutes. The corresponding deposition rate is about 7 Å/s. We used the improved nc-Si:H cell as the bottom cell in the a-Si:H/nc-Si:H double-junction structures. An initial active-area

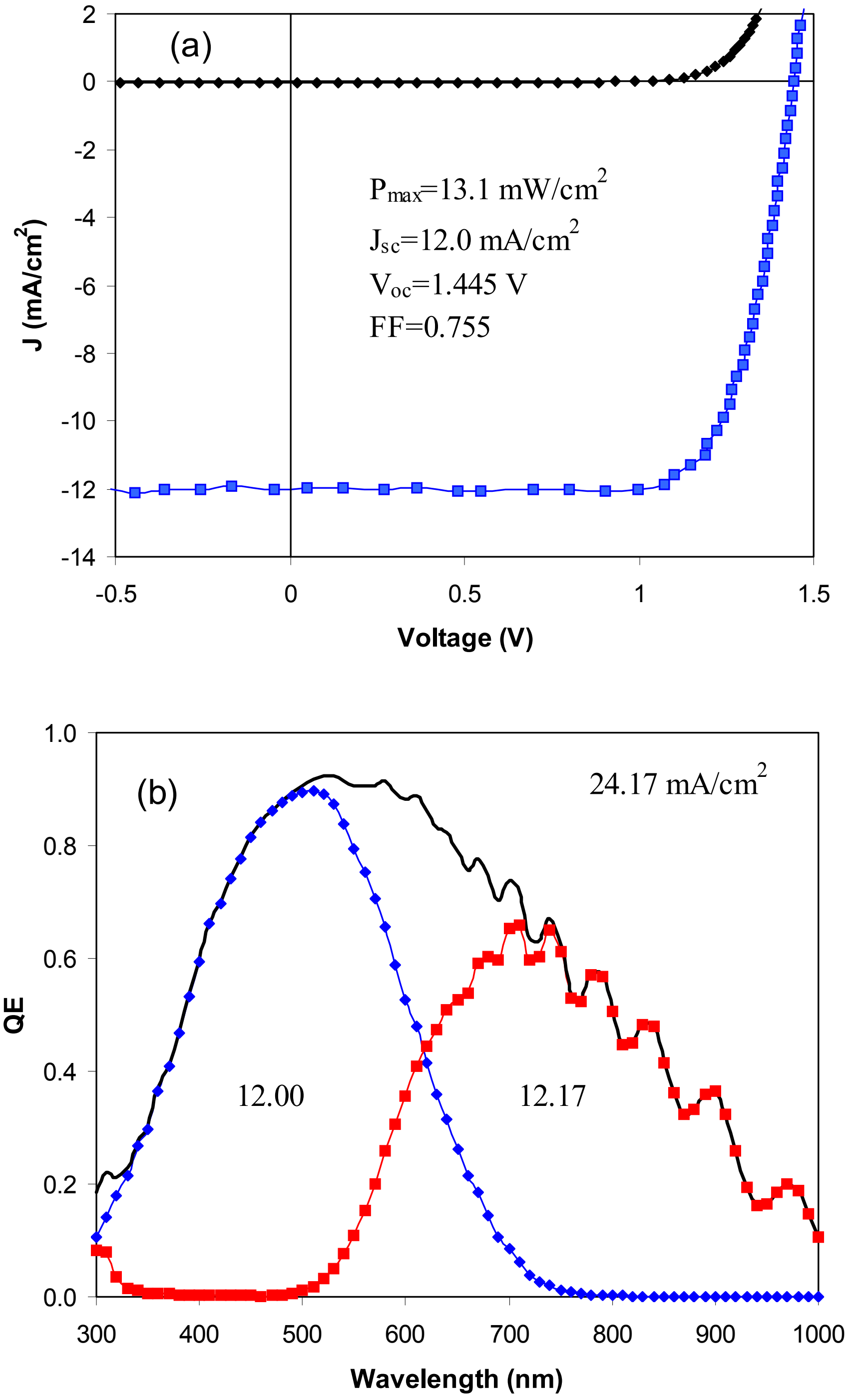

Figure 29. (a) Initial and stable J-V characteristics, and (b) quantum efficiency in an a-Si:H/nc-Si:H double-junction solar cell made with MVHF at high rates.

Table XVIII: Initial and stable J-V characteristics of four a-Si:H/a-SiGe:H/nc-Si:H triple-junction solar cells with nc-Si:H bottom cells made with MVHF at high rate. The numbers in bold are the limiting current densities. The stabilized efficiencies are in red.

Sample No.	State	V_{oc} (V)	FF	J_{sc} (mA/cm^2)	Q (mA/cm^2)			Eff (%)
					Top	Mid.	Bott.	
12427	Initial	2.203	0.730	7.42	8.19	**7.42**	7.68	11.93
	Stable	2.122	0.669	7.18	7.93	**7.18**	7.69	10.19
	Degr.	3.68%	8.36%	3.23%	3.17%	3.23%	0%	14.6%
12660	Initial	2.146	0.760	7.20	7.20	**8.22**	7.48	11.74
	Stable	2.092	0.679	7.06	7.06	**8.00**	7.53	10.03
	Degr.	2.52%	10.66%	1.94%	1.94%	2.68%	0%	14.6%
12468	Initial	2.165	0.790	7.16	7.56	7.95	**7.16**	12.25
	Stable	2.117	0.746	7.10	7.34	7.64	**7.10**	11.21
	Degr.	2.27%	5.57%	0.84%	2.91%	3.90%	0.84%	8.5%
12667	Initial	2.159	0.791	7.50	7.61	8.12	**7.50**	12.81
	Stable	2.105	0.725	7.48	7.51	7.90	**7.48**	11.42
	Degr.	2.50%	8.34%	0.26%	1.31%	2.71%	0.26%	10.9%
12852	Initial	2.175	0.786	8.08	8.21	8.17	**8.08**	13.8
	Stable	2.095	0.692	7.76	8.00	**7.76**	7.91	11.3
	Degr.	3.85%	8.34%	4.0%	2.56%	5.02%	2.10%	18.0%
12863	Initial	2.163	0.744	8.04	8.54	**8.04**	8.39	12.9
	Stable	2.086	0.656	7.70	8.27	**7.70**	8.41	10.5
	Degr.	3.52%	9.02%	4.23%	3.16%	4.23%	0	18.6%
12876	Initial	2.195	0.737	8.15	8.31	**8.15**	8.25	13.2
	Stable	2.110	0.676	7.90	7.97	**7.90**	8.18	11.3
	Degr.	3.52%	5.45%	3.07%	4.09%	3.07%	0.85%	14.4%

efficiency of 13.1% has been achieved. We also made a-Si:H/a-SiGe:H/nc-Si:H triple-junction cells, where the nc-Si:H intrinsic layers in the bottom cells were made with MVHF for a deposition time of 50-60 minutes. The best initial active-area efficiency is 13.8%. We conducted light soaking experiments on both the double-junction and triple-junction structures and found that the light-induced degradation is in the range from 8 to 19%, depending on the material quality and the cell current mismatching. A bottom-cell-limited current mismatching results in low light-induced degradation in both a-Si:H/nc-Si:H double-junction and a-Si:H/a-SiGe:H/nc-Si:H triple-junction structures. Stable efficiencies of 11.5% and 11.4% have been obtained using an a-Si:H/nc-Si:H double-junction and an a-Si:H/a-SiGe:H/nc-Si:H triple-junction structure, respectively.

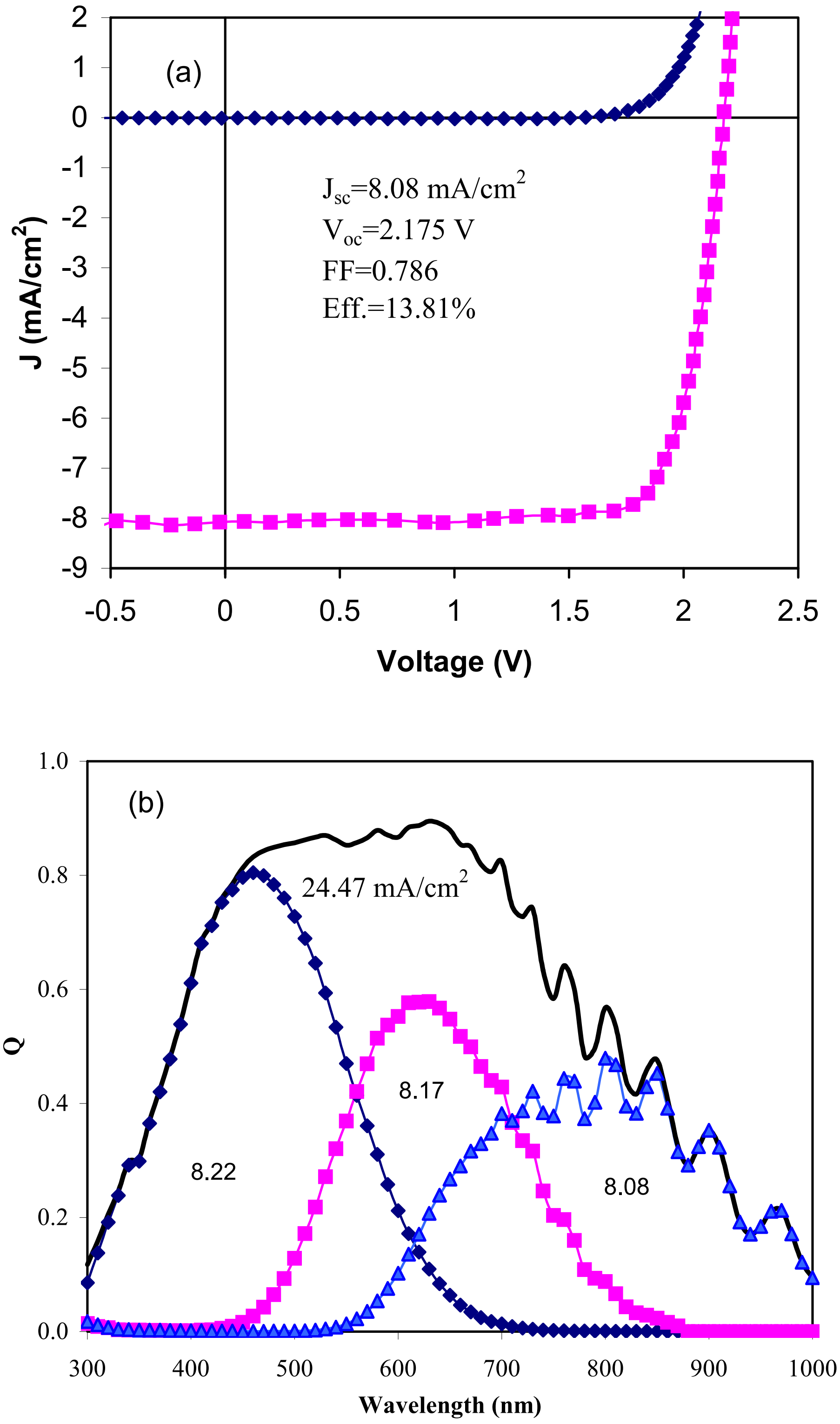

Figure 30. (a) J-V characteristics and (b) quantum efficiency of an a-Si:H/a-SiGe:H/nc-Si:H triple-junction solar cell, where the bottom cell was made using MVHF at high rate and the top and middle cells used RF at a low rate.

Section 7: High Rate Deposition of nc-Si:H Solar Cells Using RF Glow Discharge in the High Pressure Regime

7.1. Introduction

As reported in the literature, successful methods for high rate deposition of nc-Si:H solar cells are VHF glow discharge [12-13, 20] and RF glow discharge under high pressures with high power [18-20]. As an industrial R&D group, we need to evaluate both methods and study the feasibility of each method for the manufacturing process. We have made significant efforts in the deposition of nc-Si:H solar cells using MVHF, and reasonable results have been obtained as presented in the previous section. During the second year (2003) of the program, we started the study of high-rate nc-Si:H deposition using RF glow discharge under high pressure with high power. Initially, we deposited nc-Si:H single-junction and a-Si:H/nc-Si:H double-junction cells on a small-area substrate (2 in × 2 in). The results are very promising. Then, in the third year of the program, we transferred this technology to the large-area deposition and achieved a remarkable progress. The details of the large-area a-Si:H/nc-Si:H double-junction solar cells will be presented in the following sections.

7.2. Experimental

A multi-chamber RF glow discharge has been used for nc-Si:H solar cell deposition. Single-junction nc-Si:H *n-i-p* cells were deposited on Ag/ZnO back reflector coated stainless steel substrates. The doped layers were deposited using the same optimized conditions as used for conventional a-Si:H/a-SiGe:H/a-SiGe:H triple-junction solar cells. We have searched in the parameter space for the intrinsic nc-Si:H layer deposition conditions, including hydrogen dilution, substrate temperature, RF power, and pressure. We found that a higher hydrogen dilution is required to reach the transition from amorphous to nanocrystalline under a higher pressure. A high substrate temperature helps to reduce the required hydrogen dilution, but better solar cells were made at a relatively low temperature and with a higher hydrogen dilution.

7.3. RF high rate nc-Si:H single-junction cell

As expected, the high pressure RF glow discharge suffered from uniformity problems. The cell performance is not uniform even on a 2"×2" substrate. Table XIX lists the J-V characteristics of nc-Si:H solar cells at different locations on the substrate. It appears that the

Table XIX: Initial active-area J-V characteristics of nc-Si:H single-junction cells made with RF under high pressure at high rates. The nc-Si:H deposition time was 60 minutes.

Sample #	Position	Eff (%)	J_{sc} (mA/cm^2)	V_{oc} (V)	$FF_{AM1.5}$	FF_{blue}	FF_{red}
7693	Center	6.6	21.44	0.517	0.598	0.662	0.670
	Edge	6.3	22.10	0.497	0.573	0.639	0.638
	Corner	5.6	23.60	0.468	0.509	0.604	0.601
7699	Center	6.7	22.48	0.494	0.605	0.651	0.604
	Edge	6.5	23.57	0.474	0.580	0.624	0.597

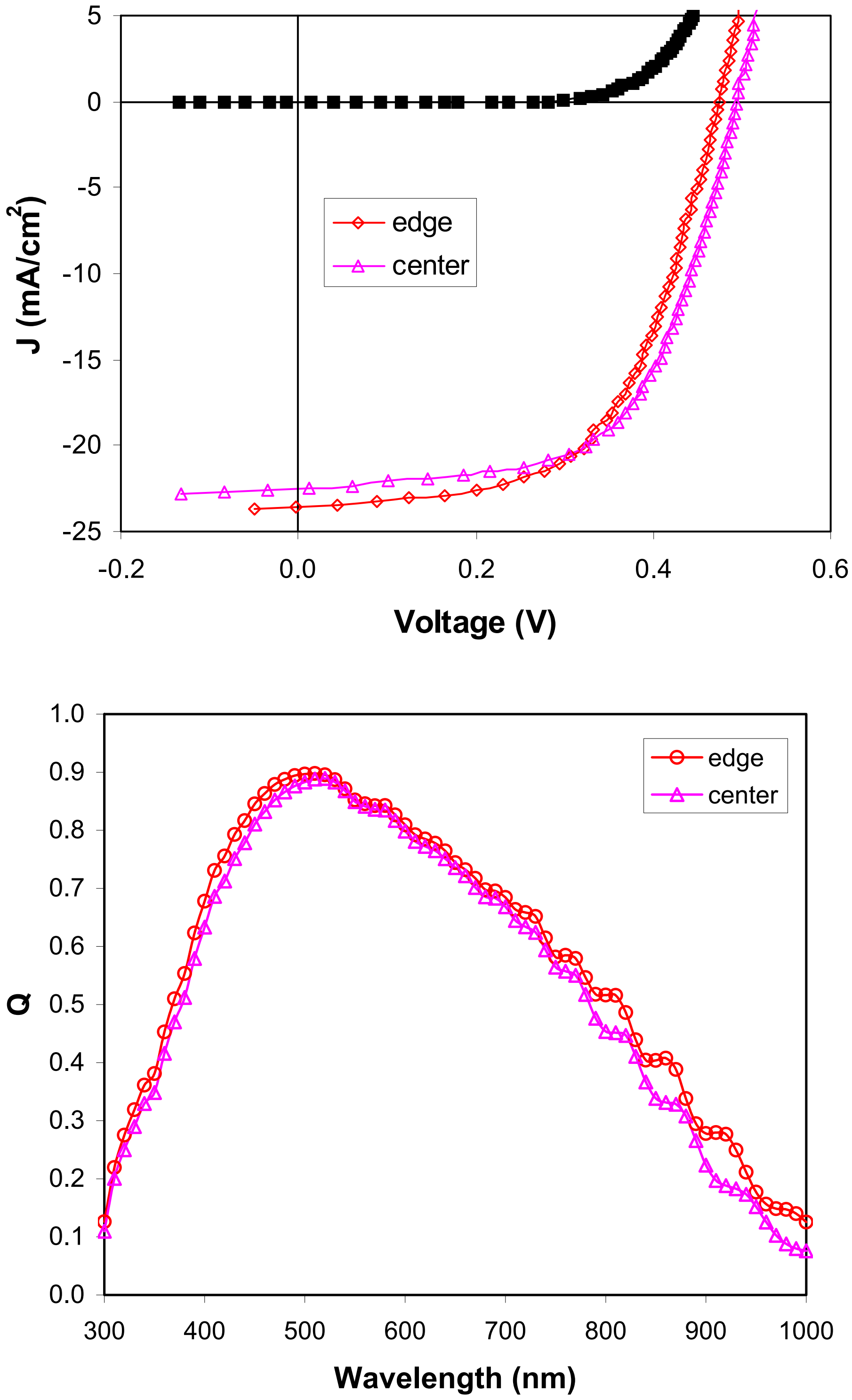

Figure 31. (upper) J-V characteristics and (lower) quantum efficiency of nc-Si:H single-junction cells at the center and the edge of the substrate. The nc-Si:H layer was deposited using high pressure RF glow discharge at ~ 3 Å/s for 60 minutes.

cells in the center have high V_{oc} but low J_{sc}, indicating a low nanocrystalline volume fraction in the center. The highest efficiency for single-junction nc-Si:H is 6.7%, in which the intrinsic layer was deposited for 60 minutes. Figure 31 shows the J-V characteristics and quantum efficiencies of cells in the center and at the edge. From the quantum efficiency plot, one can see the long wavelength response is higher for the cell on the edge than in the center. The uniformity depends not only on the plasma parameters such as pressure, gas flow and RF power, but also on the reactor geometry such as the shape of the cathode and the gap between the cathode and the anode. Based on the properties of the high pressure RF plasma, we have modified the cathode structure in the 2B system and minimized the non-uniformity problem for the high-pressure and high-power deposition with the large-area system, and achieved a reasonable uniformity in both thickness and cell performance as described in the next section.

7.4. a-Si:H/nc-Si:H double-junction solar cells with RF glow discharge under high pressure and high power

We used the RF high rate nc-Si:H cell as the bottom cell in an a-Si:H/nc-Si:H double-junction structure, and achieved an initial active-area efficiency of 12.3%, where the bottom cell nc-Si:H layer was deposited for 2 hours. Table XX lists the J-V characteristics of three cells made with different bottom cell deposition times, and Figure 32 plots the J-V characteristics and quantum efficiency of the best a-Si:H/nc-Si:H double-junction cell.

7.5. Summary

We have started RF glow discharge deposition of nc-Si:H solar cells under a high-pressure regime with high power to achieve a high deposition rate. We achieved an initial active-area efficiency of 6.7% with a nc-Si:H single-junction cell and 12.3% with an a-Si:H/nc-Si:H double-junction cell. Currently, we are working on further optimization of cell efficiency and uniformity. We also need to increase the deposition rate further to reduce the deposition time.

Table XX: Initial active-area J-V characteristics of a-Si:H/nc-Si:H double-junction cells made with RF glow discharge under high pressure at 3 Å/s. t is the nc-Si:H deposition time.

Sample #	t (min)	Eff (%)	QE (mA/cm^2)		J_{sc} (mA/cm^2)	V_{oc} (V)	FF
			Top	Bottom			
7727	60	10.0	12.38	<u>9.60</u>	9.60	1.439	0.722
7742	90	11.9	11.82	<u>11.63</u>	11.63	1.403	0.730
7741	120	12.3	<u>11.89</u>	12.69	11.89	1.410	0.731

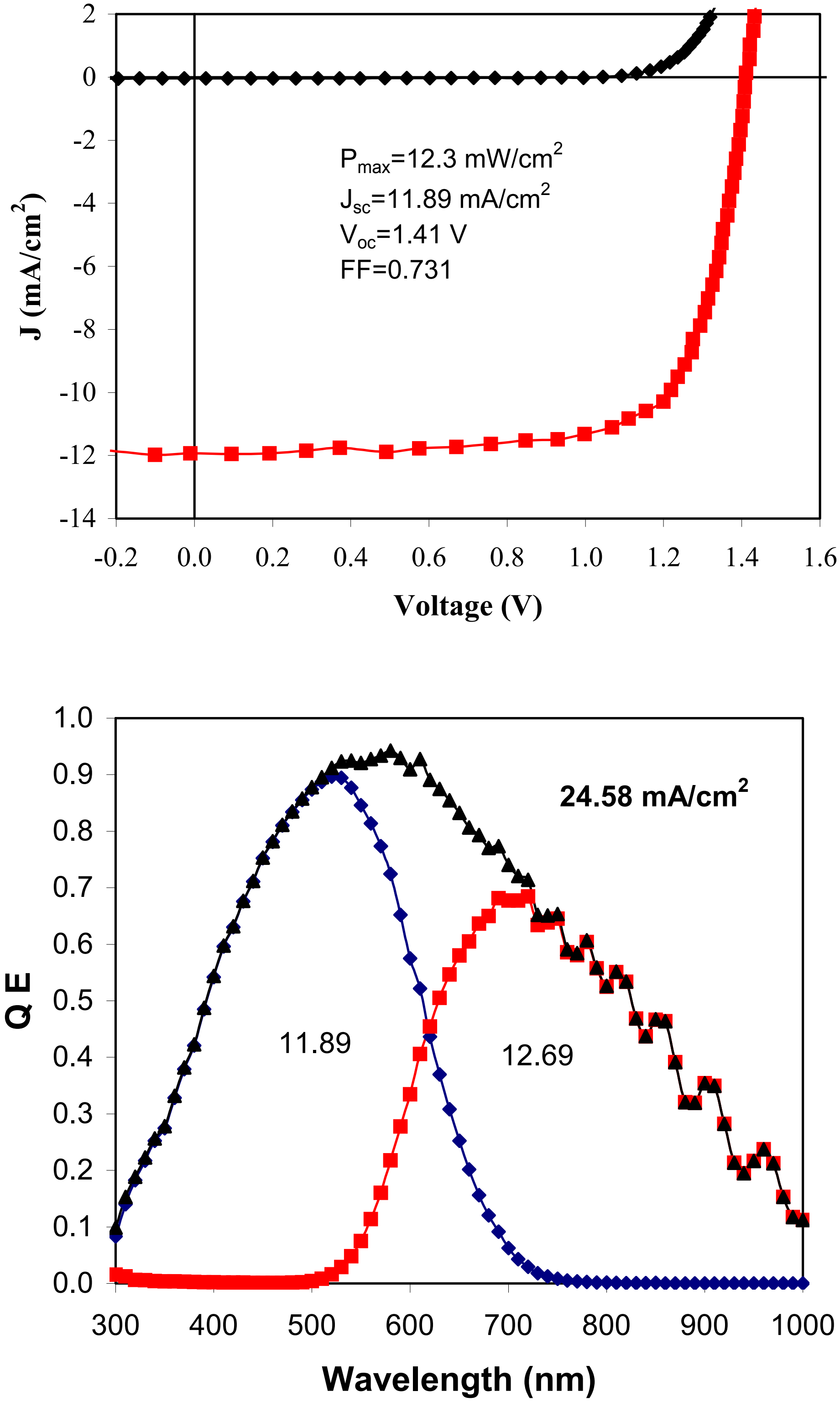

Figure 32. (upper) J-V characteristics and (bottom) quantum efficiency of an a-Si:H/nc-Si:H double-junction cell deposited using high pressure RF glow discharge at ~ 3 Å/s.

Section 8: Large-area a-Si:H/nc-Si:H Double-junction Solar Cells

8.1. Introduction

As presented in the previous sections, we have explored various techniques for nc-Si:H deposition at different rates and made significant progress in both high efficiency and high-deposition rates. In order to use the multi-junction structure with nc-Si:H in the bottom cell, an increase in the deposition rate and improvement of the deposition uniformity on large-area substrates are two major issues that need to be investigated. In this section, we present our progress in the development of large-area a-Si:H/nc-Si:H double-junction solar cells and modules. In the second year of the program, we mainly focused on the issues related to large-area deposition and module fabrication. Therefore, the initial work was limited to the low deposition rate regime. In the third year of the program, we increased the deposition rate by increasing the pressure and RF power. The deposition time for the nc-Si:H intrinsic layer in the bottom cell has been shortened to 50 minutes.

8.2. Experimental

nc-Si:H films and solar cells were deposited using a large-area multi-chamber RF glow discharge system (2B machine) with gas mixtures of H_2 and SiH_4 on substrates with an area of 35×33 cm^2. a-Si:H/nc-Si:H double-junction solar cells with an *n-i-p* structure were deposited on Ag/ZnO back-reflector coated stainless steel substrates. The thicknesses of the intrinsic a-Si:H and nc-Si:H layers are about 2000-3000 Å and 1-2 μm, respectively. ITO dots were deposited on top of the *p* layer as a transparent contact. Metal grids or wires were used to reduce the series resistance and improve the collection of current. The thickness uniformity was measured on different locations using an optical method, and the uniformity of the cell performance was characterized by evaluating small-area cells defined by ITO dots with an active-area of 0.25 cm^2 on the *p* layer of the large-area a-Si:H/nc-Si:H double-junction cells. The J-V characteristics were measured under an AM1.5 solar simulator at 25 °C. The QE curves were measured for wavelengths from 300 nm to 1000 nm. Modules with aperture areas of 45 cm^2 and 460 cm^2 (some modules have an aperture-area of 420 cm^2) were made using our conventional module fabrication procedure. The module efficiency was measured under a Spire solar simulator. The light soaking experiment was done under 100 mW/cm^2 of white light at 50 °C.

8.3. Uniformity of thickness and cell performance

Uniform cell performance ensures high efficiency of large-area solar cells and modules. The thickness uniformity depends on the cathode structure and deposition parameter. By incorporating an improved cathode and optimizing the deposition conditions, we have improved the thickness uniformity. The thickness non-uniformity for the nc-Si:H films is within 15% in a 30×30 cm^2 area and less than 10% in an area of 460 cm^2. The uniformity of cell performance was characterized by measuring the small-area cells (0.25 cm^2) defined by ITO dots at different locations over the large-area deposition. Figure 33 (a) shows the distribution of the conversion efficiency of a sample across a 22×22 cm^2 area. The value at each position represents the average efficiency of the cells with an active-area of 0.25 cm^2 on a 4×4 cm^2 piece. One can see that the cells with the highest efficiency are located in the center area of the substrate. The cells on the edge have lower efficiencies, whereas the cell efficiency is the lowest at the corners. The performance non-uniformity is similar to the thickness non-uniformity. Overall, the uniformity in the central area of 460 cm^2 is acceptable for module fabrication. Figure 33 (b) shows the distribution of the efficiency for all the cells with an active-area of 0.25 cm^2. The efficiency is in the range from 10% to 12% with a peak position at ~ 11.5%. The highest efficiency after QE correction for J_{sc} is 12.1% for a small-area cell on this substrate. Recently, we have modified the deposition chamber based on the requirement of high rate nc-Si:H deposition and re-optimized the deposition parameters. The best a-Si:H/nc-Si:H double-junction solar cell shows initial and stable active-area efficiencies of 13.3% and 11.7%, respectively. These results are similar to the champion cell achieved by using the small-area machine. Figure 34 shows the initial and stable J-V characteristics and quantum efficiency of the best a-Si:H/nc-Si:H double-junction cell made using the large-area machine.

8.4. Large-area a-Si:H/nc-Si:H double-junction modules made at low rates

Several a-Si:H/nc-Si:H double-junction modules with areas of 45 and 461 cm^2 were fabricated. Figure 35 shows a picture of three modules. The best aperture-area efficiency is 11.8% for the 45-cm^2 cell and 11.3% for the 461-cm^2 one. Figure 36 shows the J-V characteristics of the two solar cells. The solar cells with a larger area of ~ 460 cm^2 were encapsulated. The results are listed in Table XXI. After encapsulation, the efficiency decreased by ~ 6-7%, which is slightly more than the loss in the conventional lamination for a-Si:H/a-SiGe:H/a-SiGe:H triple-junction cells. The loss of the efficiency is mainly due to the reduction of the short-circuit current density. The highest efficiency of the encapsulated large-area module is 10.6 %.

Table XXI. J-V characteristic of the large-area a-Si:H/nc-Si:H modules made at low rates before and after encapsulation.

Sample No.	State	Area (cm^2)	V_{oc} (V)	I_{sc} (A)	FF	P_{max} (W)	Eff. (%)
9446	Unencapsulated	462	1.409	5.304	0.694	5.191	11.23
	Encapsulated	460	1.400	4.860	0.703	4.782	10.40
9456	Unencapsulated	461	1.402	5.317	0.690	5.139	11.12
	Encapsulated	456	1.395	4.914	0.693	4.750	10.42
9461	Unencapsulated	461	1.419	5.432	0.676	5.211	11.30
	Encapsulated	458	1.408	5.008	0.688	4.849	10.59
9464	Unencapsulated	460	1.427	5.239	0.651	4.864	10.57
	Encapsulated	458	1.420	4.756	0.658	4.445	9.71

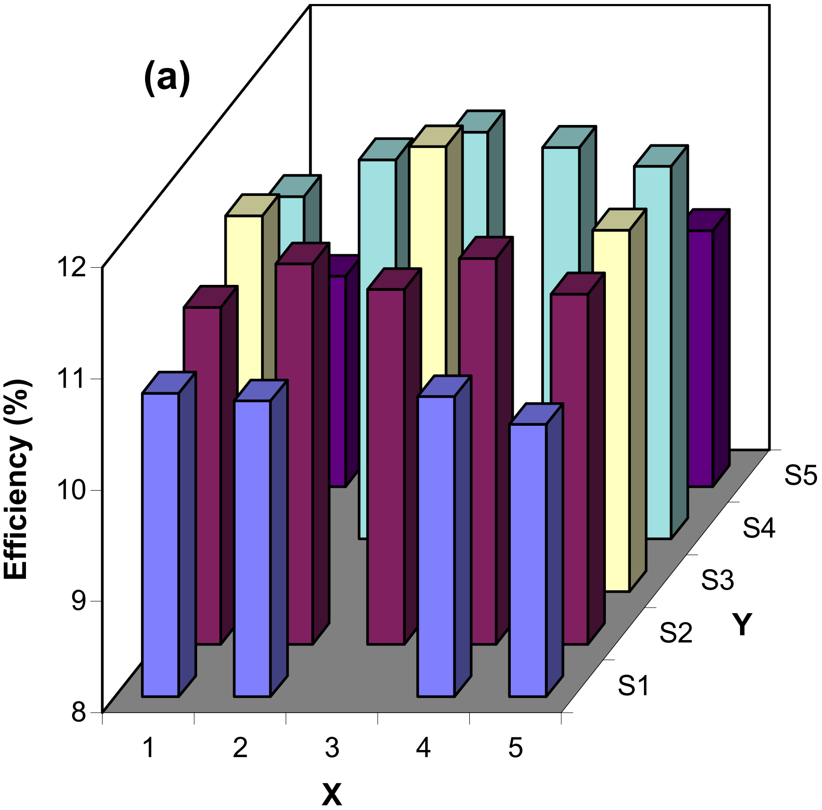

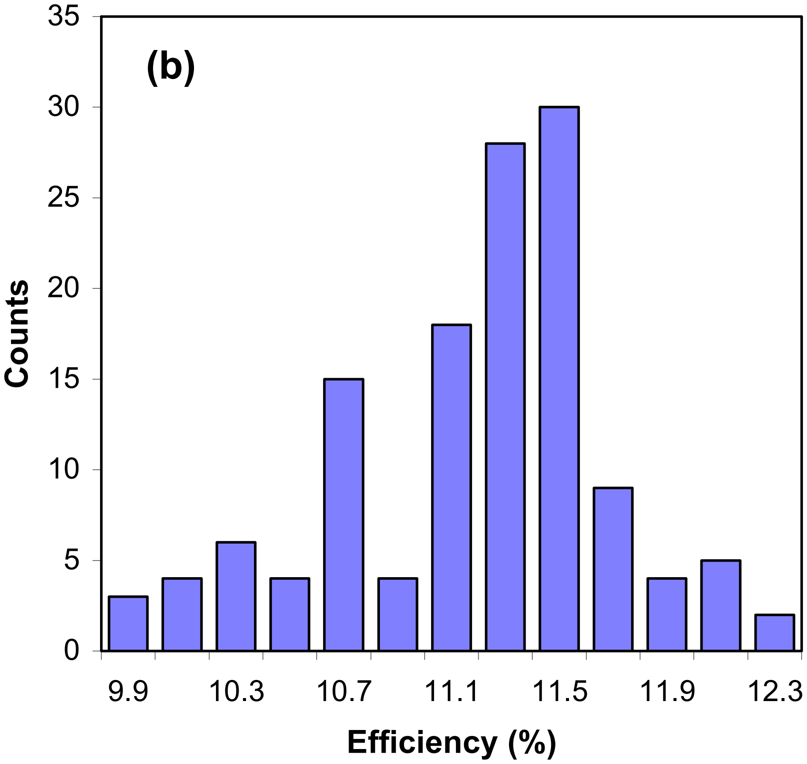

Figure 33. (a) Spatial distribution of solar cell efficiency over a large-area substrate. Each unit on the X-axis and Y-axis is about 4 cm. (b) The distribution of efficiency of sample 9504.

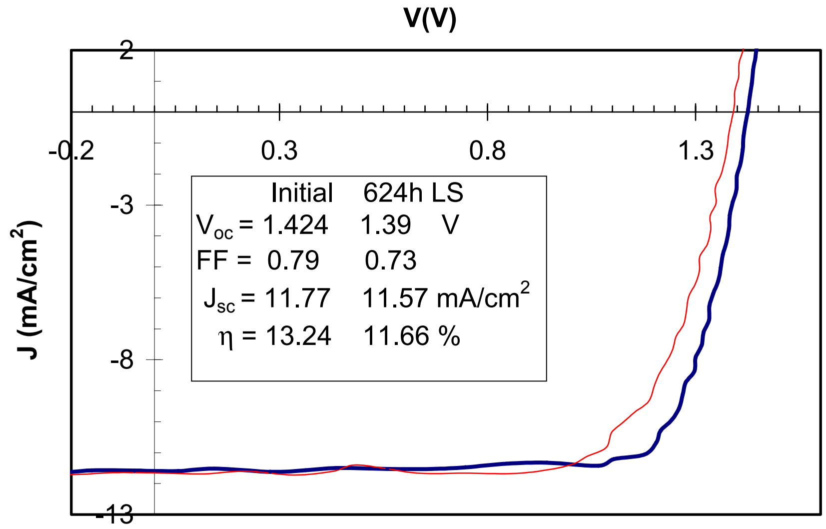
V(V)
J (mA/cm^2)
2
-3
-8
-13
-0.2
0.3
0.8
1.3
Initial 624h LS
V_{oc} = 1.424 1.39 V
FF = 0.79 0.73
J_{sc} = 11.77 11.57 mA/cm^2
η = 13.24 11.66 %

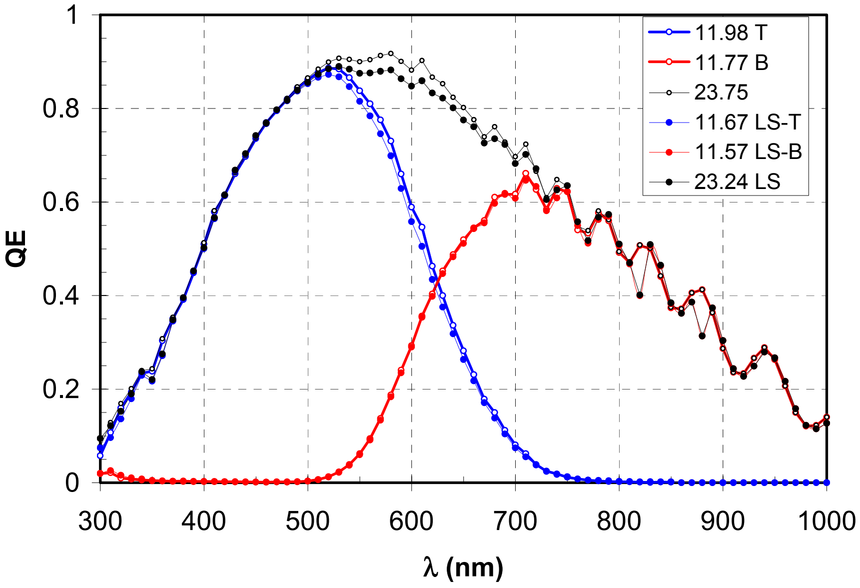
QE
1
0.8
0.6
0.4
0.2
0
300
400
500
600
700
800
900
1000
λ (nm)
11.98 T
11.77 B
23.75
11.67 LS-T
11.57 LS-B
23.24 LS

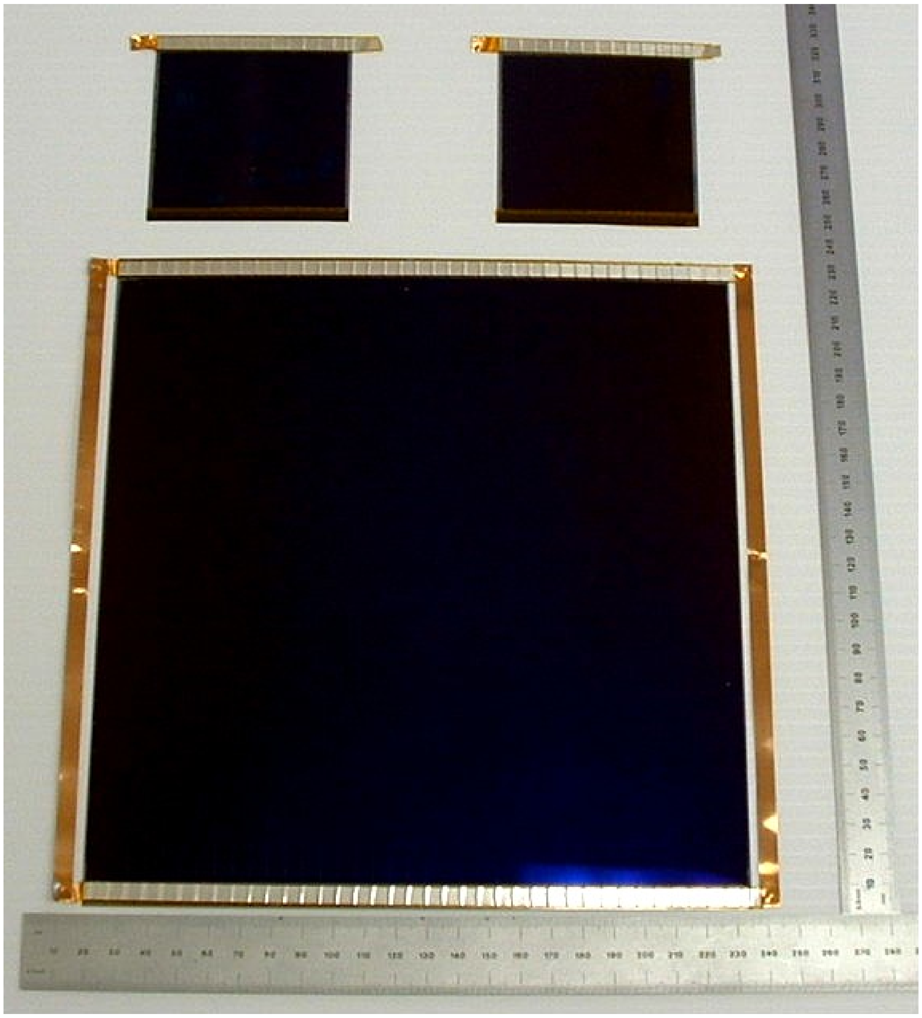

Figure 35. a-Si:H/nc-Si:H double-junction modules on textured Ag/ZnO coated stainless steel substrates with aperture areas of 45 cm^2 (top) and 461 cm^2 (bottom).

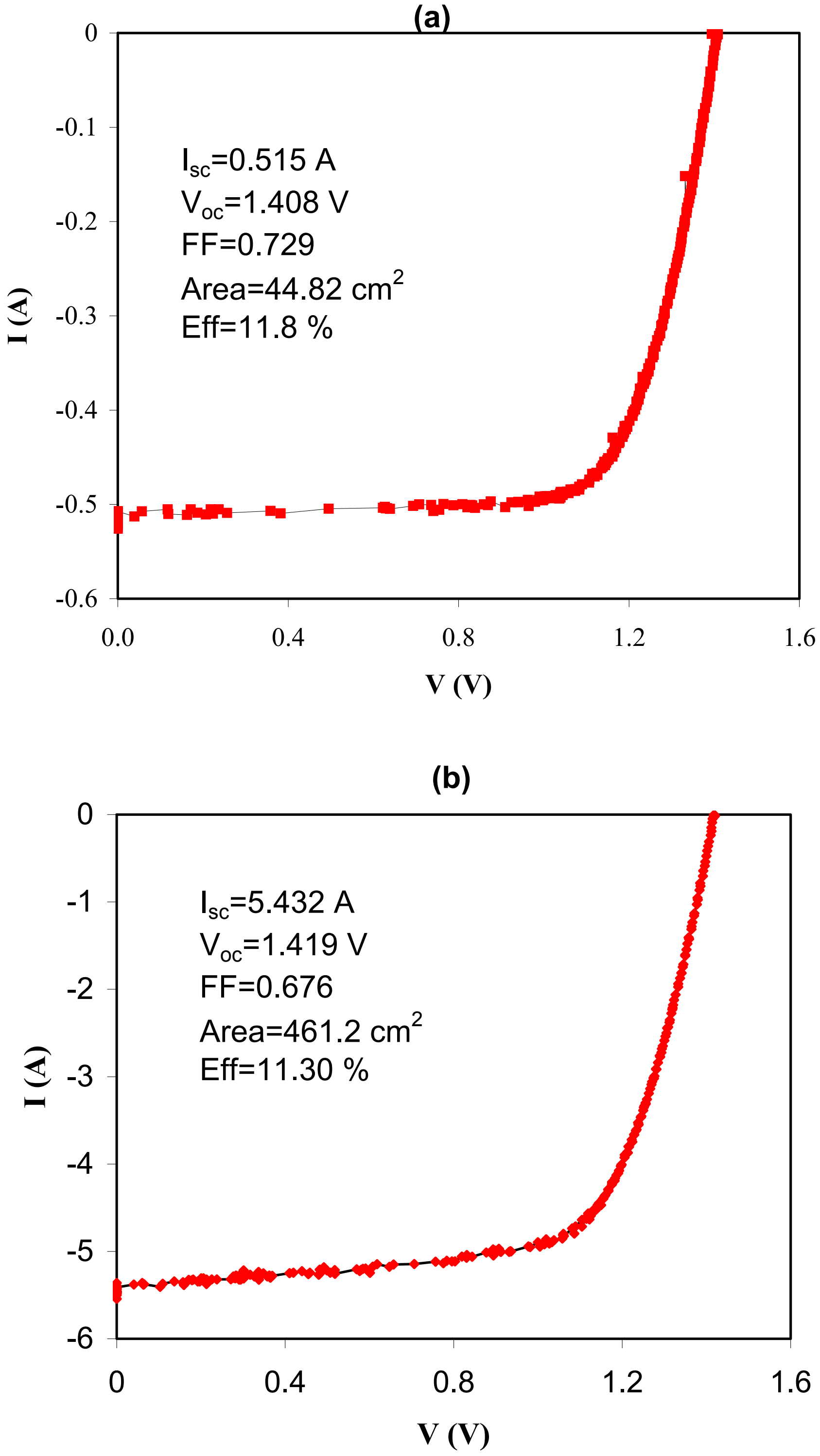

Figure 36. J-V characteristics of a-Si:H/nc-Si:H double-junction cells with aperture areas of (a) 45 cm^2 and (b) 461 cm^2.

Table XXII: Stability of a-Si:H/nc-Si:H double-junction modules after 1050 hours of light soaking under 100 mW/cm^2 of white light at 50 ^oC.

Sample No.	Area (cm^2)	State	V_{oc} (V)	I_{sc} (A)	FF	P_{max} (W)	Eff. (%)
9446	460	Initial	1.400	4.860	0.703	4.782	10.40
		Stabilized	1.378	4.774	0.662	4.356	9.48
		Degradation	1.57 %	1.77 %	5.83 %	8.91 %	8.9 %
9456	456	Initial	1.395	4.914	0.693	4.750	10.42
		Stabilized	1.373	4.817	0.648	4.283	9.40
		Degradation	1.58 %	1.97 %	6.49 %	9.83 %	9.8 %
9461	458	Initial	1.408	5.008	0.688	4.849	10.59
		Stabilized	1.378	4.827	0.638	4.246	9.27
		Degradation	2.13 %	3.61 %	7.27 %	12.44 %	12.4 %
9464	458	Initial	1.420	4.756	0.658	4.445	9.71
		Stabilized	1.399	4.631	0.633	4.104	8.96
		Degradation	1.48 %	2.63 %	3.82 %	7.67 %	7.7 %

As shown in the previous sections, we find that the a-Si:H/nc-Si:H double-junction solar cells degrade by 5 to 20% depending on the material quality and cell structure, especially the current mismatching. We also light soaked the encapsulated a-Si:H/nc-Si:H large-area modules, and summarized the results in Table XXII. The degradation is in the range of between 8 to 12%, similar to the results obtained from small area solar cells. The highest stabilized module efficiency is 9.5%. The measurement at NREL obtained an aperture-area efficiency of 9.2%.

8.5. High rate nc-Si:H single-junction cell deposited on large-area substrate with RF glow discharge under high pressure and high power

As presented in Section 7, we have made a-Si:H/nc-Si:H double-junction cells using the high-pressure RF glow discharge at high rates. In Phase III, we used this technique in our large-area machine. In this subsection, we present the effect of increasing the deposition rate by increasing the pressure and RF power. First, we show the result of nc-Si:H single-junction cells on Ag/ZnO back reflectors, where the nc-Si:H layer was deposited in 50 minutes. The nc-Si:H solar cells were deposited on a large-area substrate and then cut into small pieces (2×2 in^2). ITO dots with a 0.25-cm^2 active-area were deposited on the *p* layer for J-V and quantum efficiency measurements. It has been reported that when using higher power density to increase the growth rate of nc-Si:H material, higher deposition pressure reduces ion bombardment energy, thus increasing the grain size, and leads to a higher solar cell efficiency as well as a better stability

Table XXIII: nc-Si:H solar cell performance for several runs at different deposition pressures. The cells have an active area of 0.25 cm^2.

Cell #	V_{oc} (V)	FF	Pressure	J_{sc} (mA/cm^2)	Eff (%)
10138 LC1	0.336	0.407	Low	18.02	2.46
10153 LC1	0.460	0.644	Medium	20.90	6.19
10192 LC1	0.484	0.666	High	22.62	7.29

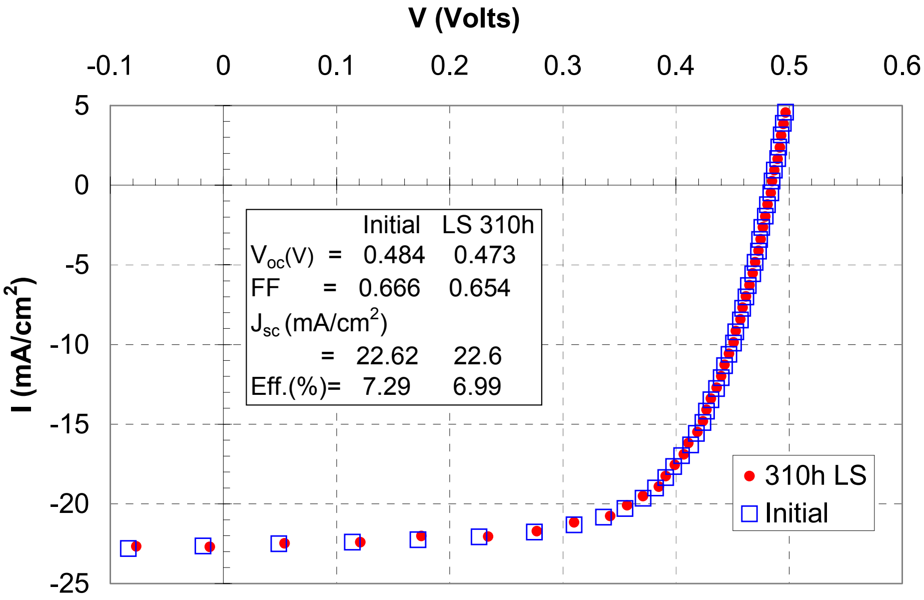

Figure 37. The J-V characteristics of sample 10192LC1 in the initial state and after light soaking for 310 hours under 100 mW/cm^2 of white light illumination at ~50°C.

against atmospheric oxidation [35, 36]. Table XXIII shows the typical performance characteristics as a function of deposition pressure. We observe that the performance improves as the pressure increases. The best nc-Si:H single-junction cell has an active-area efficiency of 7.3%. This cell was light soaked under 100 mW/cm^2 of white light at 50 °C for 310 hours. It degraded by only 4.1%. Figure 37 shows its J-V characteristics at the initial and light-soaked states.

8.6. Small-area a-Si:H/nc-Si:H double-junction cells deposited on large-area substrates with high pressure and high power at high rates

We have used the nc-Si:H single-junction cell deposited with high pressure and high power in an a-Si:H/nc-Si:H structure. At the first step, we fixed the nc-Si:H intrinsic layer time for 50 minutes. Table XXIV lists the initial and light-soaked J-V characteristics of a few small-area (0.25-cm^2 active area) cells cut from a large-area substrate. The V_{oc} and FF measured under an AM1.5 solar simulator with a 610-nm long pass filter (red) or a 585-nm short pass filter (blue) are also given. The best initial and stable efficiencies are 12.0% and 11.3%, respectively. Figure 38 shows the initial J-V characteristics and quantum efficiency of the a-Si:H/nc-Si:H double-junction cell. However, the cell with the highest initial efficiency does not give the highest stable efficiency. The data measured under the color filter and the QE current show that the FF measured under the blue light (bottom cell limited current) does not degrade significantly; on the other hand, the FF measured under the red light (top cell limited current) degrades from about 0.75 to about 0.68. Similarly, the top cell current degrades by about 1-2% while the bottom cell current remains unchanged (within accuracy of QE). From these results, one can see that the degradation of these double-junction cells is clearly dominated by the top cell as would be expected based on our earlier report that the nc-Si:H cells do not degrade under red light (or under a top cell filter) [37].

Table XXIV: Initial and light-soaked performance of a-Si:H/nc-Si:H double-junction cells made using RF glow discharge with 50 minutes of nc-Si:H intrinsic deposition time in the bottom cell. The light soaking experiments were done under a 100 mW/cm^2 of white at 50 °C.

Run	**State**	**Filter**	**V_{oc} (V)**	**FF**	**QE (mA/cm^2)**		**J_{sc} (mA/cm^2)**	**Eff (%)**
					Top	Bottom		
10460 LC1	Initial	>630	1.31	0.751				
		<585	1.35	0.805				
		AM 1.5	1.43	0.785	10.6	10.66	10.60	11.87
	1002h	>630	1.25	0.685				
		<585	1.31	0.809				
		AM 1.5	1.39	0.753	10.42	10.57	10.42	10.91
	Degr.(%)		*2.5*	*4.1*	*1.7*	*0.8*		*8.1*
10461 LC1	Initial	>630	1.3	0.744				
		<585	1.34	0.803				
		AM 1.5	1.42	0.77	10.37	10.65	10.37	11.35
	1002h	>630	1.25	0.691				
		<585	1.31	0.813				
		AM 1.5	1.39	0.738	10.29	10.67		10.56
	Degr.(%)		*2.1*	*4.2*	*0.8*	*-0.2*		*6.9*
10478 LC1	Initial	>630	1.31	0.756				
		<585	1.34	0.805				
		AM 1.5	1.42	0.778	10.87	11.2		12.02
	1002h	>630	1.25	0.683				
		<585	1.3	0.788				
		AM 1.5	1.39	0.725	10.65	11.16		10.72
	Degr.(%)		*2.3*	*6.8*	*2.0*	*0.4*		*10.8*
10485 LC1	Initial	>630	1.29	0.752				
		<585	1.32	0.803				
		AM 1.5	1.4	0.778	11.2	10.98		11.96
	1002h	>630	1.25	0.675				
		<585	1.29	0.802				
		AM 1.5	1.38	0.742	11.07	11.15		11.33
	Degr.(%)		*1.5*	*4.6*	*1.2*	*-1.5*		*5.3*

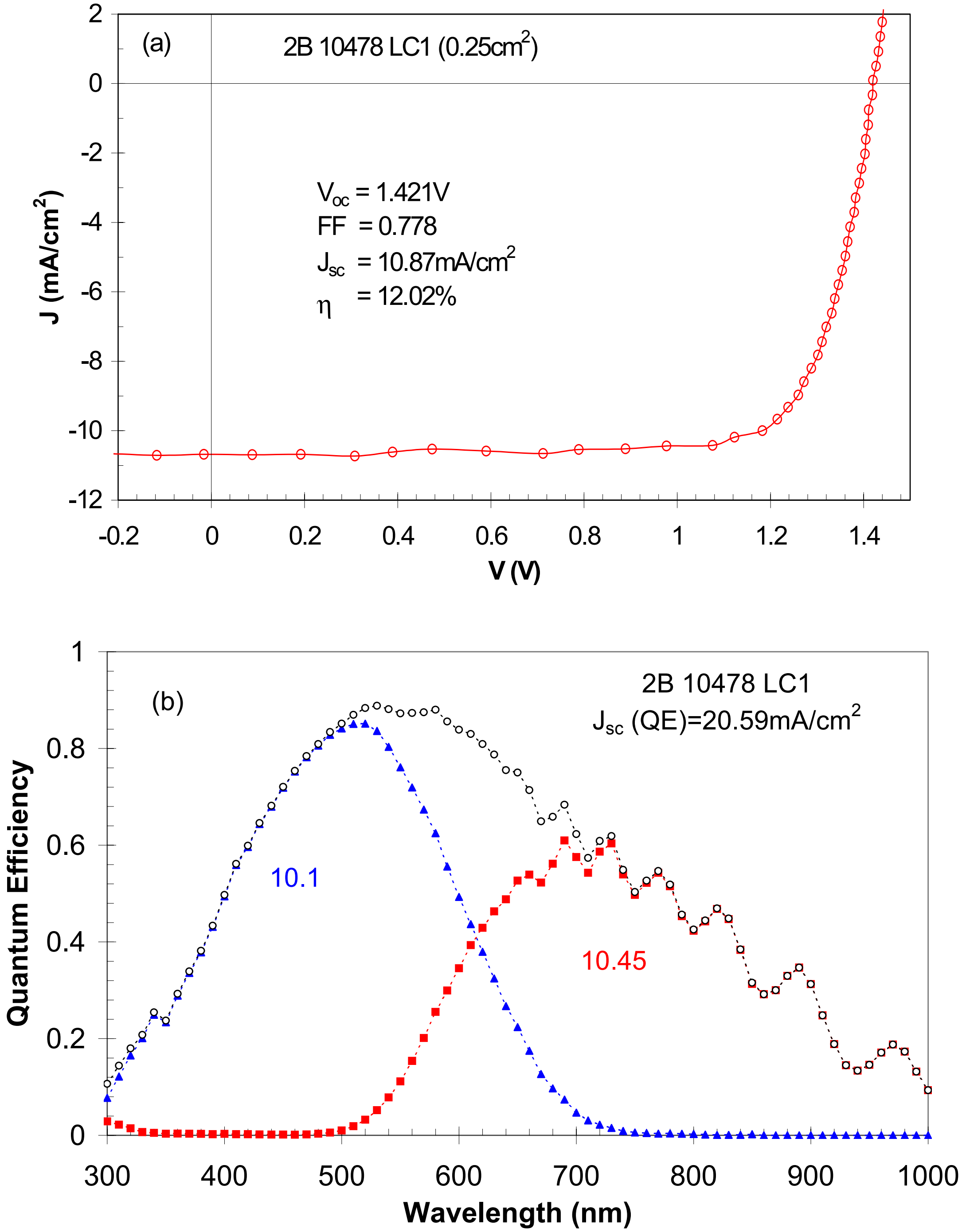

Figure 38. (a) J-V characteristics and (b) quantum efficiency of an a-Si:H/nc-Si:H double-junction solar cell with an active-area (0.25 cm^2) efficiency of 12.0%.

8.7. Large-area a-Si:H/nc-Si:H double-junction cells deposited with RF glow discharge under high pressure and high power at high rates

In order to obtain high-efficiency solar cells with large areas, the uniformity of thickness and cell performance is a critical issue. We have shown that the uniformity at low rates on the large areas is reasonably good (see Fig. 33). For the high rate deposition, we also optimized the plasma conditions and optimized the chamber structure. A very good uniformity of the a-Si:H/nc-Si:H double-junction cell performance over the large area has been achieved. Figure 39 shows the uniformity of the efficiency over an area of 14×24 cm^2 from one deposition run (2B 10478). The coefficient of variation (cov = standard deviation/mean) is 4.8%.

With the uniform high rate deposition, we have made a number of a-Si:H/nc-Si:H double-junction cells of an aperture-area of 45 cm^2. The initial and light-soaked performance of these cells is shown in Table XXV, where the light soaking was carried out under 100 mW/cm^2 of white light at 50 °C. The best initial performance is 12.3%, which is similar to the best obtained on 0.25-cm^2 cells. After 600 hours of light soaking, the best efficiency is 10.9%. One can see that the first two cells show very similar performances since they were made from the same run of deposition. The same situation applies the last three cells in the table. This result confirms the good uniformity in the large-area deposition.

In Table XXVI, we show the efficiency of a-Si:H/nc-Si:H tandem cells of an aperture-area of 420 cm^2. The best initial performance is 11.78%. This record efficiency is slightly lower than that obtained on the smaller area cells. The difference is mainly due to the lower FF. These large area cells were laminated and light soaked under 100 mW/cm^2 of white light for over 500 hours. The light-soaked solar cell parameters are also listed in Table XXVI. The stable

Table XXV: Initial and light-soaked performance of a-Si:H/nc-Si:H double-junction cells with an aperture area of 45 cm^2, where T is the measurement temperature, Eff_m the efficiency at the measurement temperature, and Eff_c the corrected efficiency to 25 °C.

Serial #	State	T (°C)	V_{oc} (V)	FF	J_{sc} (mA/cm^2)	P_{max} (W)	Eff_m (%)	Eff_c (%)
10490F2	Initial	26.6	1.425	0.741	11.40	0.542	12.03	12.07
	600h	*25.4*	*1.403*	*0.688*	*11.25*	*0.489*	*10.86*	*10.87*
10490G3	Initial	26.9	1.437	0.735	11.30	0.536	11.92	11.97
	600h	*25.9*	*1.418*	*0.671*	*11.39*	*0.488*	*10.84*	*10.85*
10491F1	Initial	26.4	1.436	0.742	10.94	0.524	11.65	11.69
	600h	*25.4*	*1.413*	*0.692*	*10.91*	*0.480*	*10.67*	*10.68*
10500F1	Initial	26.6	1.430	0.738	11.46	0.544	12.08	12.12
	600h	*25.6*	*1.409*	*0.665*	*11.43*	*0.482*	*10.71*	*10.72*
10500F2	Initial	26.9	1.432	0.736	11.64	0.552	12.26	12.31
	600h	*25.6*	*1.406*	*0.682*	*11.44*	*0.494*	*10.97*	*10.98*
10500G3	Initial	26.6	1.441	0.743	11.37	0.548	12.18	12.22
	600h	*25.9*	*1.419*	*0.686*	*11.12*	*0.487*	*10.82*	*10.83*

efficiencies are over 9%. The best one shows a stable aperture-area efficiency of 9.6%. Two major losses have been identified. First, the encapsulation process lowered the J_{sc} by 5-10%. Second, the light soaking reduced the V_{oc} and FF due to the Staebler-Wronski effect in the a-Si:H top cell. Comparing to the 300-hour results, we found that the cells became stable after 300 hours of light soaking.

8.8. Summary

In Phase II of the program, we have made large-area deposition of a-Si:H/nc-Si:H double-junction solar cells using RF glow discharge at a relatively low rate ~ 1 Å/s. The thickness uniformity is well within ± 10%. The cell performance uniformity was characterized by depositing ITO dots with an active-area of 0.25 cm^2 on the *p* layer of one large-area a-Si:H/nc-Si:H double-junction solar cell deposition. The small-area cells showed an efficiency distribution in the range from 10% to 12% with a peak position at 11.5% for a given run. After further optimization of the deposition condition and cell structure, the best small-area cell shows an initial active-area efficiency of 13.2%. Preliminary results of large-area a-Si:H/nc-Si:H double-junction structure cells show an initial aperture-area efficiency of 11.8% and 11.3% for 45 cm^2 and 461 cm^2 size un-encapsulated solar cells, respectively. The 11.3% cell became 10.6% after encapsulation and stabilized at 9.5% after prolonged light soaking.

In Phase III, we have increased the deposition rate by increasing the pressure and RF power, along with the modification based on the uniformity in thickness and cell performance. Uniform deposition of a-Si:H/nc-Si:H double-junction solar cells at high rates has been achieved. Initial aperture-area efficiencies of 12.3% and 11.8% have been obtained for cell size of 45 cm^2 and 420 cm^2, respectively. After the encapsulation and light soaking, the 420-cm^2 cells show aperture-area efficiencies over 9%. The best one is 9.5%.

Table XXVI: Initial performance of a-Si:H/nc-Si:H double-junction cells with an aperture area of 420 cm^2, where T is the measurement temperature, Eff_m the efficiency at the measurement temperature, and Eff_c the corrected efficiency to 25 °C. The A state is the as deposited state before encapsulation, the B state is reached after encapsulation and light soaking under 100 mW/cm^2 of white light at 50 °C for 500 hours.

Serial #	State	Temp (°C)	V_{oc} (V)	FF	J_{sc} (mA/cm^2)	P_{max} (W)	Eff_m (%)	Eff_c (%)
10534 (01)	A	26.1	1.425	0.694	11.49	4.770	11.36	11.38
	B	27.6	1.383	0.624	10.6	3.834	9.13	9.18
10536 (03)	A	26.4	1.422	0.708	11.31	4.784	11.39	11.42
	B	27.6	1.382	0.624	10.52	3.807	9.07	9.12
10582 (04)	A	25.6	1.440	0.729	11.21	4.943	11.77	11.78
	B	27.8	1.388	0.628	10.50	3.845	9.15	9.22
10583 (02)	A	25.6	1.435	0.722	11.10	4.829	11.50	11.51
	B	27.6	1.400	0.641	10.38	3.917	9.33	9.38
10587 (05)	A	25.6	1.438	0.689	11.68	4.859	11.57	11.58
	B	27.8	1.400	0.650	10.44	3.987	9.49	9.56

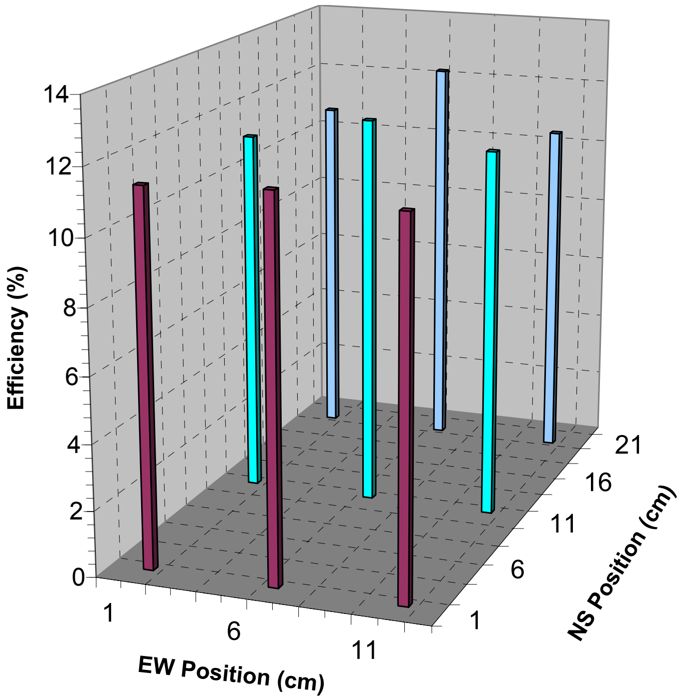

Figure 39. Efficiency distribution of 0.25-cm^2 a-Si:H/nc-Si:H double-junction cells over an area of 14×24 cm^2 from one high-rate deposition run on the 2B system.

Section 9: Metastability in Mixed-Phase Silicon Solar Cells

9.1. Introduction

It has been reported that the best a-Si:H solar cells are deposited with a high hydrogen dilution near the edge of amorphous-to-nanocrystalline transition. On the amorphous side, the best nc-Si:H solar cells, however, are deposited near the edge of nanocrystalline-to-amorphous transition, but on the nanocrystalline side. The solar cells deposited under conditions between the two edges is defined as mixed-phase cells with characteristics of dramatic changes in V_{oc} upon changes of hydrogen dilution and a large spatial dispersion of V_{oc} over the substrate. Previously, we reported a large increase in V_{oc} after light soaking of mixed-phase solar cells [9-10]. The amount of the increase depends on the initial V_{oc} and light soaking conditions. A light-induced V_{oc} increase of as large as 150 mV has been observed for a mixed-phase cell. Light soaking under reverse bias and forward current injection experiments suggests that the light-induced V_{oc} increase has the same origin as the Staebler-Wronski effect. We proposed that light-induced crystalline volume fraction or grain size reduction could cause the V_{oc} increase. However, recent studies by Raman Spectroscopy and X-Ray Diffraction found no observable change before and after light soaking within experimental errors. Therefore, it is necessary to investigate if the proposed light-induced crystalline volume fraction change is the only reason for the light-induced V_{oc} increase, or other unknown mechanisms exist.

We developed a model to explain the light-induced V_{oc} increase in mixed-phase solar cells. We first analyzed what determines the initial V_{oc} in a mixed-phase solar cell and then proposed the possible causes of the light-induced V_{oc} increase. The new model is consistent with most of the experimental results. In addition, we carried out experiments with different a-Si:H buffer layers for confirmation of the validity of the model. In order to gain more insight into the light-induced V_{oc} increase, we did kinetics measurements of the mixed-phase solar cells as a function of light-soaking time.

9.2. Two-diode equivalent circuit for mixed-phase solar cells

Before discussing the mechanism of the light-induced V_{oc} increase, we need to understand what determines the initial V_{oc} of a mixed-phase solar cell. We believe that V_{oc} starts to drop only when the fraction of the crystal phase reaches a certain level, resulting in transport paths characteristic of microcrystalline cells. If we neglect lateral transport, a mixed-phase solar cell can be considered as two individual cells connected in parallel. One cell has the characteristics of an a-Si:H cell and the other of a nc-Si:H cell. Since the V_{oc} of nc-Si:H cells is much lower than that of a-Si:H cells, the nc-Si:H cell will have a positive injection current while the a-Si:H cell still has negative photo current under a bias voltage that lies between the V_{oc} of the nc-Si:H cell and the V_{oc} of the a-Si:H cell. The open-circuit condition is reached when the positive current of the nc-Si:H cell and the negative current of the a-Si:H cell have the same magnitude. Since the forward current density is usually very high and increases with bias voltage exponentially, one should expect a very sharp V_{oc} drop when the nanocrystalline silicon path appears. The slope of V_{oc} decreases with respect to the increase of crystalline volume fraction and depends on the quality of the nc-Si:H cell, the forward current density.

Based on this information, we can project the dependence of V_{oc} as a function of crystalline volume fraction if the J-V characteristics of the a-Si:H and nc-Si:H are known. In order to test this hypothesis, we compared the measured J-V characteristics of an a-Si:H solar cell with a good nc-Si:H cell and a poor nc-Si:H cell, as shown in Fig. 40 (upper curve). Considering a mixed-phase cell with a unit area, we multiplied the positive current density data of the nc-Si:H cell with an assumed percentage of crystalline volume fraction and multiplied the current density of the a-Si:H cell with the remaining percentage to obtain the voltage that corresponds to the same current for the nc-Si:H and a-Si:H cells. This voltage is the V_{oc} of the mixed-phase solar cell with the given percentage of the nanocrystalline phase. For voltages that are larger than a certain value, current density data are not available for the nc-Si:H cell due to the limitation of measurement. In this case, we need to use extrapolated data. To obtain this data, we used an exponential extension and a linear extension. Figure 40 (lower curve) shows the estimated results using the good nc-Si:H cell with both exponential and linear extensions, and using the poor nc-Si:H cell with a linear extension. From this plot, one can see that the V_{oc} drops sharply with the increase of crystal volume fraction. The higher the quality of the microcrystalline cell, the faster the increase of the current density with voltage, the steeper the decrease of V_{oc}. Based on this plot, we can explain the increase in V_{oc} as follows. First, the crystal volume fraction might be reduced by light soaking, the same as we proposed before. In this case, the movement will be along the curve on the plot (see Fig. 40). Second, the quality of the nanocrystalline phase is degraded by light soaking, such as an increase of grain boundary recombination. In this case, the forward injection current is not sufficient to compensate for the photocurrent from the amorphous phase under the initial V_{oc}. Therefore, a larger voltage is needed to reach a new open-circuit condition. In the latter case, the movement is along a line perpendicular to the X-axis (see the upward arrow in Fig. 40 (lower)). This process is consistent with the degradation of FF. In mixed-phase solar cells, the two possible processes may coexist at the same time. Although good nc-Si:H solar cells have been reported to exhibit little light-induced degradation, the mixed-phase nc-Si:H cells do degrade. We believe that our model satisfactorily explains the observed light-induced phenomenon.

9.3. Buffer layers in mixed-phase solar cells and their effect on metastability

To test the two-diode equivalent circuit model, a new experiment was conducted. a-Si:H buffer layers of various thicknesses were deposited using RF glow discharge between the *p* and *i* layers of a mixed-phase *n-i-p* silicon solar cell. The samples were deposited on Al/ZnO back reflectors. ITO dots of area 0.05 cm^2 and 0.268 cm^2 (active-area of 0.25 cm^2) were deposited on top of the *p* layer as the top contact. Each substrate contains 40 ITO dots on a 4×4-cm^2 area. The J-V characteristics of the solar cells were measured at their initial and light-soaked states. Light soaking was done under AM1.5 illumination at 25 ºC for 40 hours. Although the cells on one substrate exhibit a large V_{oc} range corresponding to nc-Si:H, mixed-phase, and a-Si:H, due to a non-uniform deposition as shown previously, the reproducibility is quite good, i.e. the cells using the same recipe from different runs but at the same location on the substrate have similar characteristics. Therefore, the difference between cells at the same location but with different buffer layer thicknesses is mainly due to the difference in the buffer layer. Table XXVII lists the initial and light soaked values of the J-V characteristics of three cells with different buffer layer thicknesses but at the same location on the substrate. One can see that the V_{oc} increases from 0.638 V to 0.955 V when the buffer layer thickness is increased from 0-500 Å. It clearly shows

Table XXVII: Initial and light-soaked J-V characteristics of three mixed-phase silicon solar cells with different a-Si:H buffer layers.

Buffer layer thickness (Å)	State	J_{sc} (mA/cm^2)	V_{oc} (V)	FF
0	initial	16.7	0.638	0.518
	degraded	15.2	0.684	0.427
100	initial	16.2	0.722	0.584
	degraded	14.7	0.830	0.479
500	initial	16.0	0.955	0.473
	degraded	15.0	0.924	0.426

the role the buffer layer plays in determining the V_{oc} of the mixed-phase cells. The initial V_{oc} and FF increases even when only a 100 Å buffer layer is deposited, probably due to the reduction of back diffusion, interface recombination, and reduction of shunt current.

In order to understand the effect of the buffer layer on cell performance, dark J-V characteristics were measured at room temperature. Figure 41 shows the dark J-V curves for the three cells listed in Table XXVII. A significant shunt current is observed in the cell with no buffer layer. For the cells with 100 Å and 500 Å thick buffer layers, the buffer layer completely blocked the shunt current, as evidenced by the straight line at $V < 0.5$ V. Therefore, we believe that the increase in the initial V_{oc} from a no-buffer layer to a 100-Å thick buffer layer is mainly due to a reduced shunt current. In addition, the two cells have the same current for $V > 0.5$ V. This result is consistent with the behavior predicted by the two-diode model based on light-soaking results. The cell with the 500 Å buffer layer has a much lower current at $V > 0.5$ V, which means the 500 Å thick buffer layer significantly reduces the forward injection current in the equivalent nc-Si:H diode. As a result, the 500-Å thick buffer layer increases the initial V_{oc} further, but decreases FF significantly, due to a thick barrier for hole collection.

As discussed in the previous section, the light-induced V_{oc} increase could be due to the crystalline volume fraction reduction and forward injection current reduction. Figure 42 compares the dark J-V curves of the cell with the 100-Å thick buffer-layer at the annealed and degraded states, where the symbols are experimental data and the lines are the fittings for the diode characteristic formula. It appears that light soaking increases the current at a low voltage (< 0.5 V), due to an increased reverse saturated current, and increases the diode quality factor from 1.67 to 2.24. However, at a high voltage, light soaking decreases the current, a factor partially responsible for the light-induced V_{oc} increase. Figure 43 shows the light-induced changes in V_{oc} for the cells with the three different buffer-layer thicknesses as a function of initial V_{oc}. The mixed-phase cells with no buffer layer and with a 100-Å thick a-Si:H buffer layer have a bell-shaped curve as previously reported. However, no light-induced V_{oc} increase is observed for the cells with a 500-Å thick a-Si:H layer. Instead, V_{oc} decreases after light soaking, similar to regular a-Si:H cells.

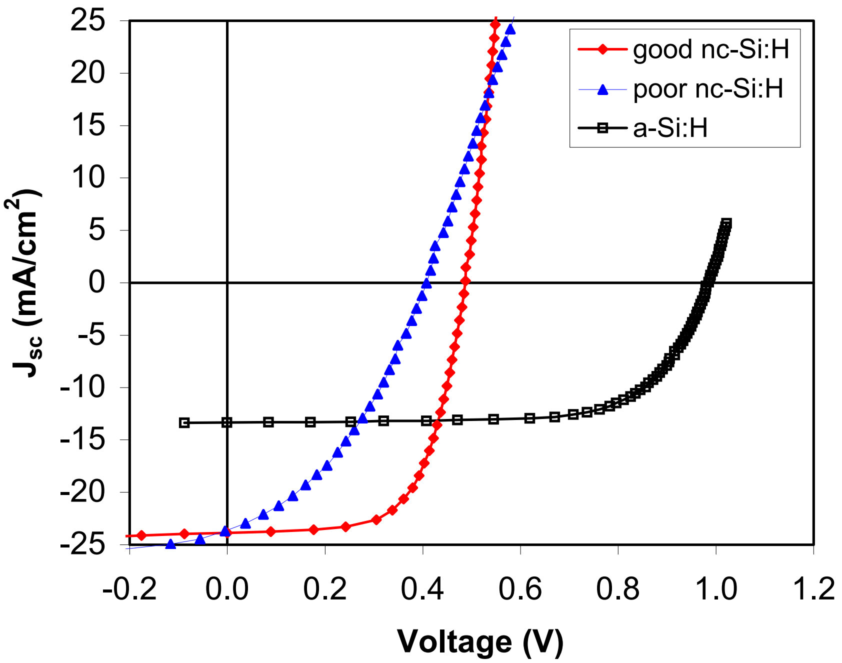

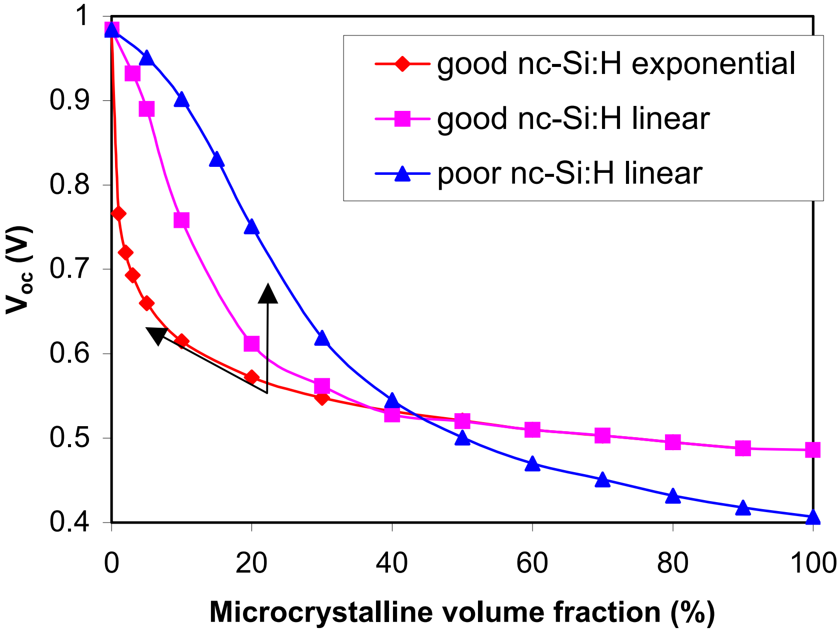

Figure 40. Light J-V characteristics (upper) of an a-Si:H and two nc-Si:H cells, and estimated V_{oc} (lower) as a function of crystal volume fraction in mixed-phase solar cells.

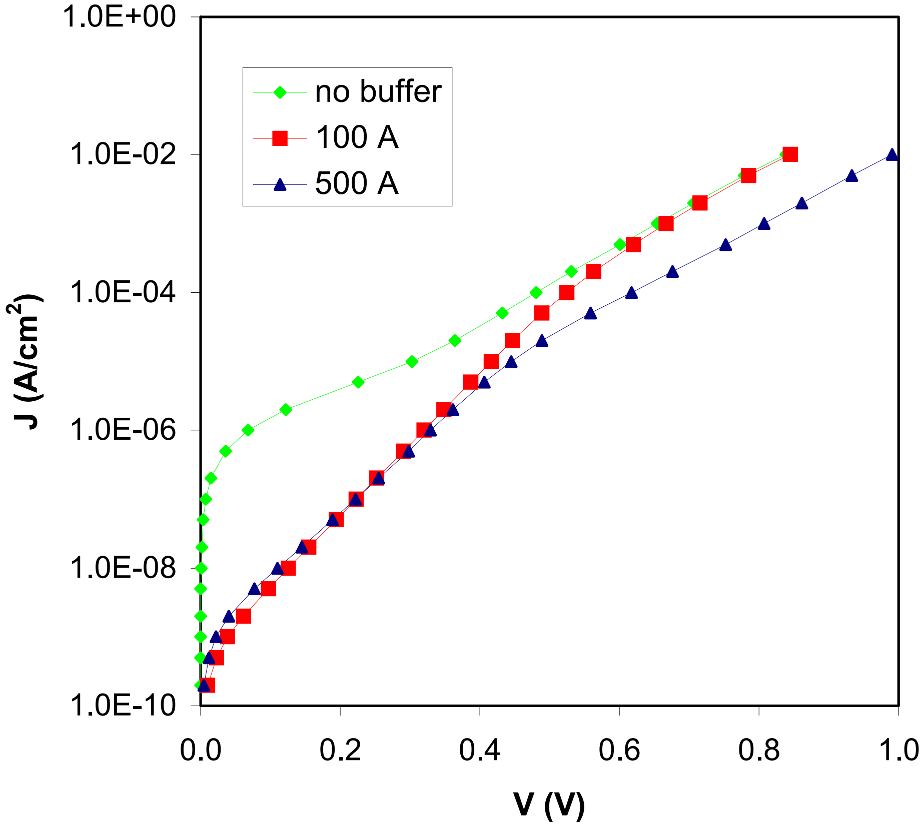

Figure 41. Dark J-V characteristics of the mixed-phase solar cells with different thickness buffer layers.

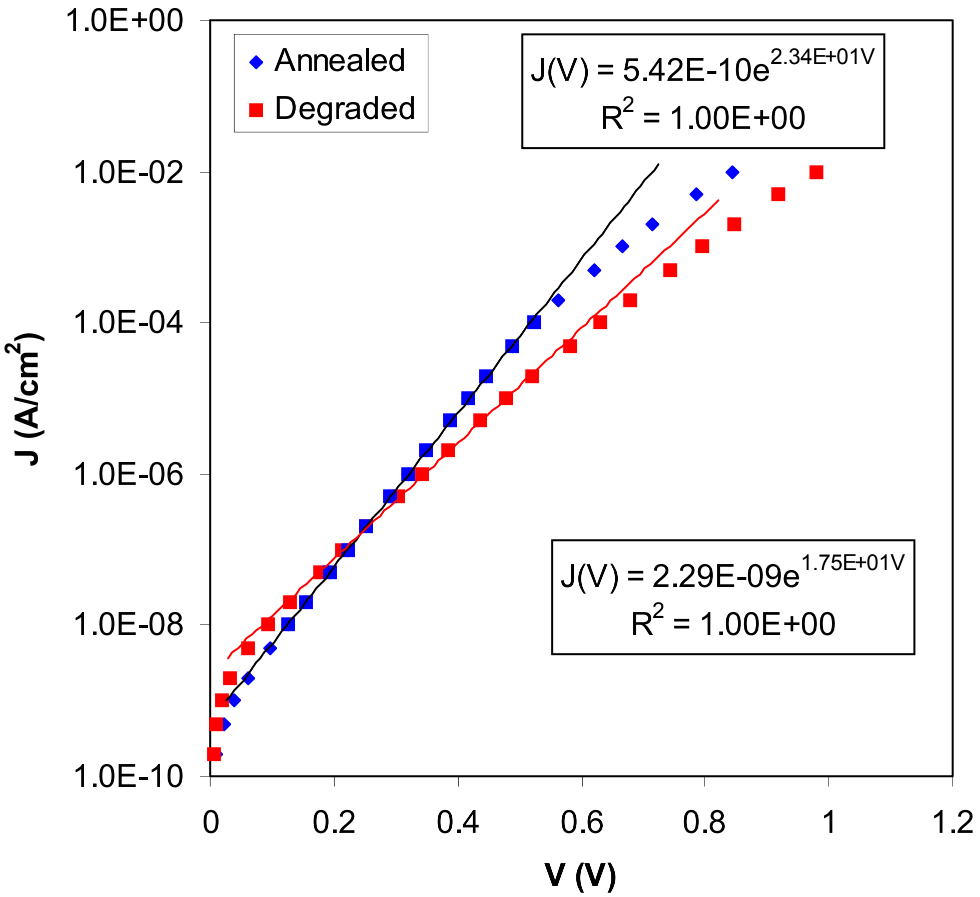

Figure 42. Dark J-V characteristics of a mixed-phase solar cell with 100 nm a-Si:H *i/p* buffer layer at the annealed and degraded states.

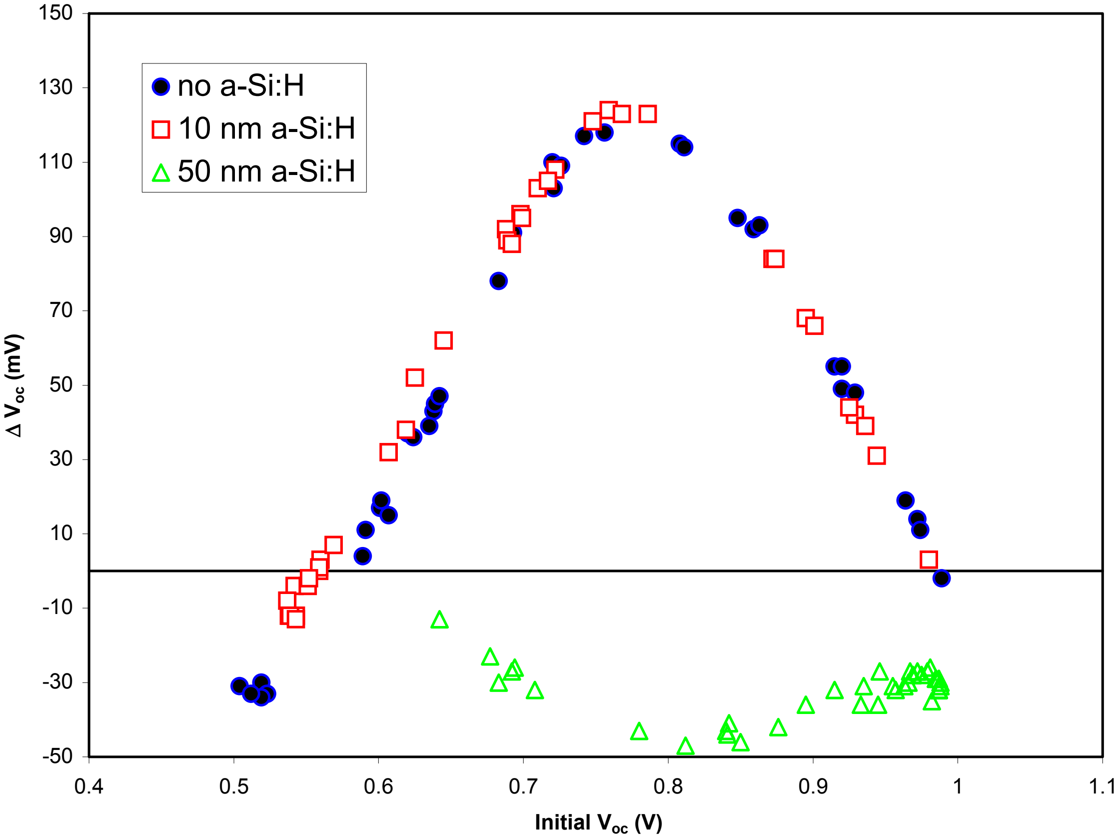

Figure 43. Light-induced V_{oc} change versus initial V_{oc} for cells with different a-Si:H buffer layer thicknesses.

A thick buffer layer between the *p* and *i* layers would reduce the forward current density of nc-Si:H cells significantly by blocking hole injection because of the wider bandgap of a-Si:H compared to nc-Si:H and a large valence band edge discontinuity between a-Si:H and nc-Si:H layers. As discussed above, a low forward current density in the nc-Si:H cell results in a large V_{oc} in a mixed-phase solar cell as shown in Table XXVII. In addition, the forward current density in a nc-Si:H cell with a thick buffer layer is no longer determined by the quality of the intrinsic layer, but instead by the a-Si:H buffer layer. In this case, light-induced changes in the nanocrystalline quality do not lead to an increase in V_{oc} of the mixed-phase silicon solar cell. The similar characteristics of cells with zero Å and 100 Å-thick a-Si:H buffer layers indicate that carriers can tunnel through the thin buffer layer. Similar experiments with a-Si:H buffer layers inserted between the *n* and *i* layers did not show an observable effect on the initial V_{oc} or light-induced behavior. The reason could be that V_{oc} is determined by the dominant junction, namely *i/p* junction, in a-Si:H solar cells. A slight change at the *n/i* interface does not significantly affect V_{oc}.

9.4. Kinetics of light-induced V_{oc} increase in mixed-phase solar cells

The light-induced V_{oc} increase depends on cell deposition and measurement conditions. In principle, the metastable behavior is a transition process between two thermal equilibrium states, one is in the dark (or under ambient condition), and the other is under illumination. The kinetics of the metastable changes provide information not only in the two equilibrium states, but also during the transition process. In order to gain insight into the mechanism of the light-induced V_{oc} increase, we conducted kinetic measurements. J-V characteristics, as a function of light soaking time, were measured at 25 °C under an AM1.5 solar simulator for cells with various initial V_{oc}. To ensure that the measurement for each cell starts from the initial state, a stainless steel plate with a hole was used to cover all other cells while the exposed cell was being measured. The parameters V_{oc}, FF, and J_{sc} were extracted from J-V curves to plot the kinetic curves. All the measurements were computer-controlled.

We first conducted measurements on cells having initial V_{oc} >0.8 V (a-Si:H side). The light-soaking time is about 16 hours (overnight). Figure 44 shows (a) the V_{oc} and (c) FF of the cells with different initial V_{oc} as a function of time. Normalized values of V_{oc} and FF with respect to their initial values are plotted in Figure 44 (b) and (d), respectively. One can see that the V_{oc} ramps up for the cells with V_{oc} < 0.98 V during light-soaking and then saturates. The ramping rate, saturation time, and the amount of increase depend on the initial V_{oc}. For the cell with an initial V_{oc} of 0.86 V, the V_{oc} increases by 100 mV after 16 hours of light soaking, and does not saturate. With increasing the initial V_{oc}, the rate and the magnitude of the increase gets smaller, and the saturation time becomes shorter. In the mixed-phase solar cells, two competing processes exist in the V_{oc} kinetics during light soaking, i.e. decreasing V_{oc} by the Staebler-Wronski effect, and increasing V_{oc}, due to the reduction of nanocrystalline volume fraction and the reduction of forward current in the nanocrystalline region. When these two competing processes are balanced, the V_{oc} should not change. The cell with an initial V_{oc} of 0.98 V has this kind of balanced structure. As indicated in the figure, the V_{oc} is almost flat for the first 3 hours, and then decreases slightly. The V_{oc} of the cell with an initial V_{oc} of 1.011 V continuously decreases during light soaking, a behavior characteristic of conventional a-Si:H solar cells. As shown in Fig. 44 (c), the values of FF for all the cells decrease with time and do not exhibit saturation.

The results of the cells having initial V_{oc} less than 0.8 V (nc-Si:H side) are shown in Fig. 45. The V_{oc} increases with time for cells having an initial $V_{oc} > 0.6$ V, but decreases with time for the cells with an initial $V_{oc} < 0.6$ V. In contrast to the behavior of cells on the a-Si:H side, the rate and the magnitude of the change increases with the increase of V_{oc}. Figure 45 (c) shows the changes in FF with a light-soaking time. Again, FF decreases with a light-soaking time for all the cells. In addition, neither V_{oc} nor FF show saturation.

It is interesting to compare the details about the behavior of the changes of V_{oc} and FF of the two sides. First, we found that the V_{oc} enhancement does not exhibit saturation for cells on the nc-Si:H side but does show saturation for cells on the a-Si:H side. Similarly, FF decreases slower at the amorphous side than at the nc-Si:H side. Secondly, compared to the a-Si:H side, the ramping rate of V_{oc} is smaller at the beginning of light soaking for cells on the nc-Si:H side. For some cells, the V_{oc} does not change after a few tens of minutes. After passing an intersection point that depends on the initial V_{oc}, the ramp rate of the V_{oc} of cells on the nc-Si:H side is faster than on the a-Si:H side.

In order to confirm the above observations, light soaking for a longer time was done on two solar cells. One was selected from the a-Si:H side and the other from the nc-Si side. Figure 46 shows the V_{oc} and FF changes of the two cells with initial V_{oc} values between 0.952 V and 0.590 V over a period of 67 hours of light soak. For the cell with an initial V_{oc} of 0.952 V, the V_{oc} first increases, then appears to saturate, and finally starts to decrease. For the cell with an initial V_{oc} of 0.590 V, the V_{oc} keeps increasing and has no indication of saturation. The FFs of the two cells decrease monotonically with time, but the change for the cell with an initial V_{oc} of 0.952 V is much slower than that with 0.590 V.

In summary, we find that for the cells with an initial $V_{oc} > 0.8$ V, the rate of increase of V_{oc} is higher at the beginning of light soaking than that for the cells with $V_{oc} < 0.8$ V. For longer exposure times, the rate of increase of V_{oc} is lower for cells with an initial $V_{oc} > 0.8$ V than that for cells with $V_{oc} < 0.8$ V. The two sets of curves intersect at a certain exposure time that is determined by the value of the initial V_{oc}. The cells with an initial V_{oc} larger than 0.8 V exhibit saturation after a long time of light soaking. For some cells with an initial V_{oc} in the range 0.95-0.98 V, the V_{oc} shows an initial increase followed by a decrease. For cells with a $V_{oc} < 0.8$ V, the V_{oc} does not exhibit saturation for exposure time up to 1000 minutes. All cells show decreases in FF with exposure time. The cells with a $V_{oc} > 0.8$ V show earlier saturation than those with a $V_{oc} < 0.8$ V.

A similar behavior is observed in the dependence of changes in V_{oc} (ΔV_{oc}) on initial V_{oc} for different light-soaking times. As shown in Fig. 47, ΔV_{oc} increases with light-soaking time for all cells. Also, the position of the peak shifts towards lower initial V_{oc}. The cell with an initial V_{oc} of 0.86 V exhibits the highest change after an exposure time of 5 minutes. The cell with an initial V_{oc} of 0.77 V exhibits the highest change after an exposure time of 40 hours. This phenomenon is indicative of a faster initial V_{oc} increase in the cells with a higher initial V_{oc} than those with a lower initial V_{oc}.

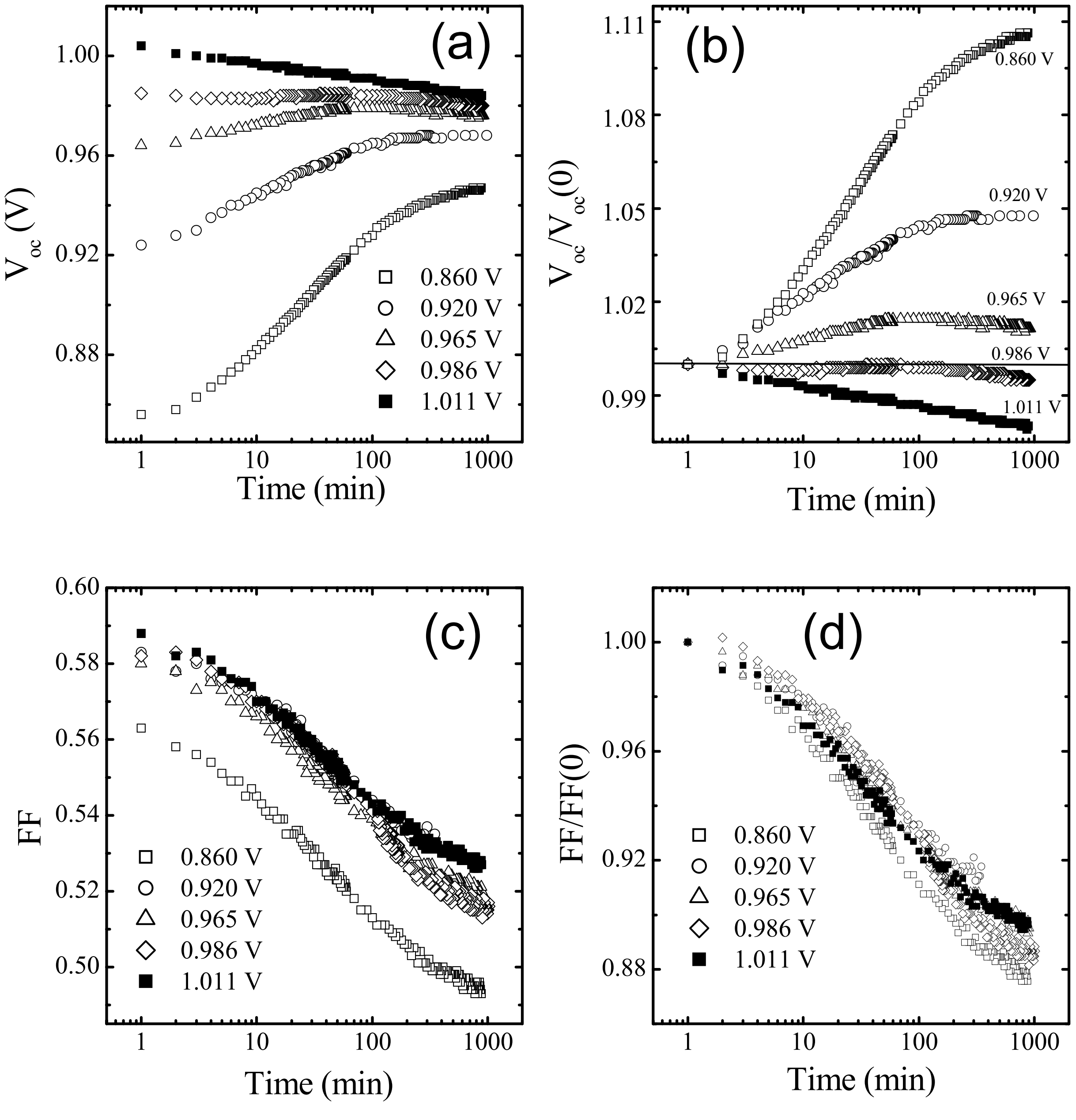

Figure 44. Kinetics of V_{oc} and FF for the cells with various initial V_{oc} on the a-Si:H side: (a) V_{oc}, (b) normalized V_{oc}, (c) FF, and (d) normalized FF.

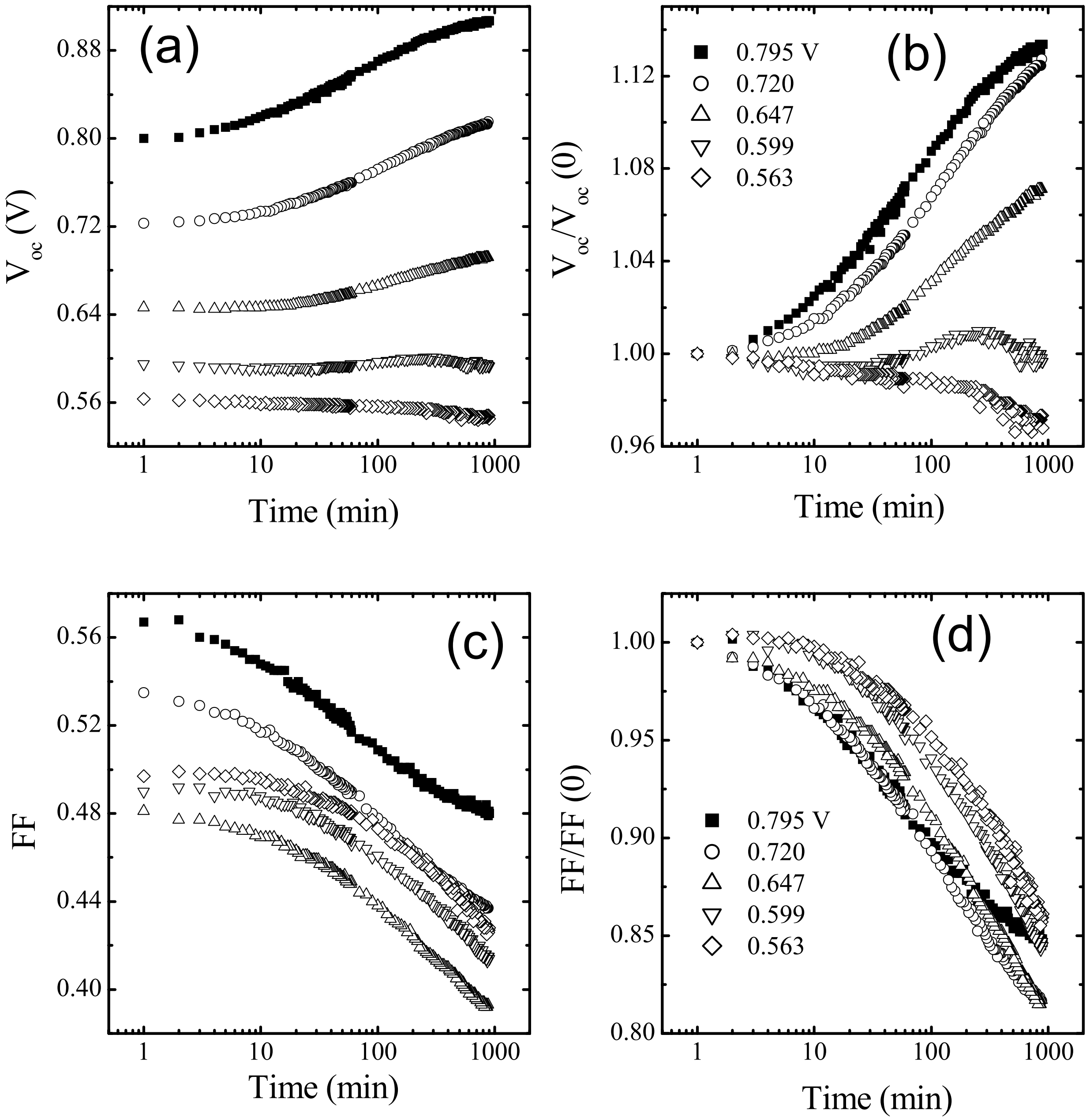

Figure 45. Kinetics of V_{oc} and FF for the cells with various initial V_{oc} on the μc-Si side: (a) V_{oc}, (b) normalized V_{oc}, (c) FF, and (d) normalized FF.

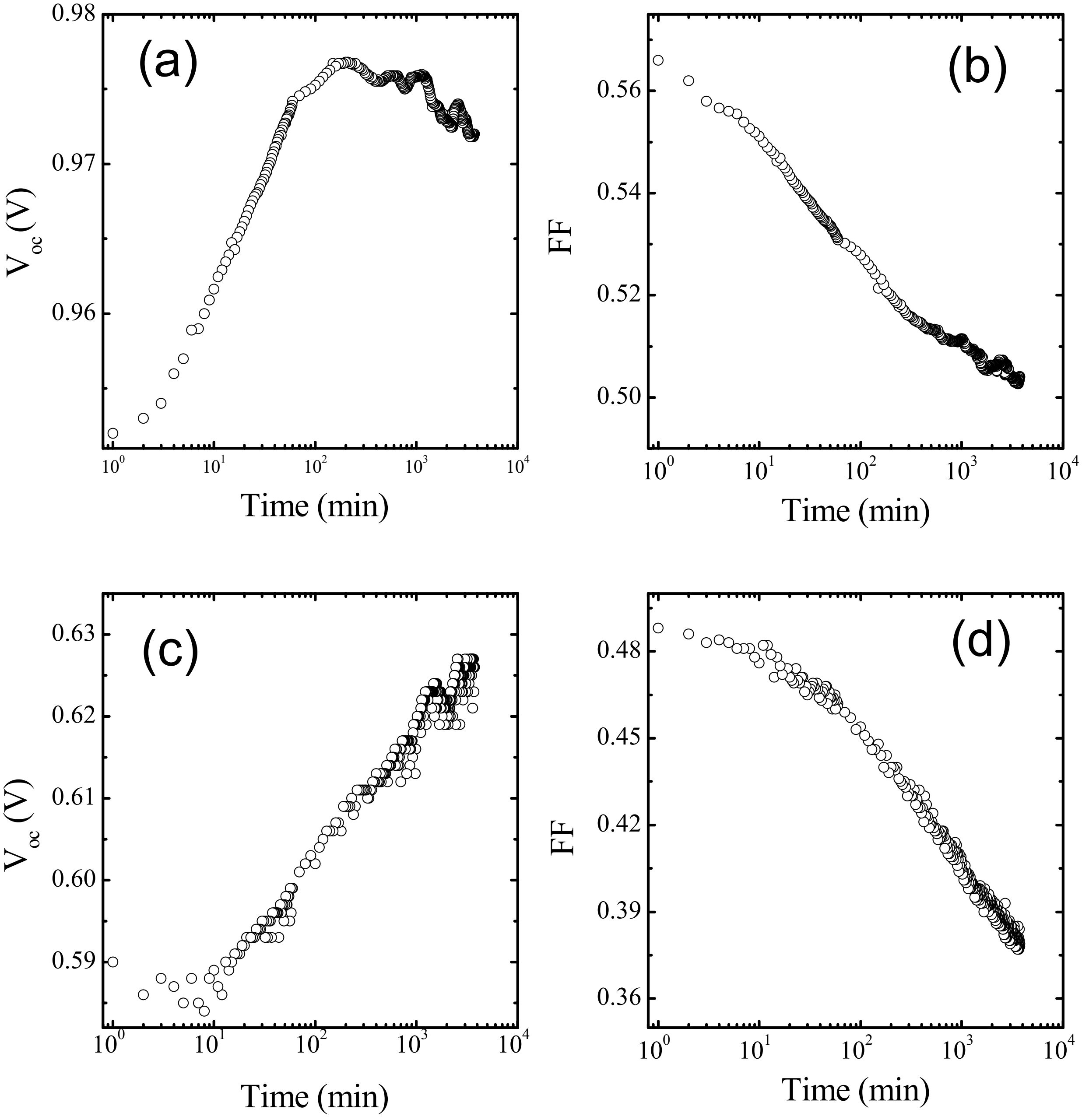

Figure 46. Kinetics of V_{oc} and FF of the cells with an initial V_{oc} of 0.952 V for (a) and (b), and 0.590 V for (c) and (d) for a 67-hour light soaking.

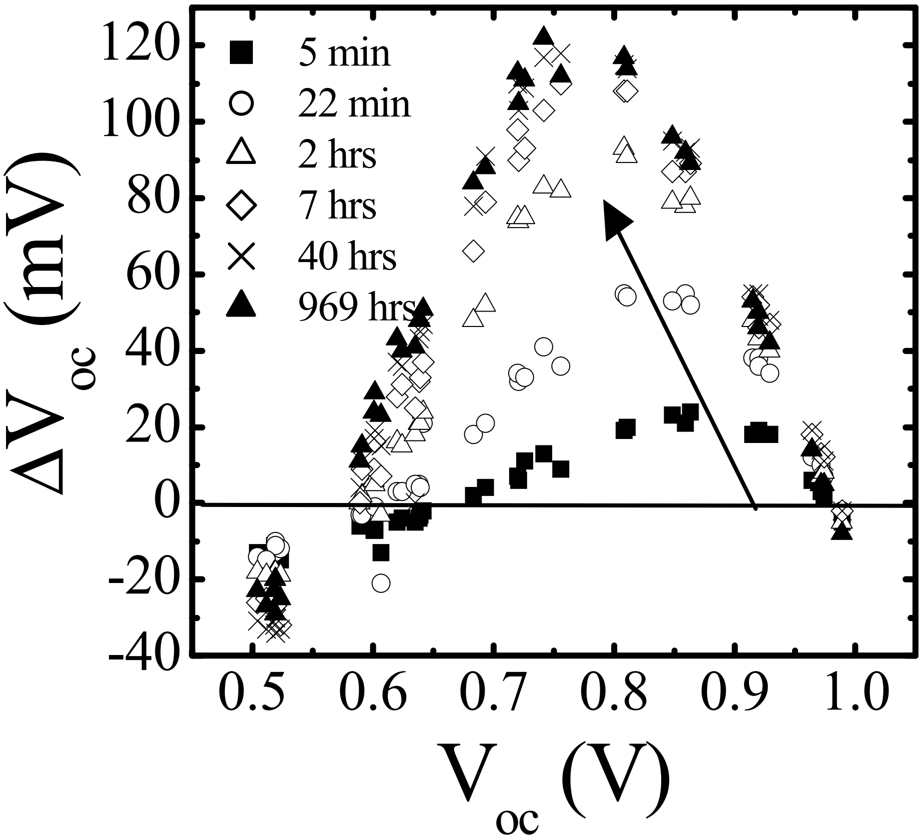

Figure 47. ΔV_{oc} as a function of initial V_{oc} for different exposure times. The arrow indicates the shift in the peak position.

Based on the concept of the two-diode model, most of the kinetic results are understandable. First, the cells with an initial V_{oc} around 0.6 - 0.8 V (depending on the cell structure and the light soaking condition) have a wider spread between the two curves of Fig. 43(b), which means that any change in the crystalline volume fraction or forward current density would produce a large $\triangle V_{oc}$. Experimentally, the largest light-induced V_{oc} increase appears at around 0.75 V with a bell-shaped curve on the $\triangle V_{oc}$ versus the initial V_{oc} plot. Therefore, the increase rate for the cells with intermediate initial V_{oc} is higher than those with smaller or larger initial V_{oc}. In addition, the cells with low initial V_{oc} (~ 0.6 V) would move towards the unstable region, but the cells with high initial V_{oc} would move out of the unstable region. Consequently, on the average, the cells with initial $V_{oc} < 0.8$ V show a smaller increase rate and a slower tendency to saturate than cells with initial $V_{oc} > 0.8$ V, as shown in Figs. 44 and 45. As a result, the maximum on the $\triangle V_{oc}$ versus initial V_{oc} plot shifts to a lower initial V_{oc} as the light soaking time increases (see Fig. 47). The saturation or decrease of V_{oc} after a period of light soaking for the cells with a high initial V_{oc} could be explained as follows. The decrease of forward current for the nc-Si:H cell due to a reduction of forward current density or reduction of crystalline volume fraction is offset by the reduction of current from the a-Si:H, due to the Staebler-Wronski effect that is more pronounced at voltages around 0.85 eV for an a-Si:H cell. We should point out that Fig. 19 is just an illustration. The choices of J-V curves for a-Si:H and nc-Si:H diodes are somewhat arbitrary. In a real mixed-phase cell, the characteristics of the equivalent a-Si:H and nc-Si:H are unknown. Therefore, quantitative predictions of the amount of light-induced V_{oc} increase, and kinetic behavior cannot be made.

Previously, we reported that the origin of the light-induced V_{oc} increase is the same as the Staebler-Wronski effect. Recombination of photo-generated carriers produces metastable defects in both nc-Si:H (may be at grain boundary region) and a-Si:H phases. Therefore, it is not difficult to understand why the FF for all the cells decreases with light-soaking time.

9.5. Summary

Light-induced V_{oc} in mixed-phase solar cells has been systemically studied. A two-diode equivalent circuit model has been proposed to explain the change of initial V_{oc} with increasing microcrystalline volume fraction. The model is consistent with most of the experimental results. A new experiment with different buffers provides additional supporting evidence for the model. We believe that the light-induced crystalline volume fraction change (if any) and the reduction of the forward current in the crystalline region are the two causes of the light-induced V_{oc} increase. At this time, we cannot distinguish which effect makes the main contribution. The kinetics of light-induced V_{oc} in the mixed-phase solar cells have been measured. The kinetics behaviors are different for cells with different initial V_{oc} and also can be explained using the two-diode equivalent circuit model.

Section 10: Metastability of nc-Si:H Solar Cells

10.1. Introduction

The Staebler-Wronski effect has limited the development of a-Si:H-based solar cells. Although a significant amount of work has been carried out in the last 25 years, an effective way has not been developed to eliminate the light-induced degradation in a-Si:H based solar cells. As an alternative material, nc-Si:H has attracted remarkable attention. One advantage of using nc-Si:H in thin-film solar cells is its better stability under prolonged light soaking than a-Si:H and a-SiGe:H alloys. In earlier studies, it was reported that no light-induced degradation was observed in nc-Si:H solar cells. However, the term nc-Si:H represents a wide range of materials comprised of various grain sizes and different microcrystalline volume fractions. The best nc-Si:H solar cells are normally deposited near the transition from nanocrystalline to the amorphous phase, which means a large amount of the amorphous phase still exists in the nc-Si:H materials. Therefore, it would be logical to assume light-induced degradation in nc-Si:H solar cells deposited in this regime. Indeed, Klein and his colleagues found that nc-Si:H solar cells made with a hydrogen dilution close to the transition show light induced degradation. The amount of degradation depends on the dilution ratio, hence, on the crystalline volume fraction and grain size [38]. This result was also confirmed by the Neuchâtel group[39].

In general, nc-Si:H can be considered as a two-phase material with nanocrystallites surrounded by amorphous tissue. The photons with energy higher than the bandgap of a-Si:H are largely absorbed in the amorphous phase while the lower energy photons are absorbed in the grains. Since the material properties inside the grains would be similar to crystalline silicon with no light induced defects, one may expect no light-induced defects generated in nc-Si:H when it is exposed to red light with photon energy lower than the optical bandgap of a-Si:H. If this hypothesis is correct, there would be much less light induced degradation in the nc-Si:H bottom cell in an a-Si:H/nc-Si:H double-junction structure, because the high-energy photons are absorbed in the a-Si:H top cell. During this program, we have studied the spectrum dependence of the light-induced change in the nc-Si:H cell performance. We find that light soaking under a red light with photon energy smaller than the band gap of amorphous silicon produces very little change in the cell performance, while a blue light results in more degradation than a white light.

It has been found that forward current injection in a-Si:H solar cells also causes degradation in the cell performance. It proves that the recombination of the electrons and holes provides the driving force for the defect generation. We have also done the forward current injection experiments on nc-Si:H solar cells and found that no forward current injection induced degradation in nc-Si:H solar cells. We believe that the current path in the nc-Si:H solar cells is through the crystallites, where the recombination does not produce defects, and hence, does not degrade the cell performance.

One surprising experimental observation is that a reverse electrical bias on nc-Si:H solar cells does not reduce the light-induced degradation as it does in the a-Si:H and a-SiGe:H alloy solar cells. Instead, the light-induced degradation in nc-Si:H is significantly increased by a reverse electrical bias. We have proposed a back-to-back connected diode model to explain the reverse bias enhanced light-induced degradation. The light-soaking experiments under various bias and illumination conditions agree with the proposed model. Furthermore, the analyses of J-V measurements under different color filters and quantum efficiency losses provide additional supports for the proposed model.

10.2. Light soaking with different light sources

We have systematically studied the light induced degradation of nc-Si:H single-junction solar cells with various light sources. Two sets of nc-Si:H single-junction solar cells were studied. The cells in each set were from one run of deposition on the same substrate; and therefore, the cell performance is very similar. One set was deposited using MVHF at a high rate with relatively low V_{oc}. The other set was deposited with RF at a low rate with relatively high V_{oc}. We believe that the RF cells have a lower crystalline volume fraction than the MVHF cells. As a comparison, we also studied a set of a-SiGe:H bottom cells. Light soaking was done at 25 °C under open-circuit conditions. An AM1.5 solar simulator was used as the light source. Focus lenses and filters were used to vary the light intensity and the spectrum. The J-V characteristics were measured as a function of light soaking time under the same light used for the light soaking. The light soaking time was 15 hours. The J-V characteristics in the initial state and degraded state, after light soaking, were measured under an AM1.5 illumination and by quantum efficiency measurements. Due to the difference in responses for different wavelengths, we used the same photo-generated carrier density for different light spectra. We have found that for solar cells with a good FF, the J_{sc} is a reasonable measure of the photo-carrier density. Thus, we

Table XXVIII: Summary of the light soaking results for the nc-Si:H single junction solar cells made with MVHF at a high rate. The red light was obtained by a focused white light with a 665 nm long-pass filter, and the blue light with a 650 nm short-pass filter.

Cell No.	State	J_{sc} (mA/cm^2)	V_{oc} (V)	FF	P_{max} (mW/cm^2)	Light source
1	Initial	22.02	0.475	0.624	6.53	White (AM1.5) J_{sc}~22 mA/cm^2
	Light soaked	21.82	0.474	0.608	6.29	
	Degradation	0.91 %	0 %	2.56 %	3.68 %	
2	Initial	21.86	0.481	0.623	6.55	Red light with J_{sc}~22 mA/cm^2
	Light soaked	21.86	0.480	0.623	6.55	
	Degradation	0 %	0 %	0 %	0 %	
3	Initial	22.20	0.474	0.621	6.53	White light with J_{sc}~44 mA/cm^2
	Light soaked	22.00	0.467	0.598	6.14	
	Degradation	0.9 %	1.48 %	3.70 %	5.97 %	
4	Initial	22.19	0.472	0.620	6.49	Red light with J_{sc}~44 mA/cm^2
	Light soaked	22.11	0.473	0.619	6.47	
	Degradation	0.36 %	0 %	0 %	0.31 %	
5	Initial	21.98	0.476	0.621	6.50	Blue light with J_{sc}~44 mA/cm^2
	Light soaked	21.78	0.469	0.591	6.04	
	Degradation	0.91 %	1.47 %	4.83 %	7.08 %	

adjusted the light intensities for different spectra to produce the same initial J_{sc} value. Here, two J_{sc} values were chosen: one is the same as the J_{sc} under AM1.5 illumination, and the other is double the value under AM1.5.

Figure 48 shows a comparison of the normalized maximum power, P_{max}, as a function of the light soaking time for the MVHF nc-Si:H single-junction solar cell and the a-SiGe:H single-junction bottom cell where the red and blue lights were obtained using a 665 nm long-pass filter and a 650 nm short-pass filter. The long-pass filter only allows the photons with energy lower than 1.86 eV and smaller than the optical bandgap of a-Si:H to pass through and illuminate the sample. For the nc-Si:H cell, the light intensities were adjusted to produce a J_{sc}~44 mA/cm^2, approximately twice the J_{sc} under AM1.5 illumination, for the white, red, and blue lights. For the a-SiGe:H cell, the light intensities were adjusted to produce a J_{sc}~46 mA/cm^2 with the same consideration. The figure clearly shows that there is no detectable light-induced degradation for the nc-Si:H cell under the red light, some degradation under the white light, and more degradation under the blue light.

Table XXVIII shows a comparison of the initial and degraded performance for five MVHF deposited nc-Si:H cells. The first two cells were light-soaked under light intensities that produced the same J_{sc} as under AM1.5. Cell 1 and Cell 2 were under the white light and the red light, respectively. Notice that no light induced degradation was found in Cell 2 under the red light, but it was 3.7% under the white light. To enhance the light soaking effect, we increased the light intensities to produce 44 mA/cm^2, which is twice the J_{sc} under AM1.5 illumination. There is still no detectable degradation under the red light within the experimental errors.

As discussed above, the undetectable light induced degradation under the red light is due to very little absorption in the amorphous phase, while the absorption in the nanocrystalline phase does not produce defects. Two mechanisms could explain the difference between the white and blue light soaking. First, the blue light has a large portion absorbed in the amorphous phase, which produces more defects. For the white light, the portion of red light is mainly absorbed in the nanocrystalline phase and does not produce degradation. Second, more blue light is absorbed nearer the *i/p* interface than in the bulk. Guha *et al.* showed that the *i/p* junction is the dominant junction, and any changes in the dominant junction can cause noticeable changes in the cell performance [40].

Table XXIX lists the J-V characteristics at the initial and degraded states for three RF deposited solar cells. The general trend is the same as the MVHF deposited cells, i.e., the red light produces low degradation, the white light some degradation, and the blue light more degradation. However, unlike the MVHF cell, this cell still has 2.2% degradation under the red light. We believe that the difference could be caused by the different material structure. For the RF-deposited cells, the V_{oc} is larger than the MVHF-deposited cells, which could indicate that there are more amorphous components in the RF cells than in the MVHF cells. This may partially play a role in the light-induced degradation. Although the cut-on filter, with a wavelength longer than 665 nm blocks, has most of the high-energy photons, there are still some photons absorbed by the amorphous tissue, which degrades the cell performance.

Table XXIX: Summary of the light soaking results for the nc-Si:H single junction solar cells made with RF at a low rate. These cells have a high V_{oc} and probably a high amorphous component in the intrinsic layer. The red light was a focused white light with a 665 nm long-pass filter, and the blue light with a 650 nm short-pass filter.

Cell No.	State	Q (mA/cm^2)	V_{oc} (V)	FF	P_{max} (mW/cm^2)	Light source
1	Initial	24.43	0.525	0.596	7.64	White light with J_{sc}~48 mA/cm^2
	Light soaked	23.86	0.521	0.578	7.51	
	Degradation	1.80 %	0.76 %	3.02 %	5.89 %	
2	Initial	24.42	0.526	0.598	7.68	Red light with J_{sc}~48 mA/cm^2
	Light soaked	24.22	0.523	0.593	7.51	
	Degradation	0.82 %	0.57 %	0.84 %	2.20 %	
3	Initial	24.28	0.525	0.605	7.71	Blue light with J_{sc}~48 mA/cm^2
	Light soaked	23.80	0.521	0.580	7.19	
	Degradation	1.98 %	4.83 %	5.77 %	7.23 %	

Table XXX summarizes the results of the a-SiGe:H bottom cells. For the a-SiGe:H cells, the material is homogeneous, and only one optical bandgap is defined with a value around 1.4 eV. The differences among the light soaked samples under the lights with the three spectra are mainly due to the second mechanism (dominant junction effect) discussed above. Overall, the light-induced degradation in the nc-Si:H cell is much less than that in the a-SiGe:H cell even under white and blue light sources. We need to point out that the light-soaked state is not a stabilized state since only a 15-hour light soaking was performed.

Table XXX: Summary of the light soaking results for the a-SiGe:H bottom single-junction solar cells. The red light was a focused white light with a 665 nm long-pass filter, and the blue light with a 650 nm short-pass filter.

Cell No.	State	J_{sc} (mA/cm^2)	V_{oc} (V)	FF	P_{max} (mW/cm^2)	Light source
1	Initial	23.40	0.624	0.575	8.40	White light with J_{sc}~23 mA/cm^2 (AM 1.5)
	Light soaked	22.94	0.608	0.563	7.85	
	Degradation	1.97%	2.56%	2.09%	6.55%	
2	Initial	23.10	0.628	0.601	8.72	White light with J_{sc}~46 mA/cm^2
	Light soaked	22.88	0.601	0.567	7.80	
	Degradation	0.95 %	4.30 %	5.66 %	10.55 %	
3	Initial	23.91	0.614	0.587	8.62	Red light with J_{sc}~46 mA/cm^2
	Light soaked	23.48	0.601	0.563	7.94	
	Degradation	1.80 %	2.12 %	4.09 %	7.89 %	
4	Initial	23.50	0.621	0.572	8.35	Blue light with J_{sc}~46 mA/cm^2
	Light soaked	22.91	0.591	0.539	7.30	
	Degradation	2.51 %	4.83 %	5.77 %	12.57 %	

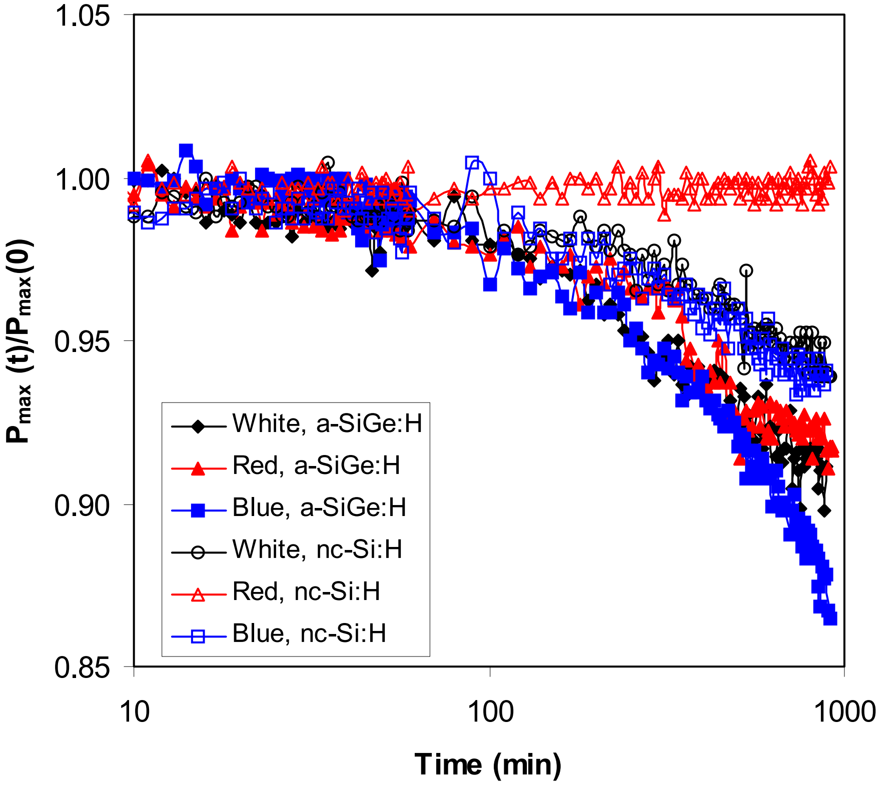

Figure 48. Light-soaking kinetics of normalized efficiency of a nc-Si:H single-junction solar cell and an a-SiGe:H single-junction solar cell.

The above experiment confirms none or very little light-induced degradation for nc-Si:H solar cells under the red light with a photon energy lower than the bandgap of a-Si:H. In an a-Si:H/nc-Si:H double-junction solar cell, most of the blue light is absorbed by the a-Si:H top cell, and the nc-Si:H bottom cell only absorbs the red light with a low photon energy. Therefore, there is very little light-induced degradation in the nc-Si:H bottom cell in multi-junction structures; and a bottom-cell, limited-current mismatching is desirable for stable efficiency, as shown above and in the previous reports.

In summary, we have systematically studied the light-induced degradation in nc-Si:H single-junction solar cells under various light soaking conditions. We found no detectable degradation under a red light with photon energies less than the bandgap of a-Si:H. We believe that the low energy photons are only absorbed in the nanocrystalline phase where no light-induced defect generation occurs. Under white and blue lights, the defect generation in the amorphous phase causes certain degradation. The fact that a larger degradation is observed under a blue light than a white light is due to more absorption in the amorphous phase and more absorption near the *i/p* interface under a blue light than under a white light. These results provide an explanation that a bottom-cell, limited-current mismatch in multi-junction structures with nc-Si:H as the bottom cell leads to a high stable efficiency.

10.3. Forward-current injection in nc-Si:H solar cells

Metastable degradation in a-Si:H solar cells can also occur when the cells are subjected to prolonged forward bias. In this case, double-carrier injection from the doped layers causes carrier recombination in the intrinsic layer, which in turn creates metastable defects. Similar forward-injection experiments have been performed on the nc-Si:H solar cells. As a reference, a-Si:H and a-SiGe:H alloy solar cells were also included in the experiments. Single-junction 1-μm thick nc-Si:H and 0.2-μm thick a-Si:H *n-i-p* solar cells were deposited on 4 cm × 4 cm Ag/ZnO back reflector (BR) coated stainless steel (SS) substrates and specular SS substrates, respectively. The intrinsic layers were deposited using a modified very-high frequency glow discharge method at deposition rates of ~ 3-8 Å/s. The forward double-carrier injection experiment was carried out in the dark at room temperature. The samples were annealed in a vacuum at 150 ^{o}C for 2 hours before and after light/current soaking.

To check whether a forward double-injection causes degradation in the nc-Si:H solar cells, we applied a 1-V forward bias to the a-Si:H and nc-Si:H cells in the dark at room temperature. The initial forward current density was about 60 mA/cm^2 for the nc-Si:H cell and 3 mA/cm^2 for the a-Si:H cell. The temperature of the samples was monitored using a thermocouple on the sample surface. No noticeable temperature increase was observed during the forward current injection. The kinetics of the FF under the forward bias are plotted in Fig. 49. One can see that the FF of the a-Si:H cell degrades continuously during the experiment time. This is simply due to new defects generated by the recombination of excess carriers injected by the applied forward bias, which deteriorate the cell performance. On the other hand, the nc-Si:H cell shows no degradation in the FF, although the forward current density was much higher than in the a-Si:H cell. One might suspect that thermal annealing, caused by the high-current density, may have occurred in the nc-Si:H cell. Therefore, we performed another experiment with an a-

SiGe:H bottom cell. The forward-injected current density at 1 V for this cell is around 72 mA/cm^2, which is higher than that of a nc-Si:H cell, but we found a significant degradation in FF, as shown in Fig. 49. In addition, the temperature of the samples was monitored using a thermocouple on the sample surface. No noticeable temperature increase was observed during the forward current injection. This experiment has been carried out for different nc-Si:H cells and under different bias conditions. The result is reproducible. Table XXXI summarizes the data of V_{oc} and FF for one a-Si:H cell, one a-SiGe:H cell, and three nc-Si:H cells. For the a-Si:H cell, V_{oc} decreased by 20 mV and FF by 4.6% for a 1 V forward bias after 20 hours of current soaking, even though the forward-current density was only 3 mA/cm^2. On the other hand, for the nc-Si:H cells, no current induced degradation was observed in either V_{oc} or FF for all three cells with one cell (Cell 5) having been subjected to a 57-mA/cm^2 forward-current injection for more than 60 hours. For the a-SiGe:H cell, the injected current density is also high, ~ 72 mA/cm^2, but it causes a degradation of 26 mV in V_{oc} and 6.5% in FF after 20 hours of current soaking. Based on the experiments above, it can be concluded that the nc-Si:H cells do not have current-induced degradation.

Table XXXI. Behavior of V_{oc} and FF for an a-Si:H (Cell 1), an a-SiGe:H (Cell 2), and three nc-Si:H cells (Cells 3-5) under various forward bias conditions in the dark.

Sample	State	V_{oc} (V)	ΔV_{oc} (mV)	FF	$\Delta FF/FF_{in.}$ (%)
a-Si:H	Initial	0.998		0.696	
Cell 1	20 hr, 1V, 3 mA/cm^2	0.978	-20	0.664	-4.6
a-SiGe:H	Initial	0.623		0.638	
Cell 2	20 hr, 1V, 72 mA/cm^2	0.597	-26	0.596	-6.5
nc-Si:H	Initial	0.469		0.575	
Cell 3	15 hr, 0.5V, 7 mA/cm^2	0.469	0	0.579	+0.7
	Initial	0.469		0.591	
Cell 4	15 hr, 1V, 58 mA/cm^2	0.470	1	0.588	-0.5
	Initial	0.472		0.587	
Cell 5	64 hr, 1V, 57 mA/cm^2	0.474	2	0.590	+0.5

10.4. Enhancement of light-induced degradation under reverse bias

For a-Si:H and a-SiGe:H alloy solar cells, a reverse electrical bias during light soaking reduces the recombination probability of the electron-hole pairs; and hence, reduces the light-induced degradation in the cell performance. During the program, we also studied the effect of electrical bias on the light-induced degradation in nc-Si:H solar cells. As a reference, a-Si:H solar cells were included. For each experiment, two cells having similar initial J-V characteristics on the same substrate were selected for light soaking simultaneously. One cell served as a reference that is light soaked under the open-circuit condition. A reverse bias was applied to the other cell during light soaking. We first confirmed that the two cells on the same substrate showed the same degradation after light soaking under the same conditions. Thus, any difference in the degradation magnitude for the two cells can be attributed to the effect of the applied bias. This experiment was repeated many times, and the results are reproducible.

Typical results are listed in Table XXXII. One notes that for the a-Si:H cell under open-circuit conditions (Cell 1), 69 hours of light soaking causes a decrease of 30 mV in V_{oc} and 8.6% in FF. For the cell under a 2-V reverse bias (Cell 2), there are no light-induced changes within the measurement uncertainty. The reduced/eliminated light-induced degradation by a reverse bias in the a-Si:H cell is commonly explained by the reduced recombination rate, due to the enhancement of the internal electric field, which separates the electron-hole pairs more effectively. In contrast, the reverse bias effect on the light-induced degradation in the nc-Si:H cells is quite different from that in the a-Si:H cell. As shown in Table XXXII, the V_{oc} of the biased cell (cell 4) decreased by 49 mV after 63 hours of light soaking, while that of the cell under open-circuit conditions (cell 3) decreased by only 9 mV. Similarly, the FF shows more degradation in the cell with applied reverse bias (12%) than under the open-circuit condition (5.4%). Apparently, a reverse bias in the nc-Si:H cell does not reduce but enhances the light-induced degradation.

Table XXXII: V_{oc} and FF values for the a-Si:H (Cells 1 and 2) and nc-Si:H (Cells 3 and 4) cells before and after AM1.5 light soaking at 25 ^{o}C with and without a –2 V bias.

Sample	State	V_{oc} (V)	ΔV (mV)	FF	$\Delta FF/FF_{in.}$ (%)
a-Si:H	Initial	0.984		0.695	
Cell 1	69 hr, no bias	0.954	-30	0.635	-8.6
	Initial	0.985		0.704	
Cell 2	69 hr, -2 V	0.983	-2	0.708	+0.6
nc-Si:H	Initial	0.476		0.591	
Cell 3	63 hr, no bias	0.467	-9	0.559	-5.4
	Initial	0.476		0.594	
Cell 4	63 hr, -2 V	0.427	-49	0.523	-12.0

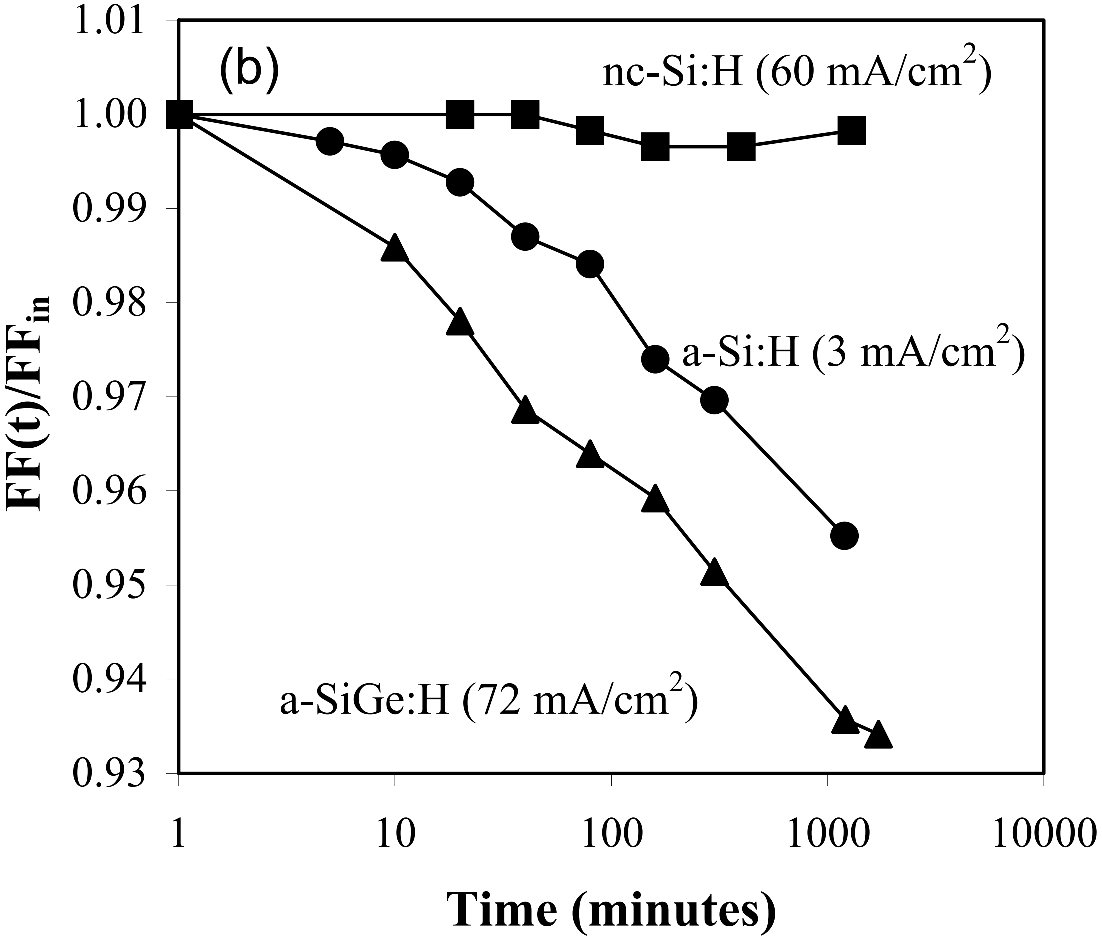

Figure 49. FF as a function of time, FF(t), normalized to the initial FF (FF$_{in}$) for a-Si:H, SiGe:H, and nc-Si:H single-junction solar cells with applied forward bias in the dark. The applied voltage and initially injected current densities are indicated.

Table XXXIII: J-V characteristics of the initial (In.) and degraded (Deg.) nc-Si:H solar cells. The light soaking was done under one sun white light with various bias conditions of –1 V, short circuit, open circuit, and +1 V at 50 °C.

Cell No.	Bias (V)	Status	V_{oc} (V)	ΔV_{oc} (mV)	FF	$\Delta FF/FF_{in}$ (%)	FF_b	$\Delta FF_b/FF_{bin}$ (%)	FF_r	$\Delta FF_r/FF_{rin}$ (%)
1	-1 V	In.	0.479		0.634		0.663		0.664	
		Deg.	0.464	-15	0.563	-11.2	0.624	-5.9	0.579	-12.8
2		In.	0.479		0.633		0.659		0.664	
		Deg.	0.464	-15	0.566	-10.6	0.624	-5.3	0.580	-12.7
3	Short circuit	In.	0.483		0.618		0.664		0.660	
		Deg.	0.472	-9	0.580	-6.1	0.636	-4.2	0.617	-6.5
4		In.	0.480		0.631		0.663		0.663	
		Deg.	0.474	-6	0.574	-9.0	0.638	-3.8	0.599	-9.7
5	Open circuit	In.	0.477		0.622		0.650		0.653	
		Deg.	0.470	-7	0.600	-3.5	0.617	-5.1	0.622	-4.7
6		In.	0.478		0.628		0.655		0.655	
		Deg.	0.470	-8	0.603	-4.0	0.618	-5.6	0.622	-5.0
7	+1 V	In.	0.482		0.608		0.655		0.655	
		Deg.	0.467	-15	0.587	-3.5	0.607	-7.3	0.621	-5.2
8		In.	0.478		0.629		0.656		0.651	
		Deg.	0.465	-13	0.604	-4.0	0.612	-6.7	0.624	-4.1

As shown above, a reverse electrical bias causes significant enhancement of the light-induced degradation in the nc-Si:H solar cells. Therefore, it is very interesting to investigate the dependence of degradation on the magnitude of the applied bias. We selected solar cells from the same substrate with a very good uniformity of the cell performance, and light soaked the cells simultaneously under 100 mW/cm^2 of white light at 50 °C under various bias conditions of –1 V, short circuit, open circuit, and +1 V. To check the reproducibility of the degradation rate, we included two cells at each bias condition. Table XXXIII summarizes the J-V characteristics of the initial and degraded state reached after 309 hours of light soaking. The values of FF under blue and red light illumination, FF_b and FF_r, were measured using narrow band-pass filters centered at 390 nm and 670 nm, respectively, at low light intensities. One can see that the cells with the same bias condition have similar degradation rates. The light-induced degradation of the FF under AM1.5 illumination as a function of the applied bias is plotted in Fig. 50 (a), where the short circuit condition corresponds to 0 V bias, and the open circuit is considered to be a forward bias with a bias value of V_{oc}, which is around 0.48 V. It clearly shows that the light-induced degradation increased with the increase of the magnitude of reverse bias. The FF degraded on average by 10.9% under the reverse bias condition of 1 V, 7.6% under short-circuit conditions, 3.8% under open circuit conditions, and 3.8% under 1 V of forward bias.

Figure 50 (b) shows the degradation in FF_b and FF_r as well as their ratio as a function of the applied bias. Normally, for a uniform one-phase material, FF_b is a measure of the properties near the *i/p* interface since the blue light is mainly absorbed in this region. Moreover, since the holes have a very short distance to traverse under blue light illumination, FF_b is also determined by electron transport. FF_r is a measure of hole transport in the bulk of the material since the red light is more uniformly absorbed. However, in nc-Si:H solar cells, the FF_b and FF_r are not only affected by the properties of the material in different regions of the intrinsic layer, but also by the heterogeneity of the material in the intrinsic layer. This is because higher energy photons (blue light) are mainly absorbed in the amorphous phase, while the lower energy photons (red light) in the crystalline phase. One notes that the bias dependence of FF_r degradation is similar to that of FF degradation measured under AM1.5 illumination, as shown in Fig. 50 (a). However, under the reverse bias and short circuit conditions, the FF_r has more degradation than the FF_b, whereas the FF_b has more degradation under the forward bias. The change of the ratio of FF_b to FF_r has a monotonic increase as the applied bias increases from negative to positive.

Banerjee *et al.* [41]used a quantum efficiency loss technique to study a-Si:H and a-SiGe:H alloy cells with different intrinsic layers and *p/i* interfaces, and identified the carrier collection losses at the *p/i* interface and the bulk of the *i* layers. We used the same technique to investigate light-induced degradation of nc-Si:H cells. The quantum efficiencies of the solar cells under short-circuit conditions, (Q(0 V)), and under reverse bias of 1-V, (Q(-1 V*)*), were measured; and the quantum efficiency loss (Q_{loss}) was defined as the ratio of Q(-1 V) to Q(0 V). Usually, the Q_{loss} values at 390 and 670 nm have correlations with the values of FF_b and FF_r, respectively. High values of FF_b and FF_r are associated with low values of Q_{loss} at 390 and 670 nm, and vice versa. Figure 51 shows the Q_{loss} as a function of the wavelength for two cells. One cell was light soaked under a reverse bias condition, and the other under an open-circuit condition. For their initial states, the Q_{loss} spectra are the same indicating that the two cells have a similar carrier collection. After light soaking, the two Q_{loss} curves became significantly different. The cell under the reverse bias condition shows much higher Q_{loss} than the cell under an open-circuit condition in the long wavelength region, and lower Q_{loss} in the short wavelength region. The result is consistent with the FF_b and FF_r measurements shown in Fig. 50 (b).

As mentioned above, we have carried out the light-soaking experiment on nc-Si:H solar cells with different light spectra under open-circuit conditions. We found that illumination on nc-Si:H solar cells using a red light with photon energies lower than the bandgap of a-Si:H did not result in any degradation in the cell performance, whereas both blue and white light illumination cause degradation, with the blue light degradation slightly larger than the white light. Since the red light is only weakly absorbed in the amorphous phase but is readily absorbed in the nanocrystalline grains, we concluded that the light-induced defect generation in the amorphous phase is responsible for the light-induced degradation. In the following experiment, we investigate the behavior of the reverse bias enhanced degradation in nc-Si:H cells under different light spectra. Again, the red light was obtained using white light with a 665 nm cut-on filter, and the blue light with a 650 nm cut-off filter. During the light soaking, the blue and red light intensities were adjusted using a lens to produce the same J_{sc} as that under 100 mW/cm^2 of white light. The applied bias was –1.5 V, and the light-soaking time was 309 hours. The experimental results are listed in Table XXXIV. One can see that after soaking a under red light, the solar cell does not degrade, which is the same as the result of light soaking under open-circuit conditions. Under a blue light, the V_{oc} degrades by 30 mV and FF by 7.9% compared to 67 mV degradation in V_{oc} and 10.2% in FF under a white light. Clearly, the white light causes

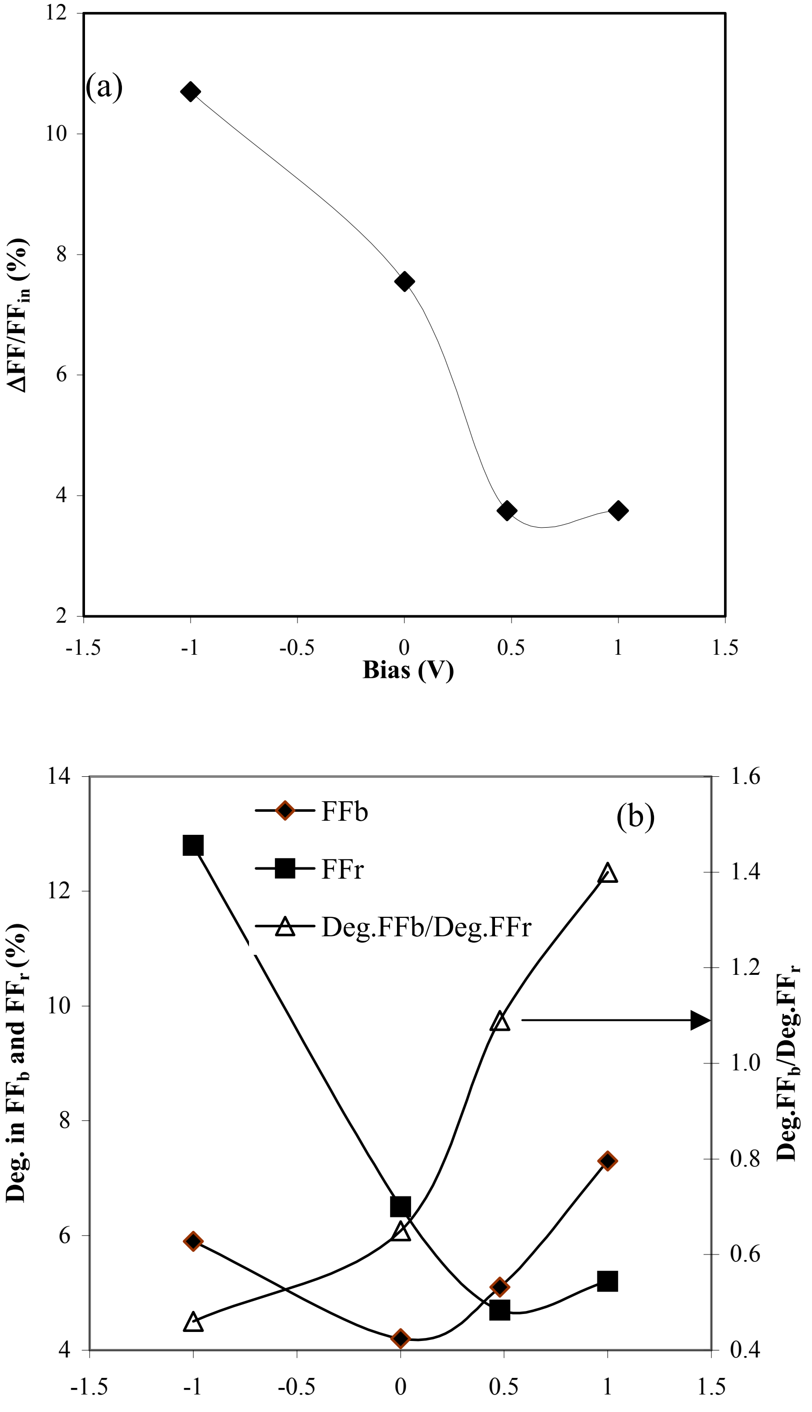

Figure 50. (a) Light-induced degradation in FF and (b) FF_b, FF_r of nc-Si:H solar cells versus the electrical bias during light soaking where ΔFF denotes the variations in FF. Light soaking was carried out at 50 ^oC under one-sun, white-light illumination for 309 hours.

more degradation than a blue light under the reverse bias, which is different from that under open-circuit conditions.

As previously reported, the reverse bias enhanced light-induced degradation in the nc-Si:H solar cells can be annealed away at high temperatures, indicating a metastable defect generation similar to the Staebler-Wronski effect in a-Si:H. Although there is no observable room-temperature recovery of the reverse bias enhanced light-induced degradation in the nc-Si:H cells in the dark, it can be partially recovered by subsequent light soaking under open-circuit conditions, as shown in Fig. 52. In this experiment, two nc-Si:H solar cells from the same substrate were selected for exposure to 100 mW/cm^2 of white light at 50 ºC. One cell (referred to as Cell 1) was light soaked under open-circuit conditions throughout the whole procedure. The other cell (Cell 2) was light-soaked under 2 V of reverse bias for 300 hours, the reverse bias was removed, and the cell was subjected to the same light-soaking conditions as Cell 1 for the rest of the experiment. We find that for Cell 2, during the first 300 hours of light soaking, the reverse bias caused a larger degradation in both FF and V_{oc}. The V_{oc} degrades by 16 mV and FF by 11.1% in Cell 2, as compared to the change of 7 mV and 3.6% in Cell 1 that was degraded under open-circuit conditions. With the reverse bias being removed, the degradation in Cell 2 was partially recovered; and Cell 1 continued to degrade. Eventually, the two cells reached the same performance. This phenomenon is very similar to the light-soaking experiments under an initial higher light intensity and followed by a lower light intensity for a-Si:H solar cells. An enhanced degradation in the cell performance by a higher intensity light recovers, after a subsequent lower intensity illumination, to the same value as obtained by a continuous lower intensity illumination.

Table XXXIV: J-V characteristics of the nc-Si:H single junction solar cells before (In.) and after (Deg.) light soaking with a reverse bias of –1.5 V at different light spectra. The light soaking was carried out at 50 ºC for 309 hours. The intensities of the red, blue, and white lights were adjusted to produce the same short circuit current in the cells.

Cell No.	Light-soaking Conditions	Status	V_{oc} (V)	ΔV_{oc} (mV)	FF	$\Delta FF/FF_{in.}$ (%)
1	Red light	In.	0.472		0.593	
	-1.5 V	Deg.	0.472	0	0.598	+0.8
2	Blue light	In.	0.468		0.585	
	-1.5 V	Deg.	0.438	-30	0.539	-7.9
3	White light	In.	0.472		0.587	
	-1.5 V	Deg.	0.405	-67	0.527	-10.2

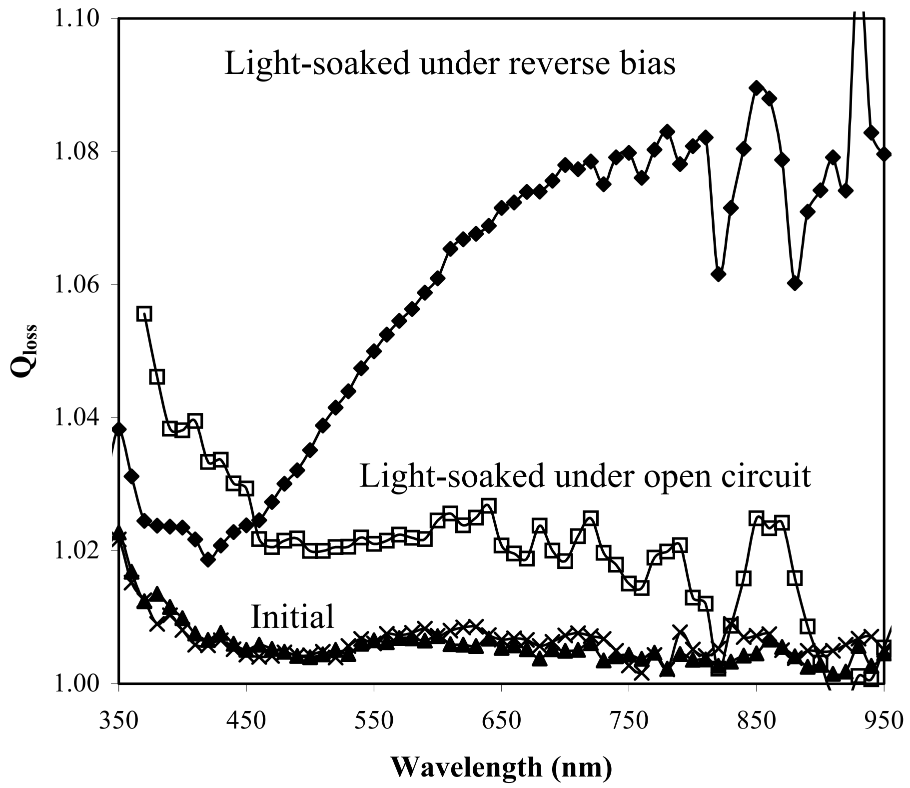

Figure 51. Q_{loss} spectra of nc-Si:H cells before and after light soaking with and without reverse bias. Q_{loss} is defined as the ratio of the biased to the short circuit quantum efficiency.

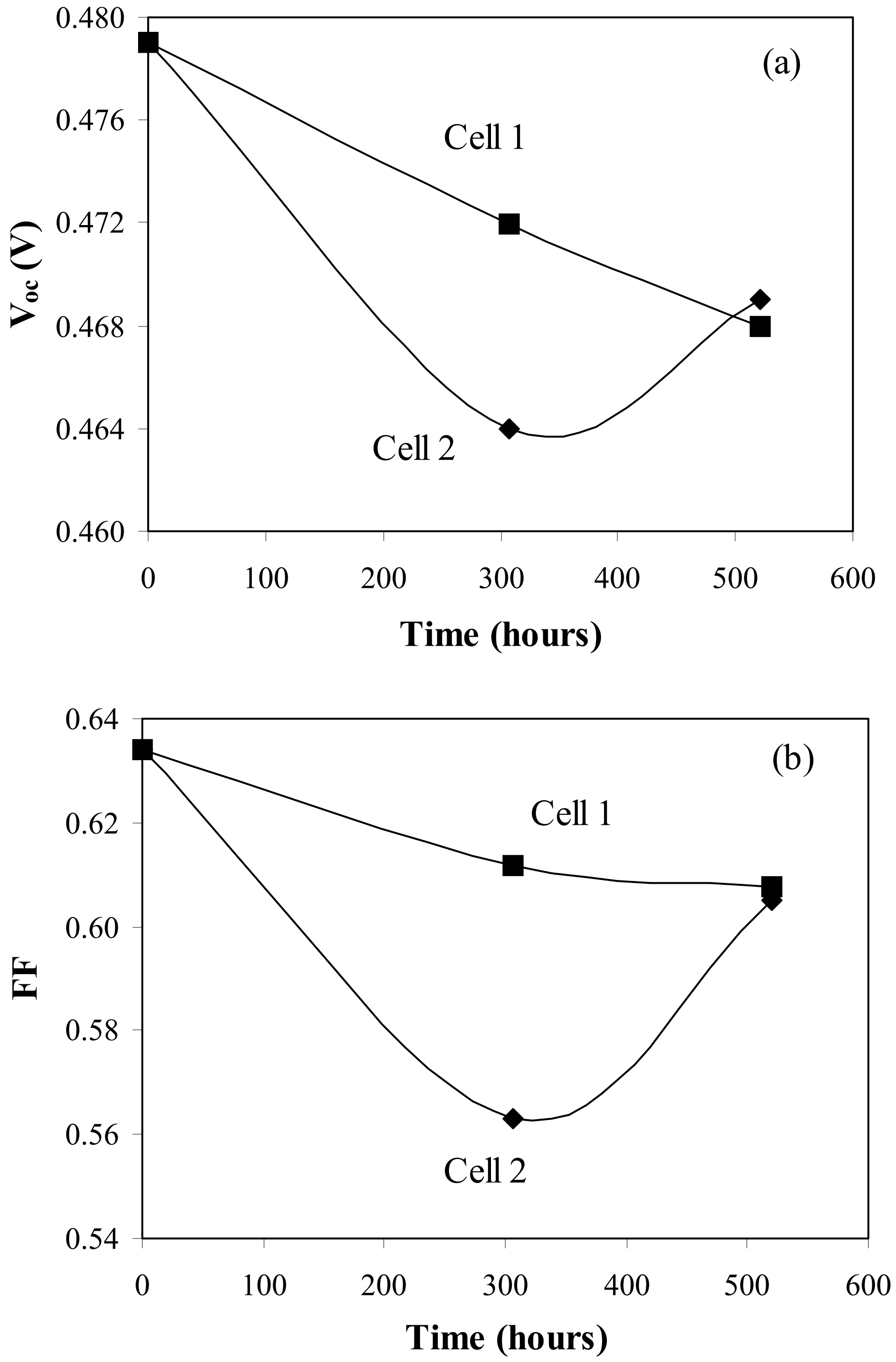

Figure 52. Photo-assisted annealing effect for the enhanced degradation by reverse bias. Cell 1 was light soaked under open-circuit conditions throughout the whole procedure. For the first 300 hours, Cell 2 was light soaked under a reverse bias of 1 V and then the reverse bias was removed. The solid line is only a guide for the eye.

10.5. Discussions

Due to the complex heterogeneous structure, the transport of carriers in nc-Si:H solar cells is not very well understood. In general, nc-Si:H can be considered as a mixed material comprised of grains and amorphous tissues. Based on transmission electron microscopy (TEM) and atomic force microscopy (AFM), Kočka *et al.*[26] proposed a model of nc-Si:H structures including large grain boundary and large grains with aggregation of tightly packed small grains. The small grains have a diameter of a few nanometers to over 20 nanometers. At the initial growth, the small grains are isolated from each other and embedded in amorphous tissues. The initial layer, with a low nanocrystalline volume fraction, is normally called an incubation layer and is avoided for solar cell deposition [6]. With the film growing thick, the crystalline volume fraction increases. As a result, the small grains aggregate to form large grains; and the amorphous tissues form narrow layers, called large grain boundaries, in the picture proposed by Kočka *et al.* [26]. Based on this model, most of the transport properties of nc-Si:H can be explained [26] by assuming that the large grain boundaries are characterized by a wide bandgap with band tail states, and the large grains have a narrow gap with bandtail states. The band tails in the large grains are from the grain boundary states. This model is also used to explain the defect structure in nc-Si:H films measured by electrically detected electron spin resonance [41] where two types of silicon dangling bonds are identified.

Based on the structure proposed by Kočka *et al.* [26], we now discuss possible mechanisms to explain the observed phenomena. Due to the nature of columnar growth of large grains, it is easy to form a percolation transport path of crystalline phase along the growth direction. In the dark, the conductivity in the amorphous phase (corresponding to large grain boundary region with Kočka's notation [26]) is much lower than that in the crystalline phase (large grains). The diffused or injected current from the doped layers basically flows through the percolation path of the grains and tunnels through the thin amorphous phase between two small grains. A previous experiment has shown that only the recombination events in the amorphous phase and grain boundaries are responsible for the degradation in nc-Si:H cells[15]. Since there are no excess carriers in the amorphous phase, current-induced degradation does not occur.

When exposed to light, the amorphous phase in the nc-Si:H material has to be considered, because the conductivity of the amorphous and nanocrystalline phases becomes comparable. In the current path, including the amorphous phase, the material is a randomly distributed hetero-junction system formed by an amorphous phase and large grains, which have different bandgaps and activation energies. Considering a given amorphous region, if both sides are large grains with a low bandgap, the interface region between the amorphous and grains can form a microscopic diode. Thus, a small unit of 'crystalline-amorphous-crystalline' is equivalent to two microscopic back-to-back connected diodes [16-17]. If we further assume that the nanocrystalline grains are more n-type material than the amorphous phase, the electrons will be accumulated in the amorphous side, and the crystalline side is depleted of electrons and accumulates holes when they form a diode. The charge redistribution will create a local internal electric field at the boundary between the amorphous and nanocrystalline phases. In this case, the conduction and valence bands of the amorphous side are bent down, and the conduction and valence bands of the crystalline side are bent up. To illustrate this picture, a schematic band diagram of a 'crystalline-amorphous-crystalline' region is drawn in Fig. 53 where (a) corresponds to the open circuit condition and (b) to the condition under a reverse bias. One can see that the excess electrons in the amorphous phase generated by illumination have a tendency to move out of the amorphous phase and into the grain boundary region where they will recombine with the holes accumulated in the crystalline side. Therefore, we expect that in addition to the light-induced defect generation in the amorphous region, light-induced defects would also be generated in the grain boundary region. In reality, there may not be a clear boundary between the amorphous and crystalline phase. With a finite thickness of the grain boundary region, the defect generation in the grain boundary region could play a significant role in carrier transport and solar cell performance. In addition, the grain boundary region may have a much higher defect density than ordinary a-Si:H. Based on this, it is not difficult to imagine that the light-induced degradation in nc-Si:H solar cells depends not only on the properties of the amorphous phase, such as the amorphous volume fraction, but also on the grain boundary properties, such as the hydrogen concentration and the structure of chemical bonds. When a reverse bias is applied to a nc-Si:H cell, the band diagram of the 'crystalline-amorphous-crystalline' structure is as shown in Fig. 53 (b). In this case, there are two mechanisms that give rise to the enhanced degradation of the nc-Si:H cell performance. First, for the forward biased diode (left side in Fig. 53 (b)), photo-generated electrons in the crystalline regions will move towards the amorphous regions. These excess electrons, together with the electrons generated in the amorphous region will recombine with the holes generated in the amorphous region, as illustrated by (1) and (2) in Fig. 53 (b). This will increase the defect generation rate in this region. However, on the right side, the enhanced electric field would sweep out the excess electrons more efficiently, which is similar to the reverse-biased light soaking on conventional a-Si:H solar cells, where the light-induced degradation is significantly suppressed by reverse bias. The internal field distribution, within the amorphous region, will determine whether there will be net additional defects created by the application of reverse bias or not. This, in turn, is determined by the thickness of these regions and also the nature of the boundaries between the amorphous and the nanocrystalline phase. If the thickness is small and the internal field is high, defect generation would take place only in the forward biased region (when a reverse bias is applied). The field in the rest of the region would be sufficiently high to prevent recombination either in the open circuit or the reverse bias case. Thus, there will be more light-induced defects generated by the application of an external reverse bias than when no bias is applied. In addition, we need to consider the second process as illustrated by (3), (4), and (5) in Fig. 53 (b). The excess electrons, generated in the amorphous phase, would easily move out of the amorphous phase on the right side of the figure. However, the electric field drives a significant amount of photo-generated holes in the crystalline region to the grain boundary as illustrated by (4), and the excess electrons moved to the grain boundary region will recombine with holes there, as described by process (5). It would be logical to assume that the grain boundary region has poor structure and more hydrogen concentration. Therefore, the recombination at the grain boundary will enhance the total defect generation. To summarize the proposed back-to-back diode model, we believe that two processes can cause the enhanced light-induced degradation by a reverse bias. First, the reduced electric field in the forward-biased diode causes additional recombination in the corresponding region. Second, the electrons driven out of the amorphous region by the electric field in the reverse diode recombine with the accumulated holes in the grain boundaries, which also produce additional defects.

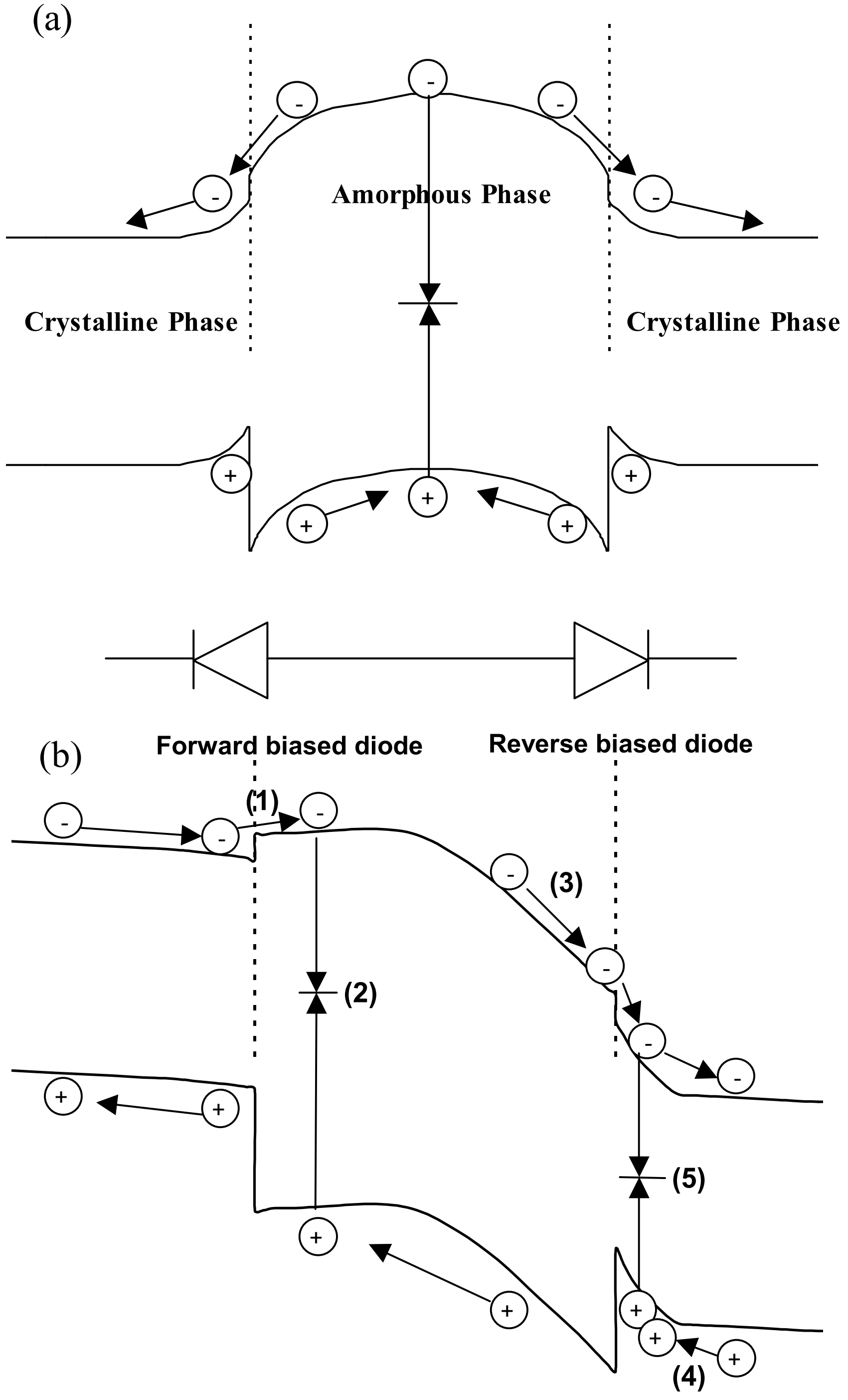

Figure 53. The band diagram of a ‘crystalline-amorphous-crystalline’ region in nc-Si:H material to illustrate the back-to-back diode model. (a) is under open circuit and (b) is under reverse bias during light-soaking. In (b), (1) represents the electron injection into the amorphous phase from the left crystalline phase in the forward biased diode, (2) photo-generated electron-hole pairs recombine in the forward biased region of the amorphous phase, (3) photo-generated electrons are swept out of the reverse biased region in the amorphous phase by an electric field (4) holes accumulate in the grain boundary in the right crystalline region, and (5) electrons recombine with the accumulated holes in the grain boundary region.

An immediate challenge for this model is why a forward-external bias does not increase the light-induced degradation. First, it is difficult to apply a high-forward bias without damaging the solar cell. For example, a 0.48 V of forward bias corresponds to the open-circuit condition. Second, a forward bias causes a significant current injection, and the injected space charges make the bias voltage drop mainly at the *p/i* interface region. In the bulk of the intrinsic layer, the electric field would be unaffected. Therefore, it is reasonable that no measurable difference was found between light-induced degradation under forward bias and open-circuit conditions.

The results of the quantum efficiency loss and color fill factor measurements (as shown in Figs. 51 and 50) suggest that the light-induced degradation in the nc-Si:H cells is not uniform. As we have mentioned earlier, FF_r is a measure of hole transport whereas FF_b is governed by electron transport. Since the mobility of electrons is higher than that of holes, one would, in general, expect less degradation in FF_b than in FF_r. When a forward bias is applied, however, the potential drop across the *p-i* interface would reduce the field therefore resulting in significant recombination at that interface. Since the blue photons generate carriers only near that interface, it is apparent that FF_b would show a larger degradation under forward bias than FF_r. The reverse bias enhanced degradation under different light spectra also provides additional support for the model illustrated in Fig. 53. Under a red light, most of the photons are absorbed in the nanocrystalline phase, and there are no photo-generated carriers in the amorphous phase. The resistance of the amorphous phase is still much higher than the nanocrystalline phase. Thus, the percolation path through the nanocrystalline grains is still the dominant current path. Although there might be a charge accumulation on both sides of the amorphous phase, the recombination rate would not be expected to increase dramatically. Consequently, no light-induced degradation occurs. On the other hand, for the blue light, most of the photons are absorbed in the amorphous phase close to the *p-i* interface since the absorption coefficient in the short wavelength region is much higher than in the crystalline phase. Recombination takes place both at the interface and in the bulk. Bulk recombination should have the same bias dependence, as discussed earlier, with reverse bias inducing more recombination. Interface recombination, however, is reduced under reverse bias. For a blue light, the ratio of carriers generated at the interface to those in the bulk is larger than that for the white-light illumination. The overall degradation under reverse bias for a blue light soaking would thus be less than that for a white light soaking. The light-assisted annealing of the enhanced degradation by the reverse bias is very similar to the light-assisted annealing in a-Si:H, a phenomenon that was originally observed in material properties such as photoconductivity and defect density and later on in a-Si:H solar cell performance [43 – 44]. A simple rate equation, including a light-induced annealing term, can explain the recovery of the defect created under some extreme conditions such as very-high light intensity or pulsed light illumination but cannot explain the continued degradation after the light-induced annealing. The concept of ‘fast’ and ‘slow’ defects was proposed [44] to explain these results where the two defective states have different annealing rates. In general, light-induced defects have a continuous distribution of annealing activation energies. Therefore, the phenomena, as shown in Fig. 52, could be simply explained by a continuous distribution of annealing activation energy [45]. However, we believe that there is more physics behind the phenomenon. As discussed above, nc-Si:H has a complicated structure, and it should be logical to assume that there is more than one type of defect. Lips *et al.* [41] have detected two kinds of silicon-dangling bonds using electrically detected electron spin resonance. In our case, one might assume that the defects, generated in the amorphous phase, are different from those in the grain boundary region. If two kinds of defects have different generation rates and annealing activation energies, one could interpret the results of Fig. 52, as explained for the light-assisted annealing in a-Si:H solar cells.

10.6. Summary and Conclusion

We have studied the behavior of light-induced degradation in nc-Si:H solar cells under various electrical bias conditions. We found that there is no forward-current-induced degradation in the dark, but an enhanced light-induced degradation under reverse bias. This is contrary to the results obtained in a-Si:H cells. Moreover, a forward bias does not cause additional light-induced degradation in the cell performance compared to the case of open-circuit conditions. The color FF and quantum efficiency loss measurements show that the light-induced defects, generated under reverse bias, are different from those under open-circuit conditions in terms of affecting the solar cell performance. The nc-Si:H cells, light soaked under reverse bias, show significant degradation on the long wavelength response and in FF_r. The effect of reverse bias on the light-induced degradation is more pronounced for illumination with a white light than a blue light. In addition, the enhanced light-induced degradation by reverse bias can be partially annealed away at the same temperature under the same illumination but under open-circuit conditions. Based on these experimental results, we propose a model to interpret the reverse bias, enhanced light-induced degradation in nc-Si:H solar cells. We believe that a 'crystalline-amorphous-crystalline' region in the nc-Si:H layer could be considered as a back-to-back connected diode structure. Considering the recombination at the *p-i* interface in the amorphous silicon region and at the grain boundaries, we explained most of the experimental observations using the proposed model in a self-consistent manner.

Section 11: Future Work

We have made significant progress during this program. We will continue our efforts in the next Thin Film Partnership Program to address the DOE's short-term and long-term goals. The main focuses for the next program are summarized below.

11.1. High efficiency multi-junction solar cells

To achieve an even higher efficiency, we need to increase the total photocurrent density. Currently, we have achieved a total photocurrent density around 26-27 mA/cm^2. This value is still not as high as reported in the literature. If we obtain a total photocurrent density of over 30 mA/cm^2, we shall achieve an initial active-area efficiency larger than 16% (J_{sc}=9.6 mA/cm^2, V_{oc}=2.2 V, FF=0.76); and consequently, improve the stable efficiency. To achieve this goal, we continue to optimize the nc-Si:H bottom cell by optimizing the deposition conditions and cell design. In addition, we may investigate the possibility of using nc-SiGe:H alloy to enhance the total current density. At the same time, we will optimize the back reflector.

11.2. High rate deposition of multi-junction solar cells

For high-rate deposition, we shall continue to work on the MVHF deposition. Two major issues need to be addressed. First, we shall increase the deposition rate further to limit the nc-Si:H intrinsic layer deposition time to less than 30 minutes. Second, we shall improve the cell performance further. In Phases II and III of this program, we have achieved stable active-area efficiencies of 11.0% and 11.5% using an a-Si:H/nc-Si:H double-junction structure. Although extensive deposition parameters have been explored, there is still a large pool of plasma conditions that need to be investigated. In addition, we shall continue to modify the deposition chamber based on the knowledge accumulated in the current program to improve the cell efficiency and uniformity.

11.3. Larger-area a-Si:H/nc-Si:H double-junction cells at high-deposition rates

We have achieved an initial aperture-area efficiency of 11.8% using an a-Si:H/nc-Si:H double-junction structure with an aperture area of 420 cm^2. This cell shows an efficiency of 9.6% after encapsulation and light soaking. The nc-Si:H intrinsic layer was deposited using a RF glow discharge for 50 minutes. We shall reduce the deposition time to around 20-30 minutes, and increase the efficiency further. To achieve these goals, we shall continue to optimize the deposition condition of the RF glow discharge. At the same time, we shall explore the possibility of using MVHF in the large-area deposition of nc-Si:H solar cells.

11.4. Explore new deposition regime for a-SiGe:H alloy

A major breakthrough for a-Si:H and a-SiGe:H alloys in solar cell applications is high hydrogen dilution, which improves not only the efficiency but also the stability under light soaking. Most of the deposition parameters in the current deposition regime have been tested. Although the a-SiGe:H quality has been improved through constant studies in the program, the narrow bandgap a-SiGe:H bottom cell is still the bottleneck for high efficiency multi-junction solar cells. In order to obtain an even higher efficiency, we need to explore some new deposition conditions such as a high pressure RF glow discharge. For this purpose, systematic studies on the plasma physics and chemistry would be helpful.

11.5. Optimization of a-Si:H/a-SiGe:H/a-SiGe:H triple-junction cells and modules

Our 2B machine has been upgraded. As a result, the uniformity has been improved significantly. In the current program, we have worked on the optimization of component cells and triple-junction cells using SiH_4 as a substitute for Si_2H_6 in the a-SiGe:H alloy. We achieved similar results by using Si_2H_6. In the next program, we shall work on large-area a-Si:H/a-SiGe:H/a-SiGe:H triple-junction modules to accomplish the proposed milestones. Meanwhile, we will modify the geometry of the reactor based on the new understanding to minimize the light-induced degradation and achieve higher efficiency. We shall transfer the knowledge, learned from the 2B machine, to the manufacturing line and to increase the efficiency of our product, and increase the throughput of the manufacturing machine.

REFERENCES

[1] J. Yang, A. Banerjee, and S. Guha, *Appl. Phys. Lett.* **70**, 2975 (1997).

[2] A. Banerjee, J. Yang, and S. Guha, *Mater. Res. Soc. Symp. Proc*. **557**, 743 (1999).

[3] S. Guha, *Proc. of 31st Photovoltaic Specialists Conference*, (Florida, January 3-7, 2005), p. 12.

[4] K. Yamamoto, A. Nakajima, M. Yoshimi, T. Sawada, S. Fukuda, T. Suezaki, M. Ichikawa, Y. Koi, M. Goto, H. Takata, T. Sasaki, and Y. Tawada, *Proc. of 3rd World Conf. on Photovoltaic Energy Conversion* (May 2003, Osaka, Japan), p. 2789.

[5] K. Saito, M. Sano, H. Otoshi, A. Sakai, S. Okabe, and K. Ogawa, *Proc. of 3rd World Conf. on Photovoltaic Energy Conversion* (May 2003, Osaka, Japan), p. 2793.

[6] B. Yan, G. Yue, J. Yang, A. Banerjee, and S. Guha, *Mater. Res. Soc. Symp. Proc.* **762**, 309 (2003).

[7] J. Yang, A. Banerjee, K. Lord, and S. Guha, *Proc. of 28th IEEE Photovoltaic Specialist Conference* (IEEE, Anchorage, AK, 2000), p. 742.

[8] J. Owens, D. Han, B. Yan, J. Yang, K. Lord, and S. Guha, *Mat. Res. Soc. Symp. Proc.* **762,** 339 (2003).

[9] K. Lord, B. Yan, J. Yang, and S. Guha, *Appl. Phys. Lett.* **79**, 3800 (2001)

[10] J. Yang, K. Lord, B. Yan, A. Banerjee, S. Guha, D. Han, and K. Wang, *Mat. Res. Soc. Symp. Proc.* **715**, 601 (2002).

[11] B. Yan, J. Yang, G. Yue, K. Lord, and S. Guha, *Proc. of 3rd World Conference on Photovoltaic Energy Conversion,* (Osaka, May 11-18, 2003), p.1627.

[12] J. Meier, R. Flückiger, H. Keppner, and A. Shah, Appl. Phys. Lett. **65**, 860 (1994).

[13] E.V. Shah, J. Meier, E. Vallat-Sauvain, N. Wyrsch, U. Kroll, C. Droz, and U. Graf, Solar Energy Materials & Solar Cells **78**, 469 (2003).

[14] B. Yan, K. Lord, J. Yang, and S. Guha, *Mater. Res. Soc. Symp. Proc.* **715**, 629 (2002).

[15] B. Yan, G. Yue, J. M. Owens, J. Yang, and S. Guha, *Appl. Phys. Lett.* **85**, 1755 (2004).

[16] G. Yue, B. Yan, J. Yang, and S. Guha, *Appl. Phys. Lett*. **86**, 092103 (2005).

[17] G. Yue, B. Yan, J. Yang, and S. Guha, *J. Appl. Phys.* (2005), to be published.

[18] L. Guo, M. Kondo, M. Fukawa, K. Saitoh, and A. Matsuda, Jpn., *J. Appl. Phys.* **37**, L1116 (1998).

[19] M. Kondo, M. Fukawa, L. Guo, and A. Matsuda, *J. Non-Cryst. Solids* **84**, 266-269, (2000).

[20] B. Rech, T. Roschek, J. Müller, S. Weider, H. Wagner, Sol. Energy Mat. Sol. Cells, **62**, 267 (2001).

[21] Y. Nasuno, M. Kondo, and A. Matsuda, *Proc. of 28th IEEE Photovoltaic Specialists Conference* (IEEE, Anchorage, Alaska, 2000), p.142.

[22] M. Kondo, *Solar Energy Materials & Solar Cells* **78**, 543 (2003).

[23] F. Finger, S. Klein, T. Dylla, A. L. Baia Neto, O. Vetterl, and R. Carius, *Mater. Res. Soc. Symp. Proc.* **715**, 123 (2002).

[24] B. Rech, J. Muller, T. Repmann, O. Kluth, T. Roschek, J. Hupkes, H. Stiebig, and W. Appenzeller, *Mater. Res. Soc. Symp. Proc.* **762**, 285 (2003).

[25] J. Kočk, H. Stuchlíková, J. Stuchlík, B. Rezek, T. Mates, and A. Fejfar, Technical Digest of the International PVSEC-12, (Jeju, Korea, 2001) p. 469.

[26] J. Kočk, A. Fejfar, H. Stuchlíková, J. Stuchlík, P. Fojtík, T. Mates, B. Rezek, K. Luterová, V. Šverčk, and I. Pelant, *Solar Energy Material & Solar Cells* **78,** 493 (2003).

[27] S. Guha, J. Yang, D. L. Williamson, Y. Lubianiker, J. D. Cohen, and A. H. Mahan, *Appl. Phys. Lett.* **74**, 1860 (1999).
[28] A. Banerjee and S. Guha, *J. Appl. Phys.* **69**, 1030 (1991).
[29] B. Yan, G. Yue, K. Lord, A. Banerjee, and S. Guha, *Proc. of 3rd World Conf. on Photovoltaic Energy Conversion* (Osaka, Japan, 2003), p. 2773.
[30] J. Müller, G. Schöpe, O. Kluth, B. Rech M. Ruske, J. Trube, B. Szyszka, Th. Höing, X. Jiang, and G. Bräuer, *Proc. of 28th IEEE Photovoltaic Specialist Conf.* (AK, 2000), p. 758.
[31] T. Matsui, A. Masuda, and M. Kondo, *Mater. Res. Symp. Proc*. **808**, 557 (2004).
[32] T. Repmann, T. Kilper, W. Appenzeller, C. Zahren, H. Stiebig, and B. Rech, *Proc. of 31st Photovoltaic Specialists Conference*, (Florida, January 3-7, 2005), p. 1383.
[33] A. Gordijn, J. Francke, J. K. Rath, and R. E. Schropp, *Mater. Res. Soc. Symp. Proc*. **862**, A10.3 (2005).
[34] G. Yue, B. Yan, J. M. Owens, J. Yang, and S. Guha, *Mater. Res. Soc. Symp. Proc*. **808**, 593 (2004).
[35] Y. Nasuno, M. Kondo, and A. Matsuda, *Appl. Phys. Lett*. **78**, 2330 (2001).
[36] Y. Nasuno, M. Kondo, and A. Matsuda, *Proc. of 28th IEEE Photovoltaic Specialists Conf.* (Alaska, 2000), p. 142.
[37] B. Yan, G. Yue, J.M. Owens, J. Yang, and S. Guha, *Appl. Phys. Lett.* **85**, 1925 (2004).
[38] S. Klein, F. Finger, R. Carius, T. Dylla, B. Rech, M. Grimm, L. Houben, and M. Stutzmann, Thin Solid Films **430**, 202 (2003).
[39] F. Meillaud, E. Vallat-Sauvain, X. Niquille, M. Dubey, J. Bailat, A. Shah, and C. Ballif, *Proc. of 31st Photovoltaic Specialists Conference*, (Florida, January 3-7, 2005), p. 1412
[40] A. Pawlikiewicz and S. Guha, *Mater. Res. Soc. Symp. Proc.* **118**, 599 (1988).
[41] A. Banerjee, X. Xu, J. Yang, and S. Guha, *Appl. Phys. Lett.* **67**, 2975 (1995).
[42] K. Lips, P. Kanschat, and W. Fuhs, *Sol. Energy Mater. Sol. Cells* **78**, 513 (2003).
[43] X. Xu, J. Yang, and S. Guha, *Mater. Res. Soc. Symp. Proc*. **297**, 649 (1993).
[44] L. Yang and L. Chen, *Mater. Res. Soc. Symp. Proc*. **297**, 619 (1993).
[45] B. Yan, J. Yang, K. Lord, and S. Guha, *Mater. Res. Symp, Proc*. **664**, A25.2 (2001).

REPORT DOCUMENTATION PAGE

Form Approved
OMB No. 0704-0188

1. REPORT DATE *(DD-MM-YYYY)* October 2005	**2. REPORT TYPE** Subcontract Report	**3. DATES COVERED** *(From - To)* 30 May 2002 – 31 May 2005

4. TITLE AND SUBTITLE High-Efficiency Amorphous Silicon Alloy Based Solar Cells and Modules; Final Technical Progress Report, 30 May 2002 – 31 May 2005	**5a. CONTRACT NUMBER** DE-AC36-99-GO10337
	5b. GRANT NUMBER
	5c. PROGRAM ELEMENT NUMBER
6. AUTHOR(S) S. Guha and J. Yang	**5d. PROJECT NUMBER** NREL/SR-520-38728
	5e. TASK NUMBER PVB55101
	5f. WORK UNIT NUMBER
7. PERFORMING ORGANIZATION NAME(S) AND ADDRESS(ES) United Solar Ovonic Corporation Troy, Michigan	**8. PERFORMING ORGANIZATION REPORT NUMBER** ZDJ-2-30630-19
9. SPONSORING/MONITORING AGENCY NAME(S) AND ADDRESS(ES) National Renewable Energy Laboratory 1617 Cole Blvd. Golden, CO 80401-3393	**10. SPONSOR/MONITOR'S ACRONYM(S)** NREL
	11. SPONSORING/MONITORING AGENCY REPORT NUMBER NREL/SR-520-38728

12. DISTRIBUTION AVAILABILITY STATEMENT

National Technical Information Service
U.S. Department of Commerce
5285 Port Royal Road
Springfield, VA 22161

13. SUPPLEMENTARY NOTES

NREL Technical Monitor: Bolko von Roedern

14. ABSTRACT *(Maximum **200 Words**)*

The principal objective of this R&D program is to expand, enhance, and accelerate knowledge and capabilities for development of high-efficiency hydrogenated amorphous silicon (a-Si:H) and amorphous silicon-germanium alloy (a-SiGe:H) related thin-film multijunction solar cells and modules with low manufacturing cost and high reliability. Our strategy has been to use the spectrum-splitting triple-junction structure, a-Si:H/a-SiGe:H/a-SiGe:H to improve solar cell and module efficiency, stability, and throughput of production. The methodology used to achieve the objectives included: i) explore the highest stable efficiency using the triple-junction structure deposited using RF glow discharge at a low rate, ii) fabricate the devices at a high deposition rate for high throughput and low cost, and iii) develop an optimized recipe using the R&D batch large-area reactor to help the design and optimization of the roll-to-roll production machines. For short-term goals, we have worked on the improvement of a-Si:H and a-SiGe:H alloy solar cells. a-Si:H and a-SiGe:H are the foundation of current a-Si:H based thin-film photovoltaic technology. Any improvement in cell efficiency, throughput, and cost reduction will immediately improve operation efficiency of our manufacturing plant, allowing us to further expand our production capacity.

15. SUBJECT TERMS

PV; high-efficiency; amorphous silicon; solar cells; module; manufacturing; module; thin-film; capacity; triple junction; glow discharge

16. SECURITY CLASSIFICATION OF:			**17. LIMITATION OF ABSTRACT**	**18. NUMBER OF PAGES**	**19a. NAME OF RESPONSIBLE PERSON**
a. REPORT	**b. ABSTRACT**	**c. THIS PAGE**			
Unclassified	Unclassified	Unclassified	UL		**19b. TELEPONE NUMBER** (*Include area code*)

Standard Form 298 (Rev. 8/98)
Prescribed by ANSI Std. Z39.18